University of Rajshahi **Rajshahi-6205** **Bangladesh.**

RUCL Institutional Repository **http://rulrepository.ru.ac.bd**

Department of Physics PhD Thesis

1996

Study of Physical Properties and Modelling of Sio and V205 Sandwich Devices

Sarkar, Md. Jamshed Ali

University of Rajshahi

http://rulrepository.ru.ac.bd/handle/123456789/910

Copyright to the University of Rajshahi. All rights reserved. Downloaded from RUCL Institutional Repository.

Study of Physical Properties and Modelling of Sio and V205 Sandwich Devices

By

MD. JAMSHED ALI SARKAR
M. SC. (RAJSHAHI)

This thesis has been submitted in fulfilment of the requirements for the degree of Doctor of Philosophy at Rajshahi University, Bangladesh.

Rajshahi June, 1996

CONTENTS

		Page No.
	Acknowledgement	i
	Abstract	ii
	CHAPTER I INTRODUCTION	1
1.1	Scope of the Thesis	2
	CHAPTER II A critical review of electrical conduction mechanism in thin dielectric films	3
2.1	D.C and A.C. conduction mechanisms in unformed and pre-formed MIM devices.	3
2.1.1	D.C Conduction mechanisms	3
2.1.1.1	Schottky emission	5
2.1.1.2	Poole-Firenkel emission and its modifications	8
2.1.1.3	Distinction between Schottky and Poole-Frenkel emission.	15
2.1.1.4	Space- Change-Limited [SCL] flow	16
2.1.1.5	D.C Hopping	19
2.1.2	A.C. Conduction mechanism	21
2.2	Electroforming in MIM structures	26
2.2.1	Models based on homogeneous penetration.. . .	27
2.2.1.1	Hickmott's model	27
2.2.1.2	Simmons Verderber and Eales model	28
2.2.1.3	Barriac et. at. model	30
2.2.1.4	Greene, Bush and Rawlings model	31
2.2.2	Filamentary models	33
2.2.2.1	Dearnaley, Morgan and Stoneham model	33
2.2.2.2	Ralph and woodcock's model	36
2.2.2.3	Rakhshani, Hogarth and Abidi model	38
2.2.2.4	Sutherland modification for the filamentary model.	39
2.2.2.5	Our modification to the filamentary model . .	40

CHAPTER III.
Experimental equipments and technique . . . 41

3.1 Preparation of samples in vacuum. 41
3.2 Boats and filaments 42
3.3 Electron beam source 43
3.4 Substrate cleaning procedure. 43
3.5 Deposition parameters. 44
3.6 Sample fabrications 44
3.7 Sample thickness measurement 45
3.8 Electrical measurement systems 45
3.8.1 D.C. Measurements 45
3.8.2 A.C Measurements 45
3.9 Optical Measurements 46
3.10 Structural Study 46

CHAPTER IV Experimental results and discussion

4.1 Electrical Measurements 47
4.1.1 D.C Measurements 47
4.1.2 A.C Measurements in unformed and pre-formed MIM devices 54
4.1.2.1 Analysis and discussion of A.C results . . . 54
4.1.3 VCNR, Switching and electron emission in Al-SiO - Cu / Al-V_2O_5 - Cu / Al-V_2O_5 - Al sandwich structures. 58
4.1.4 Optical measurements 60
4.1.4.1 UV and visible measurements 61
4.1.4.2 IR measurements 63
4.1.4.3 Proposed electronic band structure of SiO . . 64
4.1.4.4 X-ray diffraction study 65

CHAPTER V
Conclusion and suggestions for further research. 66

REFERENCES 68

ACKNOWLEDGEMENT

I thank my supervisor Dr. M.A.R. Sarkar, Professor, Department of Applied Physics and Electronics, Rajshahi University for his constant guidance, help and encouragement throughout the course of this work.

I wish to thank Dr. M. Delawer Hossain for supplying me silicon chips for IR studies and Mr. M. Rezaul Islam for his necessary help in the instrumentations.

I am indebted to Dr. M. Azizul Islam and Dr. M. Abdul Jalil Miah, Department of Chemistry, Rajshahi University for providing the facilities in IR studies and Mrs. Nurus Saba Khanam and Mr. Abu Taher Mondal, Department of Bio-chemistry, Rajshahi University for their help for UV and visible studies.

I also express my thank to Professor Fakrul Islam, Department of Applied Chemistry and Chemical Technology, Rajshahi University for supplying me V_2O_5 materials and Mr. M. Badruddoza, Technician, Department of Physics, Rajshahi University for his help in making masks of different sizes.

I am obliged to the all teachers, technical staff, Librarian staff, office staff and store-keeper Mr. M. Mojammel Hoque, Department of Applied physics and Electronics, R.U. for their co-operation and assistance throughout my research work.

Finally I am grateful to the University Grants Commission, Bangladesh for awarding me a Junior Research Fellowship and Rajshahi University for granting me a study leave to prosecute my Ph.D. research programme.

ABSTRACT

Electrical measurements have been carried out in Al-SiO-Al unformed and Al-SiO-Cu pre-formed devices having insulator thicknesses in the range 50 nm - 600 nm at ambient and different temperatures and under modest vacum with the application of DC high fields. The DC conductivity has been explained by normal poole-Frenkel model based on localized conduction.

AC measurements have also been carried out in these devices in the frequency range 100 Hz -100 KHz. The measured activation energy and the monotonic increase of conductivity suggest that the conductions mechanism operating in these devices are of multiphonon hopping type.

The electroformed studies such as VCNR, electronic switching and electron emission in the Al-SiO-Cu/Al-V_2O_5-Cu divices were explained by employing the modified filamentary model.

The structural studes of SiO and V_2O_5 suggest that these film materials are amorphous in character.

The information obtained from optical study (UV, Visible and IR) and the DC activation energy help to construct the electrical band diagram of SiO.

Becasue of lacking information it was not possible to construct an electronic band diagram of V_2O_5.

CHAPTER I

INTRODUCTION

Currently worldwide study of dielectric films has been a subject of extensive theoretical and experimental investigations because of their many potential applications in science and technology and in many varied fields. Electronic use of insulating films include field effect transistors, passivating layers, capacitors, sweitching elements, electron emitters, electroluminescent devices, etc. Other potential non-electronic applications include replica and supporting membranes for electron microscope and electron diffraction studies, as multilayer combinations for increasing and decreasing the reflectance of dielectrices and metals in various spectral regions, as heat reflecting filter and finally as selective surfaces for photothermal conversion of solar energy.

The widespread and ever-increasing films demand that more knowledge is required about their electrical and physical properties. Hence, explorations of new dielectric films or the dielectric films already investigated need further study for obtaining newer and more properties. Having these ideas in mind I decided to study the electrical, optical and structural properties of the SiO and V_2O_5 devices.

Scope of the Thesis

A systematic investigation of the electrical, optical and structural properties of SiO and V_2O_5 devices is to be presented. Thus the aim of this research is to investigate the followings:

1. DC transport properties of unformed Al-SiO-Al and Pre-formed Al-SiO-Cu sandwich structures under high electric fields.
2. AC transport properties of unformed Al-SiO-Al and pre-formed Al-SiO-Cu sandwich structures.
3. Electroformed characteristics of Al-SiO-Cu/Al-V_2O_5-Cu/Al-V_2O_5-Al sandwich structures.
4. Optical measurements such as visible, UV and IR transmission spectra in the 350-900 nm and 2.5-50 μm (4000-200 cm^{-1}) wavelength ranges respectively.
5. X-ray diffraction study of SiO and V_2O_5 films

In chapter II a critical review has been presented concerning the various models of electrical conduction in thin insulating films.

Chapter III deals with the substrate cleaning technique, experimental apparatus for preparation of specimen for the various studies and measuring techniques.

Experimental results, their analyses and suggested models are presented in chapter IV.

Conclusion and suggestions for further research are presented in Chapter V.

CHAPTER II

A CRITICAL REVIEW OF ELECTRICAL CONDUCTION MECHANISMS IN THIN DIELECTRIC FILMS.

A critical review of electrical conduction mechanisms under high field conditions for the following two categories of devices has been presented in this chapter :

(i) Unformed and preformed Metal-Insulator-Metal MIM MIN devices

(ii) and formed MIM devices.

Section 2.1 deals with the conduction processes operating in the first category of devices and section 2.2 deals with that of the second category of devices.

2.1 D.C. and A.C. conduction Mechanisms in unformed and Preformed MIM Devices.

2.1.1 D.C. Conduction Mechanisms.

The systematic study of various charge transport mechanisms through thin dielectric films sanwiched between metallic electrodes has been contimed since 1960. The probable conduction mechanisms operating through such devices in the presence of an electric field are illustrated in Fig.2.1. using electronic energy band diagram. It is observed from this diagram that electrons can be injected from the cathode into the conduction band of the insulator over the potential barrier at the metal-insulator interface by thermal activation (mechanism-1). This process is called Schottky effect.

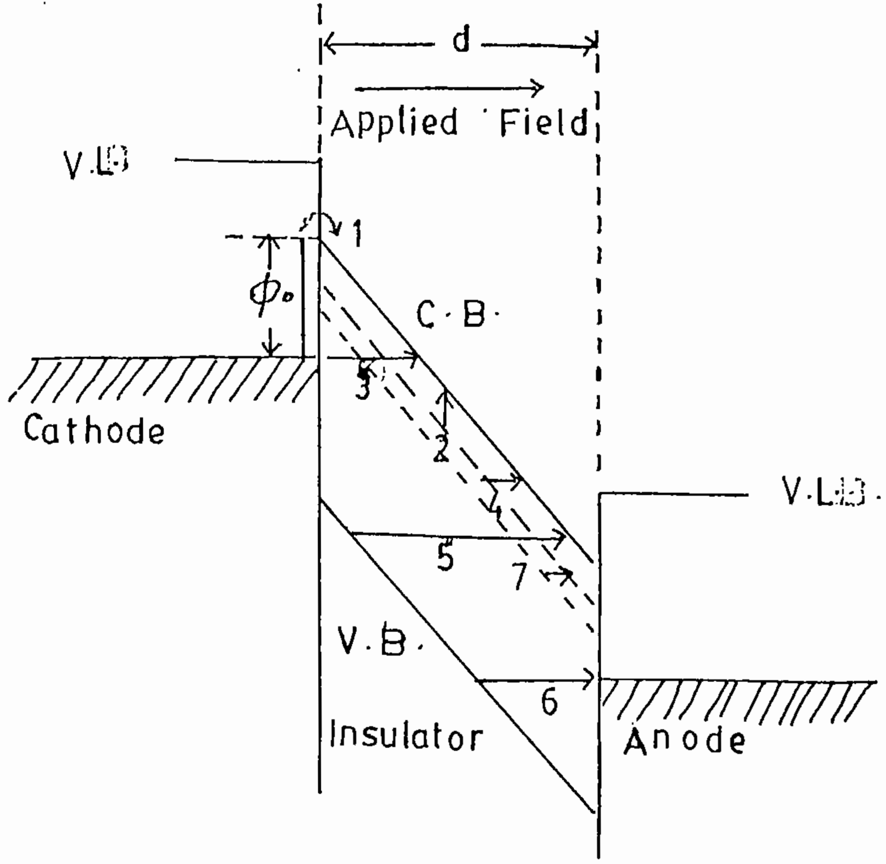

Fig.2.1. High field conduction mechanism.

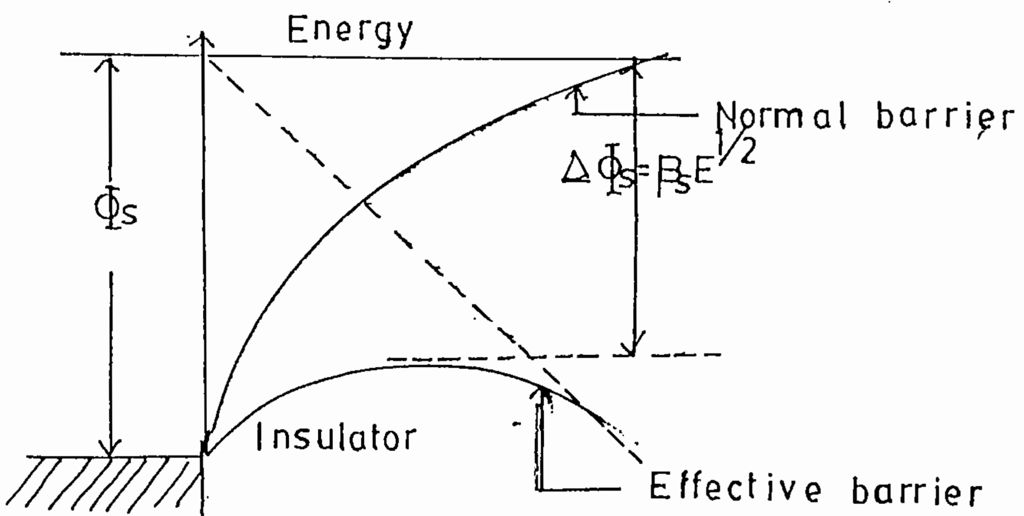

Fig.2.2. Schottky barrier.

Process-2 shows that electrons may also be thermally excited into the conduction band of the insulator from trapping levels inside its forbidden gap. This conduction mechanism is termed the Poole-Frenkel emission (mechanism-2). Electrons may also tunnel directly into the conduction band of the insulator either from the cathode (mechanism-3) or trapping levels within the insulator (mechanism-4) or the valance band of the insulator (mechanism-5). It is also possible for electrons to tunnel to the anode from the valence band of the insulator (mechanism-6). If the thickness of the insulator is less than 10 nm, electrons may tunnel directly between the metal electrodes. The latter mechanism will no be discussed in details because this type of film has not been fabricated in the present work.

Furthermore, non-linear current flow through the insulator may occur due to the presence of impurities, for example, foreign atoms or defects. Schottky or Poole-Frenkel defects may cause either impurity or ionic conduction. Impurity conduction involves electron transport from one stationary donor to an adjacent donor (mechanism-7) as shown in Fig. 2.1) whereas in ionic conduction the impurities or defects in the films migrate. Extremely low ionic mobility μ of the carriers (typically μ = 10^{-12} m^2 $v^{-1}S^{-1}$) and high activation energy (>0.6 ev) characterize the ionic conduction. In ionic conduction mass transfer occurs through the insulator to an electrode. Finally at very low temperatures electronic effects may also include tunnelling whilst ions (both types) are unable to tunnel.

Charge injection into the conduction band, tunnelling or impurity conduction in some cases may cause to build up of space-charge within the bulk of the material which limits the charge transport. This effect is called space-charge limited conduction.

A number of the above mentioned conduction mechanisms may operate simultaneously at one particular applied potential difference across the device, but generally one mechanism will dominate the observed current. Some of the above stated conduction mechanisms are discussed in details below :

2.1.1.1 Schottky Emission.

The Schottky effect is the emission of electrons into the conduction band of an insulator from the metal contact electrode (the contact electrode may also be a semiconductor) by thermal excitation over the field-lowered metal-insulator interfacial barrier. This is an electrode-limited conduction process. This emission mechanism is shown in (Fig. 2.2). The lowering of the barrier height $\Delta\phi_s$ is caused by the interaction of the electron image force with the applied electric field E and is given by

$$\Delta\phi_s = (Ee^3/4\pi\epsilon_0 E)^{1/2} = \beta_s E^{1/2} \quad \text{..........(2.1)}$$

Where

$$\beta_s = (e^3/4\pi E_0 \epsilon)^{1/2} \quad \text{......................(2.2)}$$

β_s is called the Schottky field-lowering coefficient. In the above expression

e = electronic change,

ϵ = dielectric constant of the insulating film

and ϵ_0 = dielectric constant of free space ($\approx 8.85 \times 10^{-12}$ F^{+} m^{-1}).

This type of electron emission from the electrode at a negative potential would be analogous to the thermionic emission except that the applied electric field lowers the barrier height. The current density J_R for thermionic emission over a potential barrier of height ϕ would be given by the Richardson equation

$$J_R = AT^2 \exp(-\phi / KT) \quad \ldots\ldots\ldots\ldots\ldots\ldots(2.3)$$

Where T is the absolute temperature of the emitter and A is the Richardson constant which is given by

$$A = 4\pi mek^2/h_3 \quad \ldots\ldots\ldots\ldots\ldots\ldots\ldots\ldots \quad (2.4)$$

For most metals A is about 60-100A $cm^{-2}K^{-2}$.

In expression (2.4), K is the Boltzmann constant, H is Planck's constant and m is the electronic mass.

Because of the image-force lowering of the potential barrier, the electrode limited current does not saturate according to the Richardson equation (2.3), but rather obeys the Richardson - Schottky (law :- The current density under these conditions may be identified by the symbol J_{RS} which is given by

$$J_{RS} = J_R \exp(\beta_s E^{1/2}/KT) \ldots\ldots\ldots\ldots\ldots\ldots\ldots(2.5)$$

In deriving equation (2.5) Schottky neglected the electron-electron interaction term in calculating the carrier density using the Fermi-Dirac statistics. This assumption is practically not true because the emission current has a significant magnitude and hence there is always the possibility of electron-electron interaction. He also assumed a constant value of work function: In practice, however, the work function will increase if an electronic space-

charge exists in the vicinity of the emitter. It also decreases with increasing electric field strength. Small amounts of absorbed gases like nitrogen and carbon dioxide will increase the work function. In addition the emitting area is not, in general, equal to the actual surface area. The presence of these possible sources of error suggests that a rigorous fit of theoretical and experimental results cannot be expected.

It has been shown that the effect of an electron having differing masses in the metal and insulator implies that an effective mass m^* must be used in the constant A (equation 2.4). Simmons (27) has pointed out that equation (2.5) holds only if the electron mean free path is of the order of the insulator thickness.

According to Stuart (34) both Schottkey and the Poole-Frenkel emissions give a linear plot of log I against $V^{1/2}$. In the case of Schottky emission, the field E_0 at the interface due to the applied voltage is equal to V_g/d ($d \approx$ film thickness, V_g applied voltage). This may cause band bending near the interface and results in a non-linear dependence of E on V. Mahalingam *et al* (33) stated that if the transport of current is due to Schottky emission, the plot of log (I/T^2) versus $1/T$ would be a straight line. In the light of above mentioned model. Simmons (27) showed from his experimental data on the bulk conductivity of Ta_2O_5 and SiO films that the electrical conduction in these materials were due to Schottky emission. Geddes *et al* (107) analyzed Schottky emission in Al-22-tricosenioc acid Mg sandwich assuming Schottky barrier height to be 1.06 ev.

2.1.1.2 Poole-Frenkel Emission and its Modifications

The Poole-Frenkel effect initially put forward by Frenkel (88) is a bulk limited conduction process. Electrons are emitted from trapping centers in semiconductors and insulators by the combined effect of temperature and electric field. It is also called field-assisted thermal ionization. Fig.2.3 shows the Poole-Frenkel effect. The solid line in this diagram represents the normal potential energy of the electron as a function of the distance X from the positive ion. This potential energy ϕ_{PF} of the electron at a distance X_0 would be given by

$$\phi_{PF} = -e^2/4\pi\epsilon_0\epsilon x_0 \quad \ldots\ldots\ldots\ldots \quad (2.6)$$

In the presence of an external field E the coulomb potential is reduced by a factor $-eEx_o$. The resultant potential barrier for thermal excitation of trapped electrons into the conduction band is shown by the dashed curves in (Fig. 2.3). The resultant potential at a distance X_0 would be given by

$$\Delta\phi = -e^2/4\pi\epsilon_0\epsilon x_0 - eEx_0 \quad \ldots\ldots\ldots\ldots \quad (2.7)$$

If X_0 is defined as the distance from the ion at which the potential energy has its maximum value, then

$$\frac{d}{dx_0}\left(- e^2/4\pi\epsilon_0\epsilon x_o - eEx_o\right) = 0 \text{ which after}$$

Simplification gives $X_o = e/4\pi\epsilon_o\epsilon E)^{1/2}$ $\quad \ldots\ldots\ldots \quad (2.8)$

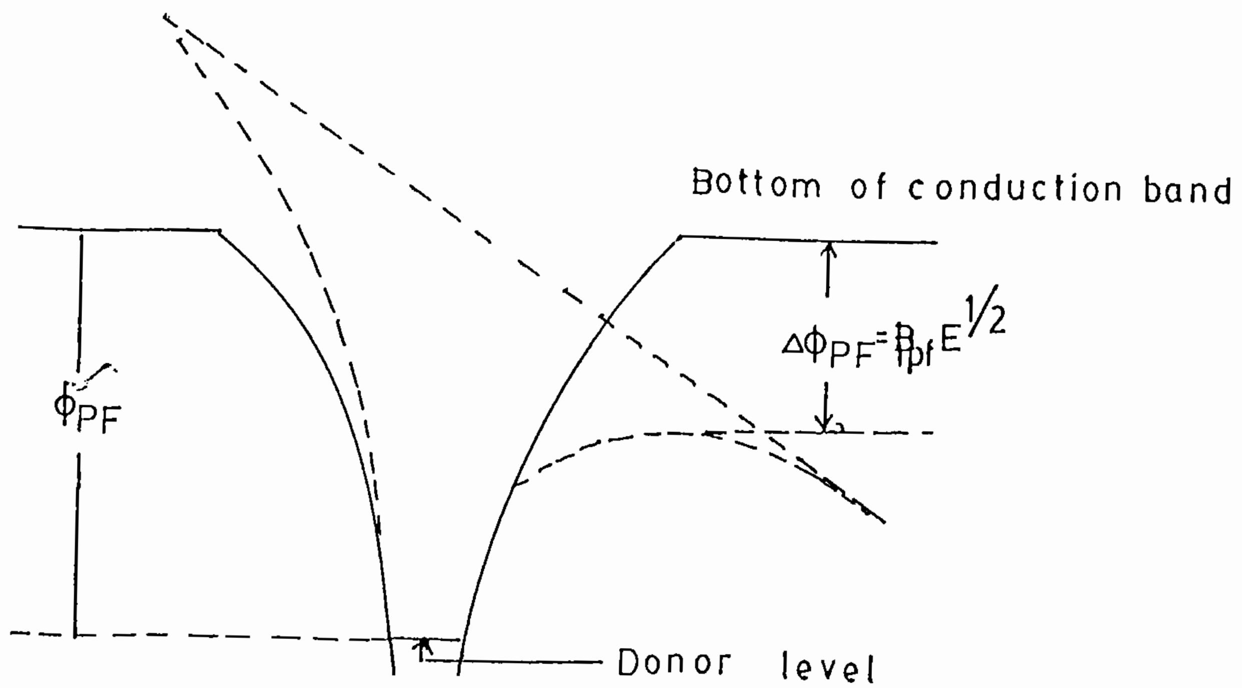

Fig.2.3. Poole-Frenkel barrier.

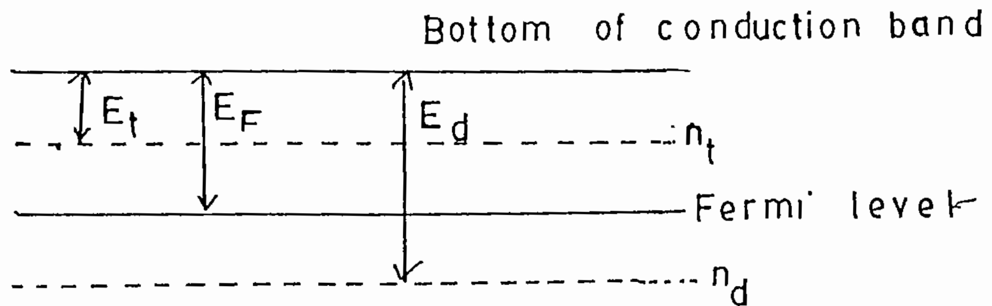

Fig.2.4. Trapping level.

Putting value of X_0 from (2.8) in (2.7) we obtain

$$\Delta\phi_{PF} = -2 \ (e^3E/4\pi\epsilon_0\epsilon)^{1/2} \quad \ldots\ldots\ldots\ldots\ldots \quad (2.9)$$

Relation (2.9) is the reduction of the Poole-Frenkel barrier. The resultant barrier would be $(\phi_{PF} - \Delta\phi_{PF})$.

Thus the Poole-Frenkel emission current density J_{PF} in the presence of the field can be expressed by the following relation

$$J_{PF} = e\mu n_c E \ \exp \ [-(\ \phi_{PF} - \Delta\phi_{PF})/2KT] = J_0 \ \exp \ ((\Delta\phi_{PF}/2KT) \quad \ldots \quad (2.10)$$

where

$$J_0 = e\mu n_c E \ \exp \ (\phi_{PF}/2KT) \quad \ldots\ldots\ldots\ldots\ldots \quad (2.11)$$

In equations (2.10) and (2.11) μ is the electronic mobility and n_c the effective density of states in the conduction band of the insulator. The Poole-Frenkel field-lowering coefficient β_{PF} is the coefficient of $E^{1/2}$ on equation (2.9) and it may be given by

$$\beta_{PF} = (e^3/\pi\epsilon_0\epsilon)^{1/2} \quad \ldots\ldots\ldots\ldots\ldots \quad (2.12)$$

Equation (2.10) is the original Poole-Frenkel model. Mahalingam *et al* (33). measured the temperature dependent conductivity of LaF_3 films in the Al-LaF_3-Al sandwich structures in the temperature range 300-470K and at high electric field ($>10^6$ Vm^{-1}). They obtained the good quantitative agreement with this Poole-Frenkel model Chari *et al.* (31) carried out D.C. measurements in the Al-Al_2O_3-Al sandwich devices having Al_2O_3 thickness in the range

800-2000 Å. The Poole-Frenkel conduction mechanism is operative in these devices. Anwar *et al.* (43) investigated Al-M_0O_3-Al having M_0O_3 film - 1000 Å thick in the temperature range 193-393K and Schottky and Poole-Frenkel models were compared with the experimental values of ß Measurements of current voltage characteristics in SiO, Al_2O_3 and Ta_2O_5 thin films of thickness range 400-7000 Å (8) are found in qualitative agreement with the Poole-Frenkel model (eqn. 2.10). But the resulting constant ß was found somewhat smaller than β_{PF} (eqn. 2.12) and in some cases in near agreement with the Schottky ß (eqn. 2.2).

It is apparent from the stated insulator thickness that the conduction mechanism would be bulk-limited whilst ß favours the Schottky value. To explain this anomaly three alternative modifications of the Poole-Frenkel model have been proposed. Among these three modifications one model is based on the hypothesis of the presence of discrete trapping levels, the second one is based on the compensation within the materials and the 3rd one includes the mobile donor concept.

The first explanation of the anomalous value of the constant ß is due to Simmons (87). He proposed a model based on neutral trapping centers and field assisted thermionic emission from donor centers. His model is shown in (Fig. 2.4). In his model he firstly determined the position of the Fermi level by equating the number of electrons missing from donor centers to the number of occupied traps assuming the number of electrons in the conduction band to be negligibly small. He then estimated the current density given by

Documentation Section
Document N. ...D-1901
Date....10.10.98.

Where $J_0 = e\mu n_c E\ (n_d/n_t)\ \exp[-(E_d + E_t)\ /\ 2KT$ In this expression n_d, n_t, E_d, E_t,E_d are the concentrations and energy levels respectively of donor and trapping centers. It is seen from equation (2.13) that the field lowering coefficient is now $\beta_{PF}/2$ ($\beta_{PF}/2$), although the conductivity is not electrode-limited.

This modification of the normal Poole- Frenkel model helps to explain the experimental results of several workers (27). Stuart (37) has shown that his bulk-limited I_s-V_s characteristics could be interpreted in terms of equation (2.13).

The second explanation of anomalous ß is due to Yeargan and Taylor (26). Their model is based on compensation of donors. They assumed the presence of acceptors, the concentration of which is smaller than that of the donors. The derived current density is similar to the expression (2.13). The proposed model is displayed in (Fig. 2.5). This model has been used to explain the experimental results of Anwar and Hogarth (41) on films of M_oO_3 / In_2O_3 materials.

The third explanation of the anomalous value of ß is due to Hill (87) who made a detailed analysis of electrical conduction in amorphous solids. The basis of his analysis is the ionization of local defects by an applied field. He derived an expression of a generalized current J of the form

$J = \alpha^2\ \mathrm{Sinh}\alpha$ ....(2.14)

or

$J \infty \alpha^{-1}\ (\alpha\ \mathrm{Cosh}\alpha - \mathrm{Sinh}\alpha)$ ....(2.15)

Where J is given by

$J = IT^{-n}\exp\ (E_i/KT)$ ....(2.16)

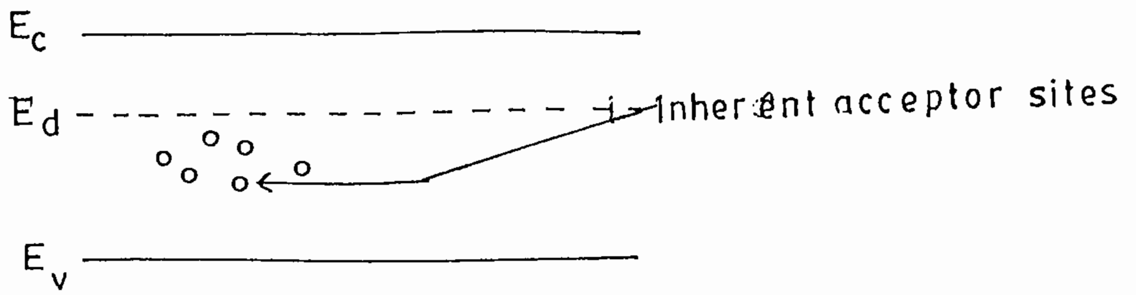

Fig.2.5. Inherent acceptor sites.

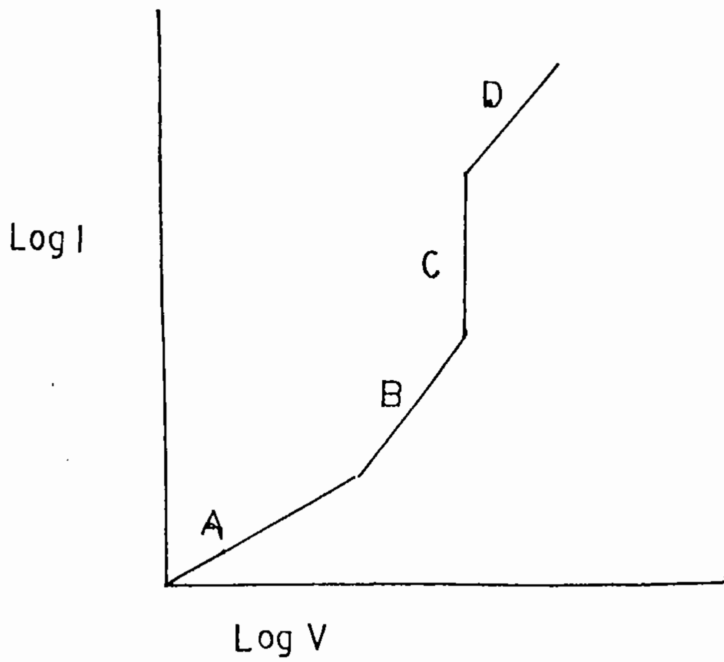

Fig.2.6. SCL I-V Characteristics.

E_i is the ionization energy of the centre and α is $\beta E^{1/2}/KT$. Equation (2.14) corresponds to emission from the donor centre occurring along the electric field direction with 'n' equal to 4 in equation (2.16) whereas equation (2.15) corresponds to spherically uniform emission from the centers in which case 'n' is equal to 3 in equation (2.16).

To explain the anomalous value of β, Hill (87) assumed that donors and traps co-exist. He also assumed that the density of ionized donors is a small fraction of the total density of ionizable donors. If this is the case then ionization of a donor by Poole-Frenkel emission can stimulate further ionization by other processes (other than Poole Frenkel emission). The initial ionized donor can act as a capture centre for the electron released from the second donor giving rise to an effective mobile donor and an anomalous value of β. Hill has expressed β_{AN} in terms of the normal β_{PF} by the relation

$$\beta_{AN} = \beta_{PF} \left(2V_e - V_n \right) / 2V_e \quad \ldots\ldots\ldots\ldots\ldots\ldots (2.17)$$

Where V_e and V_n are the velocities respectively of the free carrier and mobile donor. As the ionization of the second donor must always be dependent on the availability of the first donor it is unlikely that $V_n > V_e$ so that the range of the anomalous Poole-Frenkel constant is from β_{PF} to $\beta_{PF}/2$ ($\approx \beta_s$) as observed experimentally by Jonscher (87).

Jonscher and Hartke (87) have extended Hill's model to a three- dimensional well over which all emission probabilities have to be integrated. Writing $e\beta_{PF}E^{1/2}/KT = S$, they obtain a modified emission probability P given by

$$P = p_o S^2 (S-1) \exp(s) + 1 \quad (2.18)$$

Where p_o is the probability of escape in any direction in the absence of the electric field, By contrast, the simple Poole-Frenkel model gives

$$P_{PF} = P_o \exp(s)/2 \quad (2.19)$$

The modification statement from the concept that the maximum barrier lowering $\beta_{PH}E^{1/2}$ occurs in one particular direction only in space; other directions present a higher energy barrier to electron flow. After release from the donor centre the change carrier faces one of the two possible situations. In one case the carrier may be assumed to be trapped by the nearest centre downstream. In this case the distance travelled is independent of the applied electric field and the current is therefore directly proportional to the probability of emission P. i.e., $I \propto P$. For large values of S we obtain in this manner

$$I = I_o \exp(s)/S = Io\,(KT/\beta_{PF}E^{1/2}) \exp(\beta_{PF}E^{1/2}/KT) \quad (2.20)$$

one would thus expect in the limit of high fields to obtain a straight line with the appropriate slope (β_{PF}/KT) by plotting $\log(IE^{1/2})$ versus $E^{1/2}$ graphs.

The second possible assumption regarding the flow of current is to postulate that the liberated carriers travel for a constant period of time before being re-trapped. This would lead to a relation

$I \propto EP \propto S^2P$

Thus in this case the plot of $IE^{-1/2}$ versus $E^{1/2}$ should have the limiting logarithmic slope β. Servini (87) tested both hypotheses experimentally and observed fair agreement with the former, i.e. re-trapping at the nearest site is the most likely mechanism.

Another development on previous models in due to Hall (87). Hall assumed that an electron can exist in either the ground state of the donor centre or states localized at sites in the material. These sites are not necessarily centered on atoms, the only assumption about them being that they occur at a high density. He also ignored effects due to tunnelling. Hall arrived at two solutions for the emission current from Poole-Frenkel centers. They are

$I_1 \propto \exp\ (2\beta E^{1/2}-\phi)/KT$ ....(2.21)

and

$I_2 \propto \exp\ (2\beta E^{1/2}-\phi)/KT$ ....(2.22)

I_1 is appropriate above room temperature whereas I_2 should be used below room temperature. This model was applied to the results of Anwar and Hogarth (41) on thin films of MoO_3/In_2O_3 materials. It has particular success in explaining the variation of β with temperature.

2.1.1.3. Distinction Between Schottky and Poole-Frenkel emission.

Both Poole-Frenkel and Schottky emissions furnish linear graphs of log J_s versus $E^{1/2}$ over the range of electric fields employed experimentally ($\approx 10^6$ to 10^8 Vm^{-1}). The gradient of the linear region may be of roughly the same value. Both emission processes are likewise exponentially dependent on 1/T. These criteria are insufficient, to distinguish the two emission processes. However, considering a number of factors simultaneously it is possible to discriminate between the two emission processes. These are described below:

i) The height of the barrier at the contact for a wide band gap insulator is expected to be above 0.8ev whereas much low activation energies are indicated with bulk-limited emission.

ii) The two emission characteristics have different voltage and temperature dependencies. For Schottky emission $J_s \propto T^2 \exp(\beta_s E^{1/2}/KT)$. A graph of $\log(J_s/T^2)$ versus 1/T may be drawn at given electric field E and for a given temperature T, a plot of Log J_s versus $E^{1/2}$ can also be drawn. For Pool-Frenkel emission $J_{PF} \propto E \exp(\beta_{PF} E^{1/2}/2KT)$. The corresponding graph is Log J_{PF} versus 1/T at a given field E and for a given temperature T. Log (J_{PF}/E) versus $E^{1/2}$ may be drawn.

iii) The current characteristics of an MIM device using metals with different work functions will be highly asymmetric for schottky emission and symmetric for Poole-Frenkel emission.

iv) The bulk resistivity for thin-film ($\approx$ 10 to 100 nm) devices should be very small in the case of bulk-limited conduction and it should be large for very thick film (1000 nm or above) devices.

2.1.1.4. Space-charge-Limited (SCL) flow.

A space-charge will be built up within the insulator if there is an inexhaustible supply of free carriers in the dielectric near the injecting electrode. Current flowing through the insulator will then saturate. For low values of potential difference, ohm's law will be obeyed if the injected carrier density is lower than the thermally generated free carrier density ηo and the current density J_{sc} is given by

$$J_{sc} = en_o\mu\ v/d \quad (2.23)$$

Where V is the applied (DC) potential difference across the device and 'd' the insulator thickness. When the injected carrier density is greater than the free carrier density the current becomes space-charge-limited. The following two conditions need to be satisfied in order to observe SCL current flow of significant magnitude :

(i) at least one of the two electrodes must make an ohmic contact with insulator, and (ii) the insulator must be relatively free from trapping defects.

The mechanism of SCLC in solids was first proposed by Mott and Gurney (87). They established an expression for the current density J_{sc} for the simple case of single carrier trap-free SCLC in an insulator as

$$J_{sc} = \frac{9}{8} \frac{\mu\epsilon\epsilon_o V^2}{d^3} \quad (2.24)$$

Where the symbols have their usual meanings. It is seen from equation (2.24) that I_s is directly proportional to V^2 and inversely

proportional to d^3. Equation (2.24) predicts much high currents than are observed in practice and also that SCLC is temperature insensitive.

These predictions are contrary to observation. These deviations from the simple trap free theory are readily accounted for when a more realistic insulator, that is, one which contains traps is considered. Rose (87) enunciated the theory of SCLC in defect insulators. In the presence of traps, a large fraction of the injected space charge will condense therein which means that the free-carrier density will be much lower than in a perfect insulator. Furthermore, since the occupancy of traps is a function of temperature, the SCL current will be temperature dependent.

If the insulator contains n_t shallow traps, all assumed to be at the same energy level E_t below the bottom of the conduction band, the ratio Θ of the free charge to the trapped charge is given by

$$\Theta = (n_c/n_t)\exp(-E_t/KT) \quad \ldots\ldots\ldots\ldots\ldots\ldots (2.25)$$

Including the effects of shallow traps, the current density

$J_{(SC)T}$

is given by

$$J_{(SC)T} = \frac{9}{8}\,\frac{\mu\epsilon\epsilon_0\Theta V^2}{d^3} \quad \ldots\ldots\ldots\ldots\ldots\ldots\ldots\ldots (2.26)$$

As Θ is a very small temperature - dependent quantity the inclusion of shallow traps in the insulator is capable of accounting the experimental observations. The traps will be filled

up if sufficient charge is injected into the dielectric and the current density in the device will again be given by the Mott-Gurney equation. The voltage at which this occurs is called the trap-filled-limited (TFL) voltage V_{TFL} expressed by

$$V_{TFL} = en_t d^2/2\epsilon_0\epsilon \quad \ldots\ldots\ldots\ldots\ldots\ldots\ldots (2.27)$$

Fig. 2.6 presents the SCL I-V characteristics for an insulator containing shallow traps. It is seen from this figure, that there are four distinct zones. These are : Zone-A ohmic, Zone-ß governed by a modified Mottand Gurney law Zone-C a trap-filled-limited region and finally Zone-D governed by the trap-free Mott and Gurney law.

Normally the traps are not localized in shallow levels as considered above and the form of the space-charge law will depend on the nature of the trap distribution. For a trap distribution whose density decreases exponentially as the energy from the band edge increases, the current density for the applied potential difference V is given by (87).

$$J(sc)_T = (e\mu n_c)(\epsilon\epsilon_0 T_x K)^x (V^{x+1}/d^{2x+1}) \ldots\ldots\ldots\ldots (2.28)$$

Where x is a parameter which characterizes the particular distributing of traps and T_x is the temperature used to characterize the trap distribution.

Single-Carrier-Space-Charge-limited-Currents have been observed in many insulators and semi-conductors. Nazar (28) has reported space-charge-limited conduction in Si_3N_4, Arya *et al.*(29) in Bi_2O_3 , Chari *et al.*(31) in Al_2O_3, Signerski *et al.*(32) in

tetrcene, Herdt *et al.*(36) in SiO, Wiktorczyk *et al.*(35) in Yb_2O, Moreno *et al.* (44) in tetrafluore-ethylene-hexz-fluoropropylene copolymer (Teflon FEP), Gould *et al.*(45) in cdTe, Subbarayan *et al.*(45) in Perylene and Shafai *et al.*(46) in lead phthalocyanine (pbpc) thin films.

2.1.1.5 D.C. Hopping.

In the earlier discussion it has been observed that depending on the energy electron transport can occur from the valence band into the conduction band of an ideal insulator. But in practice most of the insulators contain certain amounts of traps. Hence it is not necessary to raise the electron into conduction band of the insulator for electrical conduction, rather electron can hop from one trap to another giving hopping conduction. There are two types of hopping conduction: (i) D.C. hopping conduction and (ii) A.C. hopping conduction.

In this section D.C. hopping conduction will be treated. Both theoretical and experimental investigations of D.C. hopping conductivity began in 1950. Hopping probability P_{hop}. may be expressed as the product of a tunnelling term and a phonon term as

$P_{hop} \propto \exp(-2\alpha R - W/KT)$ ....(2.29)

Where R is the average transition distance independent of the energy difference W between the inital and the final states. The two types of D.C. hopping are; (i) nearest neighbour hopping (also called thermally activated hopping) and (ii) variable range hopping.

The expression for the nearest-neighbour D.C. hopping conductivity σ_0 at higher temperatures (30-300K) is given by

$\sigma_0 = A \exp(-W/KT)$ ....(2.30)

Where A is a constant and the relevant density of states at the Fermi level is given by

$N(W_F) = (12R^3W)^{-1}$ ....(2.31)

Several workers observed this effect in antimony films of thickness 170-14000 Å in the temperature range 30-160K. Efendiene *et al.*(39) and Knotek *et al.*(48) studied D.C. hopping in Bi_2O_3 and a-Ge films respectively. Anwar *et al.*(41) discussed D.C. hopping in MoO_3-In_2O_3 films.

At sufficiently low temperatures, variable-range hopping is always to be expected. The variable-range hopping conductivity σ is given by

$\sigma_i \propto \exp(-B/T^{1/4})$ ....(2.32)

Where B is a constant dependent on the density of states and degree of localization of the states through which hopping occurs. A number of observations of variable-range having in amorphous semi-conductors have been reported in the literature since Mott's enunciation of the model (equation 2.32).

Hill (49) discussed variable-range hopping in amorphous semi-conductors. According to Wiktorczyk *et al.*(38), the activation energy ΔE for Yb_2O_3 was 0.53eV in the temperature range 300-390K and 0.98eV in the temperature range 440-500K. The variation 0.53-0.98 eV in the activation energy indicates the existence of variable-range hopping in Yb_2O_3.

2.1.2 A.C. Conduction Mechanism.

Measurements of A.C. Characteristics such as impedance, Z, phase angle ϕ, conductance G, capacitance C and dielectric loss factor $\tan\delta$ as a function of frequency and temperature determine the conduction mechanism in MIM structures in both the planar and sandwich configurations.

Frequency dependent barrier resistance R_b is split into two parallel resistances, one is $R_{D.C}$ independent of frequency and the other is $(AW)^{n-1}$ dependent of frequency. R_p (the phonon assisted hopping resistance), r (the resistance due to the dielectric loss) and C_p (capacitance of the intergranular barrier). Two equivalent circuits (one is in series mode and the other in parallel mode) containing R_m (resistance of the metal-oxide particles), R_p, R, R

and C_p are shown in Figures 2.7(a) and (b).

i) **R_p and R_b In Series Mode.**

From Fig. 2.7(a) we get the circuit impedance as

$$Z = Z_1+Z_{23} \quad \ldots\ldots(2.33)$$

Where

$$\frac{1}{Z_{23}} = \frac{1}{Z_2} + \frac{1}{Z_3} \quad \ldots\ldots (2.34)$$

and

$$Z^{`} = R_m, \; Z_2 = R_p+R_b, \; Z_3 = R+ \frac{j}{Wc_p} \quad \ldots\ldots (2.35)$$

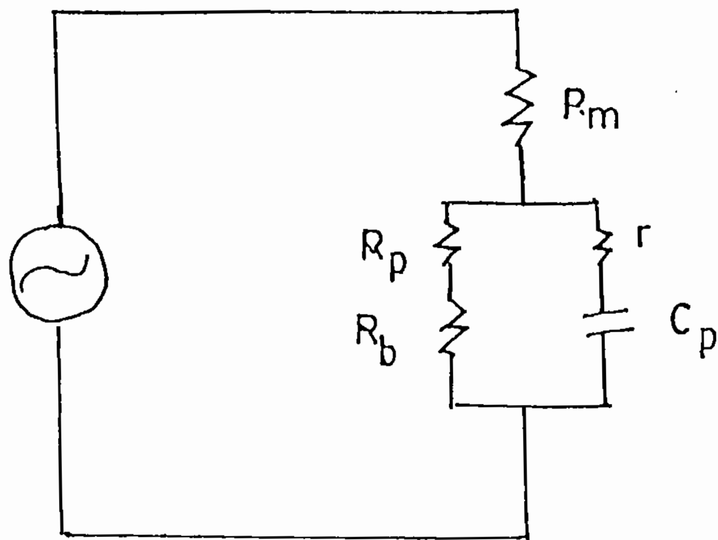

(a)

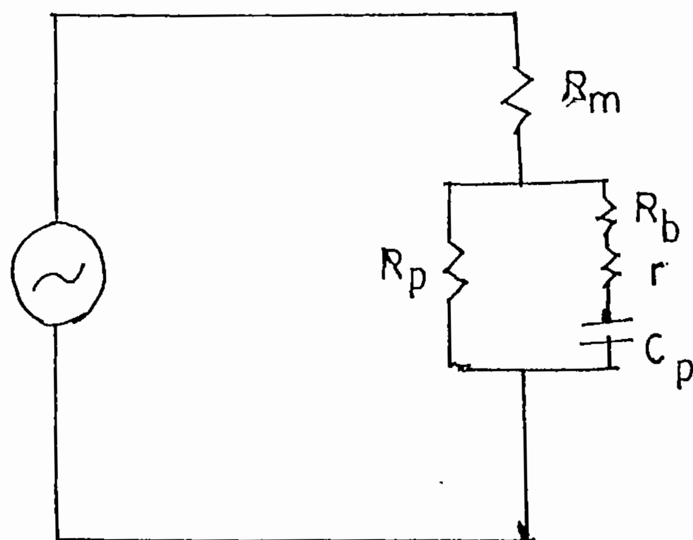

(b)

Fig.2.7 (a) R_p and R_b are in series mode (b) R_p and R_b are in parallel mode.

At very low frequency, the term $R_m/r^2W^2Cp^2$ being of the order of 10^{19} and is very much larger than R_m. Thus the series mode impedance is given by

$$=R_m + \frac{[1+(R_p+R_b)rw^2C_p^2] \qquad (R_p+R_b)}{[1+(R_p+R_b)rw^2Cp^2]+(R_p+R_b)^2w^2C_p^2}$$

$$+ \frac{jWC_p(R_p+R_b)^2}{[1+(R_p+R_b)^2w^2C_p^2]^2 \ [R_p+R_b]^2w^2c_p^2} \quad \ldots\ldots\ldots\ldots (2.6)$$

The conducting particles in the sample get aligned in specific patterns depending on the firing time, temperature and pattern. These patterns form the capacitor, Hence depending on the type of capacitor formed due to these conducting particles, the impedance and hence the capacitance of the sample can be studied elaborately as a function of frequency. Assuming zero correlation, the capacitance of a parallel plate capacitor

$C_p = \epsilon\epsilon_0 A/Df$ .... (2.37)

Where ϵ is the dielectric constant of the material. ϵ_0 is the permittivity, A the area of the plate, D the distance between the plates and f the size factor. Therefor, for thick films,

$C_p = K\epsilon\epsilon_0 A / Df$ ....(2.38)

Where K is a correlation constant. Then

$C'_p = K'\epsilon_0 A/Df$ ....(2.39)

Where

$K' = K\epsilon$ ....(2.40)

On the other hand, for a spherical capacitor formed by the conducting particles of the sample the capacitor will be

$$C_p = 4\pi n \epsilon \epsilon_o d \; 2(t+d)/2t+d) \quad (2.41)$$

Therefore for thick films

$$C'_p = 4\pi n K \epsilon \epsilon_o d \; 2(t+d)/2t+d) \quad (2.42)$$

$$\text{or } C'_p = K' C_p \quad (2.43)$$

Where n is the number of particles per unit volume, t is the average site of the particles and d is the thickness of the barrier.

We can also derive an expression for the cylindrical capacitor. In this case the capacitance is given by

$$C_p = \frac{4\pi\epsilon\epsilon_o D}{2K} [n_1/l_n\{2(t+d)/d\}+n_2/l_n[\{4(t+d)+2l\}/l]] \quad (2.44)$$

and $$C'_p = \frac{4\pi\epsilon\epsilon_o D}{2K} [n_1/l_n\{2(t+d)/d\}+n_2/l_n[\{4(t+d)+2l\}/l\}] \quad (2.45)$$

or

$$C'_p = K' C_p \quad (2.46)$$

Where l is the average length of the cylinders, n_1 and n_2 are the concentration of cylinders, type1 and type 2 respectively.

ii) $R_p$and R_b In Parallel Mode.

The equivalent circuit diagram for R_p and R_b in the parallel mode is shown in Fig.2.7(b). The impedance of the circuit can be written as

$$Z = Z_1 + Z_{23} \quad (2.47)$$

Where

$$\frac{1}{Z_{23}} = \frac{1}{Z_2} \quad \frac{1}{Z_3} \quad \ldots\ldots\ldots\ldots\ldots \quad (2.48)$$

and $Z_1 = R_m$, $Z_2 = R_p$ and $Z_3 = R_b + r + \frac{j}{C_p w}$ . . . . (2.49)

Then

$$Z = R_m + \frac{R_p[1+R_p(R_p+r)w^2C^2_p}{[1+R^2_b(R_b+r)^2w^4C^4_p+R^2_pw^2C^2_p} + \frac{jR^2_pwC_p}{[1+R^2_p(R_b+r)^2w^4C_p^4+R_p^2w^2C_p^2} \quad (2.50$$

As before in this case as well three possibilities will rise for the formation of types of capacitors.

Same theories and models could be used for the dielectric materials as well as ferro-and para-electric materials.

Kannan *et al.*(61) defined the temperature coefficient of capacitance (TCC) and temperature coefficient of permittivity (TCP) as follows :

$$TCC = \frac{1}{C_p} \quad \frac{dC_p}{dt} \quad \ldots\ldots\ldots\ldots\ldots \quad (2.51)$$

and

$$TCP = \frac{1}{\epsilon} \quad \frac{d\epsilon}{dT} \quad \ldots\ldots\ldots\ldots\ldots \quad (2.52)$$

The linear expansion coefficient can be evaluated from

$\alpha = TCC-TCP$ . . . . (2.53)

TCC can also be calculated using the relation

$TCC = A \tan\delta - \alpha\epsilon$ . . . . (2.54)

Where A is a constant ($A = 0.05 \pm 0.01/K$)

Kannan *et al.* found the values of TCC and TCP to be 646 ppm/K and 623 ppm/K respectively for Nd_2O_3 films in the $Al-Nd_2O_3-Al$ sandwich structures at 1kHz and at room temperature. ϵ is the dielectric constant. The value of α is 23 ppm/K.

Models proposed by Halder *et al.*(54) for the calculation of impedances are rather lengthy. The following approximations were made. R_p = 20Ω, R_m = 30KΩ, r = 1KΩ and C_p = 1F, $R_b(w) \approx 1/w$, $c(w)=1/w$ and $\phi=1/w$. The sudden rise of R and C at about 10^5 Hz could not be explained with this model. In some cermets including some commercial resistors. This type of behavior means presence of some large voids in the sample.

The phase angle according to Halder *et al.* can be defined as

$$\phi = \tan^{-1}(\mathrm{Im}\ Z/\mathrm{Re}Z) \quad \ldots\ldots\ldots\ldots \quad (2.55)$$

Thus ϕ is frequency dependent.

The A.C. conductivity can be expressed as

$$\sigma(w) = \sigma_{d.c.}+\sigma_{a.c.}(w) \quad \ldots\ldots\ldots\ldots \quad (2.56)$$

Where the true A.C. part of the conductivity should be

$$\sigma_{a.c.}(w) \sim w^n \quad \ldots\ldots\ldots\ldots \quad (2.57)$$

Where n is close to unity.

A.C. hopping conductivities have been discussed in details in the literatures (47-50) Hossain (51) discussed dielectric properties in T_i Mgo and Gd/Mgo films. Jayaraj *et al.*(52) observed A.C. properties in Eu_2O_3 films, Dharmadhikari *et al.*(53) in Nd_2O

Mishra *et al.*(56) in tourmaline, Arora *et al.*(57) in $CuWo_4$, Parkhutik *et al.*(58) in Al_2O_3. Shabalov *et al.*(59) in SiO_x, Sathyamoorthy *et al.*(60) in YF_3,

Kannan *et al.*(61) in Nd_2O_3, Lhotska *et al.*(62) in ferroelectric, TGS-type crystals, Salam (63) in Indium-Tin-Oxide films, Sawaby *et al.*(65) in sodium accetylacetonate compound,

Heidinger (65) in ceramic materials, Nadkarni *et al.*(66) in MoO_3 films, Khurana *et al.*(89) in a-$Ge_{17}Te_{83}$ and Dutta *et al.*(90) in Yb_2O_5 films, Al-Dhahan *et al.*(97) in CeO_2/SnO_2 films, Despujols(105) in Al_2O_3 films, Ettaik *et al.*(106) in polyparaphenylene, Geddes *et al.*(107) in 22-tricosenoic acid, Islam *et al.*(108) in Sio/B_2O_3, Soukup *et al.*(128) analysed A.C. properties of SIC films, Wiktorczyk (129) in Dy_2O_3 films and Bhosale (132) in V_2O_5 films.

2.2 Electroforming In MIN Structures

MIM structures in both planar and sandwich forms exhibit anomalous electrical properties. By the application of a D.C. bias in the range 2-15V, an MIM device under certain conditions undergoes a forming process during which the electrical conductivity of the device is increased by a few orders of magnitude and its current voltage (I_s-V_s) characteristic shows a maximum in the I_s-V_s graph. A formed MIM device exhibits VCNR and CCNR, electron emission (EE), electroluminescence (EL), Switching and memory phenomena. Several models have been suggested for explaining these features. These models are broadly classified into two categories. They are :

(i) Models on homogeneous penetration of the current carrier

(ii) Models on filaments formation.

2.2.1 Models Based on Homogeneous Penetration.

2.2.1.1 Hickmott's Model.

Hickmott was the Pioneer in interpreting the anomalous behavior of MIM devices. His model is a qualitative one. He assumed that the anodically formed insulator layers contained considerable impurity so that the impurity band appears approximately at the Fermi level in the insulator gap. The forming process involved ionisation of the impurity thereby enabling an electrical current to flow through the impurity band. For the particular case of Al_2O_3 it has been experimentally derived that the gap width E_g=8.2ev and E_c-E_F =4.1ev, E_F-E_H=2.3eV, E_H-E_V =1.8 eV, E_F-E_v=4.1ev, where E_c, E_v are the bottom of the conduction band and top of valence band respectively and E_F is postulated as an acceptor level E_H is the Fermi leave. The largest port of V_s applied to the sample is probably situated at the negative electrode and the remaining insulator layer is almost without an electric field. When V_s reaches a value of 1.8V (the threshold for electroluminescence and electron emission), in the high field region, free holes are created at the top of the valence band by electrons tunnelling to the E_H acceptor level. Free holes recombine with electrons from the impurity band. This can cause light emission (electroluminescence) or excite electrons to the conduction band by Auger processes. When V_s reaches a value of 2.3V the electrons start tunnelling from the acceptor level to the impurity band and the conductivity decreases as a result. At V_s=2.8V the processes of ionization and neutralization in the impurity band are equal and a maximum in the I_s-V_s characteristic appears followed by the VCNR region if V_s is

further increased. Electron emission arises from electrons passing through the top electrode on obtaining an energy of 4.1eV in the Auger process. Hickmott did not believe that electron arose by photoemission from the top Au electrode caused by electroluminescence but some photo-excitation from Al electrode is possible. Hickmott did not consider the influence of the surrounding atmosphere and temperature. No information about switching is available in his model.

2.2.1.2 Simmons, Verderber and Eales Model.

Simmons *et al.*(3) have suggested that the forming process is caused by the homogeneous introduction of the ions of the upper electrode (from nobel metal =Ag. Au, Cu, Pt, etc.) into the dielectric where the impurity band originates because of great disorder or amorphous structure of the dielectric. In order to satisfy overall charge neutrality in the insulator, the ions (assuming them to be singly ionized) must drag into the insulator an equal number of electrons from the apposite electrode. Noble metal atoms act as donor centers and hence are neutral or positively charged depending on whether they are positioned energetically below or above the Fermi level of the insulator.

The noble metal 'donors' in an insulator having a crystalline structure would provide a discreate energy level in the forbidden band of the insulator. This would not be the case for an amorphous insulator for two reasons. First, because of the amorphous nature of the insulator, a noble metal ion does not have a uniquely defined environment. There will be found no consistency in nearest

neighbour and next nearest neighbour configuration etc. with the result that the potential energy of the ion within the lattice is not well defined. Secondly an amorphous insulator would be expected to contain a number of traps; some of these below a certain energy (Fermi level) will be occupied giving a net negative charge. The coulombic interaction between the negatively charged trap and the positively charged donor centre perturbs the potential energy of the donor centre. The overall result of these two effects produces a broad band of localized states within the forbidden energy gap of insulator as shown in Fig.2.8(a). This energy band extends within $\Psi_i-\Theta_i$ of the bottom of the conduction band where Ψ_i and ϕ_i are the energies of the bottom of the conduction band and top of the localized levels respectively measured from the Fermi level. At the electrodes there are depleted layers of Al-insulator and insulator-noble metal (≈Ag, Au, Cu, Pt, etc.), the barrier of the first one is denoted by ϕ_o. It is further assumed that the impurity density is so high that electrons penetrating the barrier ϕ_o can tunnel from one centre to another on levels at the same energy. The electrons for $V_s<\phi_i$ coming from the bottom metal electrode pass through the dielectric on the anergy level equal to the Fermi level in the bottom electrode.

When electrons with an energy $V_s>\phi_i$ cannot pass through the dielectric they reach only the point near the bottom electrode on the level ϕ_i from which they can be excited to the conduction band of the dielectric by an interaction with phonons Fig.2.8(c). Only electrons on level (a) create the conduction current and the maximum in the I_s-V_s characteristic appears for $V_s=\phi_i$. The electron

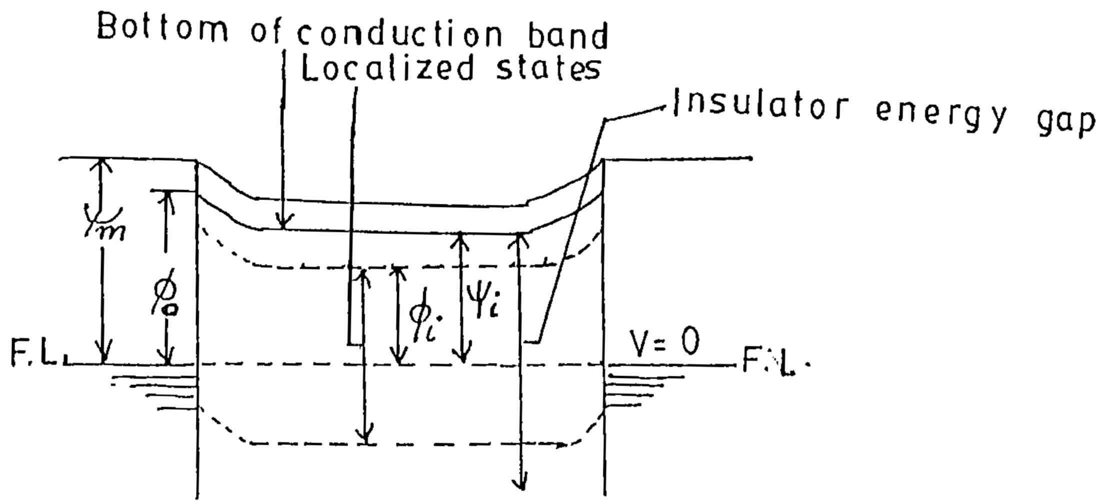

(a)

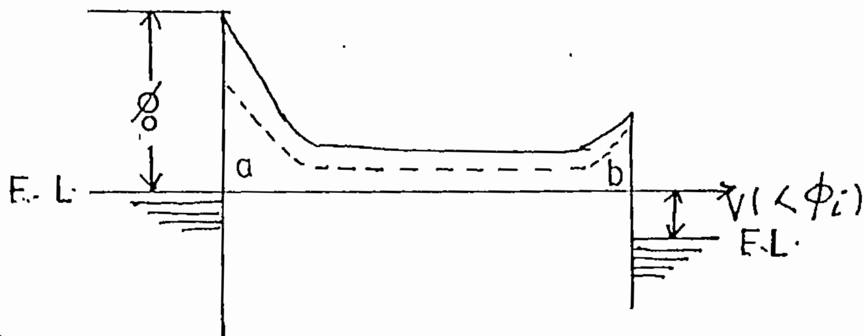

(b)

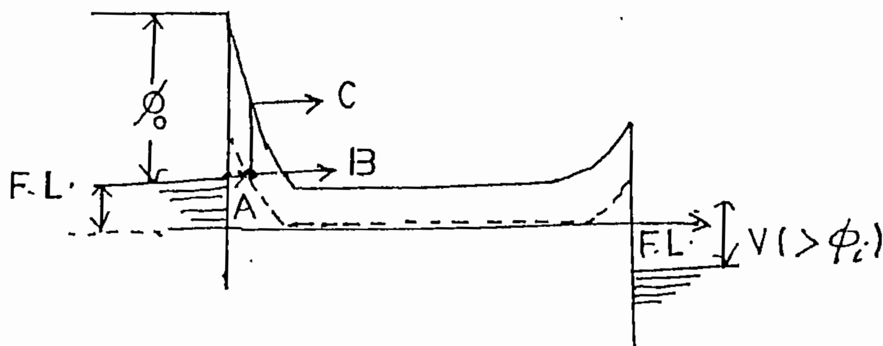

(c)

Fig.2.8. Energy diagram of formed MIM devices for various voltages. (a) $V = 0$, (b) $V < \varnothing_i$; (c) $V > \varnothing_i$.

emission for V_s less than that corresponding to the work function of the top electrode is explained by electrons obtaining excess energy from the Lattice of at least 1eV. Electrons coming to the top polycrystalline electrode undergo a scattering process on the planes of the noble metal crystallites. Electrons for V_s<8V are scattered back towards the insulator and must undergo further scattering events (e <———>e, e <———>p) before they are able to enter the vacuum through the edge of a pinhole. The process is accompanied by energy losses and is insufficient in directing electrons towards the pinhole edge. For the conditions V_s>8V an electron is scattered within the distance of the mean free path from the edge of the pinhole and then it enters into the vacuum without loss of energy. This is in agreement with the rapid rise in emission current above 8V in the I_s-V_s characteristics.

A hystersis in the I_s-V_s characteristics is called the memory state. Fig.2.9 (a,b,c) presents the electron storage mechanisms in the memory state. Fig.2.10(a) illustrates the energy diagram for the system operating with an induced memory.

2.2.1.3 Barriac *et al.* Model.

Barriac *et al.*(6) suggested that for $Al-Al_2O_3-Au$ sandwich structure under an increasing bias V_s at some value of the electrical field in the oxide breakdown will occur at the thinnest film region. The perforation of the top electrode is caused by local melting which results evaporation in the breakdown areas. Ions of the top electrode enter the cracks in the oxide. For bias V_s, $0<V_s<V_m$ the current I_s is determined by the motion of ions

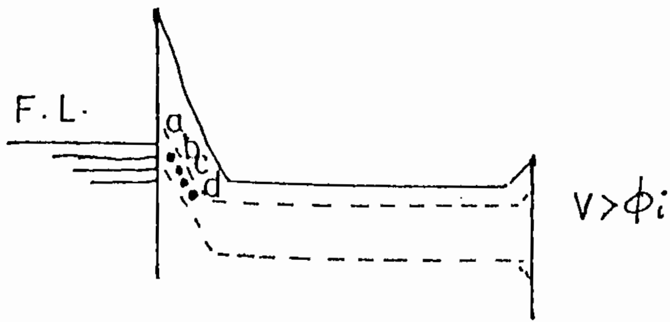

(a)

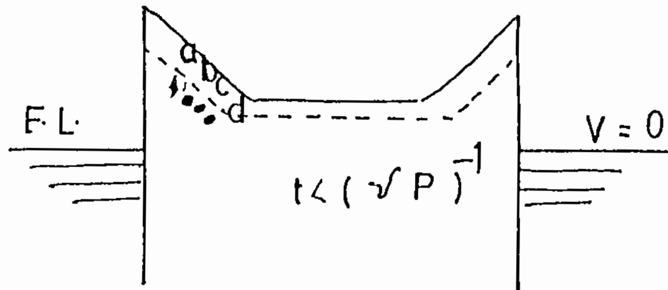

(b)

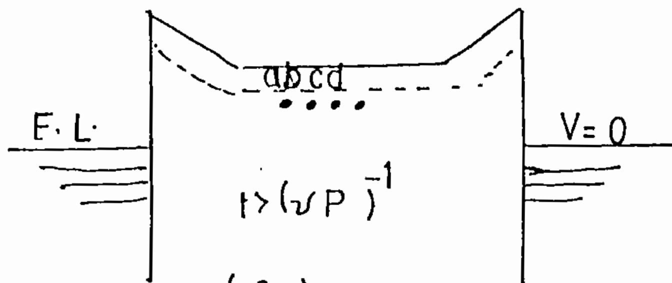

(c)

Fig.2.9 Energy diagrams showing the position of the stored charge relative to the Fermi levels (a) at a voltage bias of V volts (b) Immediately after voltage has been rapidly reduced to zero, (c) at time $t > (\nu P)^{-1}$.

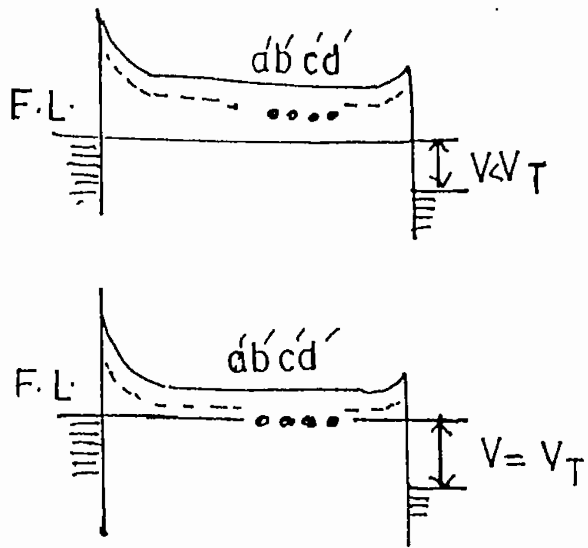

Fig.2.10 Energy diagram showing position of stored charge relative to Fermi level (b) before switching occurs (b) onset of switching.

towards the negative electrode along the surface of the cracks. In the vicinity of the negative electrode space charge of variable thickness is formed. At $V_s=V_m$ the space charge thickness reaches a minimum value and electron tunnel emission starts from the negative electrode followed by recombination of electrons with positive ions (neutralization of space charge). The charge recombination results in a decrease in the total current which is the difference between the ion and electron current. This causes the VCNR characteristics to appear in the I_s-V_s characteristic curve. The effect of O_2 is considered to arise from its penetration into pores and cracks, where it chemically reacts with ions of the upper electrode.

2.2.1.4 Greene, Bush and Rawlings' Model.

Greene *et al.*(8) proposed that the forming mechanism is a high-field electrolytic process in which anion vacancies are injected into the insulator. These vacancies give rise to localized conduction paths through the insulator. The model is presented for a hypothetical insulator MX consisting of M^+ and X^- ions.

Under low-field conditions the reactions at the anode and cathode (both assumed inert) are respectively

$$X^- \longrightarrow X+e^- \qquad (2.58)$$

$$M^+ + e^- \longrightarrow M \qquad (2.59)$$

with the amion after newtraliztion is given off as gas.

Under high electric field conditions a further cathode reaction is given by

(X vacancy)+e^- ——> (X vacancy with trapped electron) . (2.60)

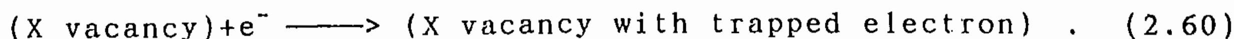

More vacancies are produced by the discharge of X^- ions at the

anode. The diffusion of vacancies under the influence of the electric field establishes chains of defect centers across the insulator.
Subsequently, the conduction occurs by the tunnelling of electrons through such chains of centers. The observed evolution of fluorine gas in devices with fluoride insulators can now be understood using reaction (2.58). Since atomic transport is involved the forming rate should decrease with temperature, as observed.

In the presence of an oxygen environment a third possible cathode reaction is

$$Y_2O_2 + ze^- \longrightarrow O^{2-} \quad \ldots\ldots\ldots\ldots \quad (2.61)$$

At sufficiently high pressures, reaction (2.61) is dominant over (2.60) and electroforming cannot occur. If the anode metal M is chemically reactive an alternative to reaction (2.58) may occur at the anode. viz.

$$M_a \longrightarrow M^n{}_a + n^{e-} \quad \ldots\ldots\ldots\ldots \quad (2.62))$$

If material enters the insulator by reactions (2.61) and (2.62) at a greater rate than being discharged by reactions (2.58) and (2.59), the insulator thickness will increase. This means that through (2.60) the forming process is weakened. Hence a less reactive anode material and very low ambient pressure are recommended for optimum forming.

Negative resistance and memory may be explained in terms of trapped space charge produced when the applied potential difference across the device is sufficient to give some of the electrons enough energy to leave the conducting path and enter the surrounding unformed dielectric.

This model accounts well for the forming in ionic crystals. It is not clear whether the mechanism can be adapted to other insulators such as SiO_2.

2.2.2 Filamentary Model.

2.2.2.1 Dearnaley, Morgan and Stoneham Model.

Dearnaley *et al.*(5) postulated that electroforming creates filamentary paths between the electrodes, the conduction being essentially ohmic. The filaments are considered to be not perfectly uniform but to have weak spots which determine their resistance. These filaments become heated by the flow of electrons since conduction must arise due to unusual interatomic spacing, interbond angles or defect configuration. In other words electrons will suffer phonon scattering particularly at the weak, hot spots of the filaments and the conducting chain may actually be ruptured. This is the novel aspect of the filamentary model that will account for negative resistance and memory properties of the formed layers. According to Pagnia (24) switching 'off' and 'on' states correspond to rapture of filaments due to Joule heating and re-growth of the filaments within a dead time respectively.

Once each filament bridges the gap between the electrodes, electronic conduction begins and Joule heating will occur. A local lattice temperature T is considered with each filament and assume that rupture will occur if T exceeds T_{max}. Thus the local temperature T is given by

$$dT/dt = \alpha^2 V^2(t)/P - (T-T_o)/\tau_c \quad \ldots\ldots\ldots\ldots\ldots \quad (2.63)$$

Where α measures the heating, τ_c characterizes the cooling and ρ is

the resistivity of each filament. From the steady state solutions of (2.63) at V only filaments with resistance greater than

$$\rho_{min} = \tau_c \alpha V^2/(T_{max}-T_o) \quad (2.64)$$

remain unfracttured. The total current is

$$I = \int_{\rho_{min}}^{\alpha} d\rho V\ P(\rho)/\rho \quad (2.65)$$

Where $P(\rho)$ gives the probability distribution of the various resistances and

$$\int_{o}^{\alpha} P(\rho)d\rho = 1 \quad (2.66)$$

Two features of $P(\rho)$ are immediately apparent. First, there are very few filaments with resistance below

$$\rho_T = \tau_c \alpha V^2_T/(T_{max}-T_o) \quad (2.67)$$

Since the devices can be cycled below V_T without showing signs of filaments breaking. Secondly there are very few filaments with resistances above $\rho_u = \tau_c \alpha\ V^2_u/(T_{max}-T_o)$ (2.68)

Where V_u is the voltage at which I(V) is a minimum. Above V_u the current is close to that of the unformed device and extra conduction mechanisms can be ignored. $P(\rho)$ can be derived from I(V) as

$$P(\rho)/\rho \approx d(1/v)/d(V^2) \quad (2.69)$$

This distribution is shown in Fig. 2.11(a). The apparently negative value of $P(\rho)$ for small ρ simply neflects the contribution of tunnelling at small voltages. Dearnaley *et al.*also showed a simple triangular distribution in Fig. 2.11(b) and in Fig. 2.12. They

showed that the I(V) characteristics for the two distributions are strikingly similar. The distribution of resistances in Fig. 2.11 is merely qualitative unless we can estimate N, the number of filaments per unit area. N was estimated roughly assuming that all filaments have the same resistance ρ. The initial resistance of the device per unit area is ρ/N, apart from small tunnelling effects and the filaments all burn out when $V \sim V_{max}$. Thus from equation (2.63) we obtain the following relation

$$\rho \sim \tau_c \alpha \; V^2_{max}/(T_{max}-T_o) \quad \ldots \quad (2.70)$$

The cooling time τ_c is estimated by considering each filament as a cylinder of radius 'd' and temperature T cooling to a cylindrical link of radius D and temperature T_o. D is taken to be the mean filament separation defined by $ND^2=1$ but could be smaller than this. It is then easy to show that

$$\tau_c \alpha = I_n(D/d)/4.68 \times 2\pi KL \quad \ldots \quad (2.71)$$

Where K is thermal conductivity of the insulator and L is the length of the filaments.

Deacnaley *et al*. postulated that electron emission is due to the generation of hot carriers by the high electric fields which exist at high-resistance spots in the filaments. Across some of these spots, the potential drop may very nearly equal the whole bias voltage. If the weak spot is close to the anode, electrons may be accelerated to nearly the full applied potential difference. This approach suggests, therefore, that emission should become particularly strong for potential differences close to the threshold voltage V_T, at which value filaments are beginning to rupture.

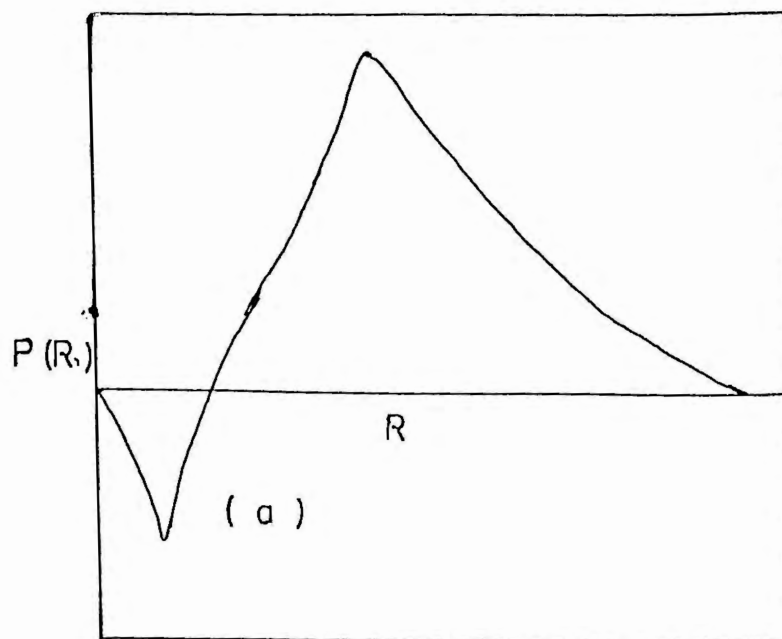

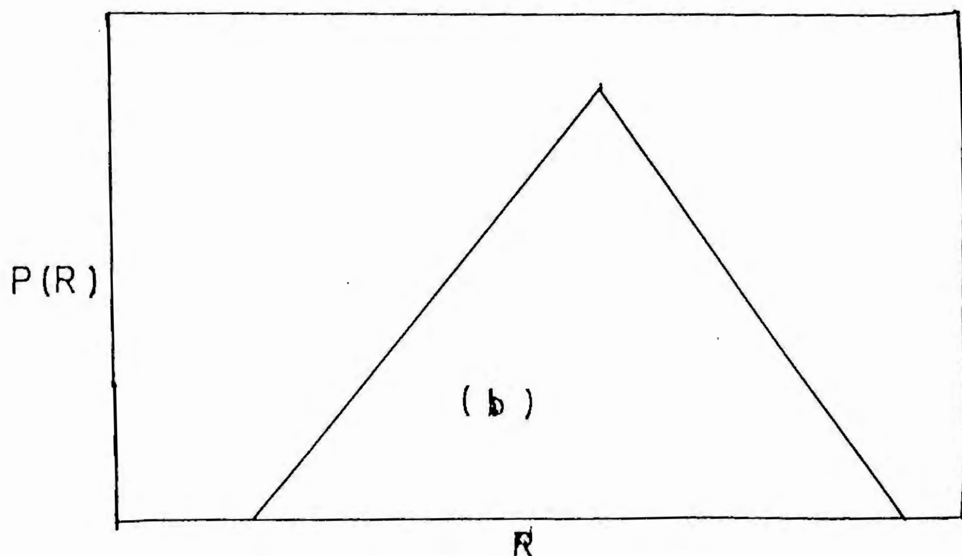

Fig.2.11(a) The calculated distribution of filament resistance deduced from experimental current-voltage behaviour. Negative values near the origin arise because tunnelling at the electrodes has been neglected (b) the simple triangular distribution of filament resistances assumed as an approximation in fitting the current-voltage characteristi

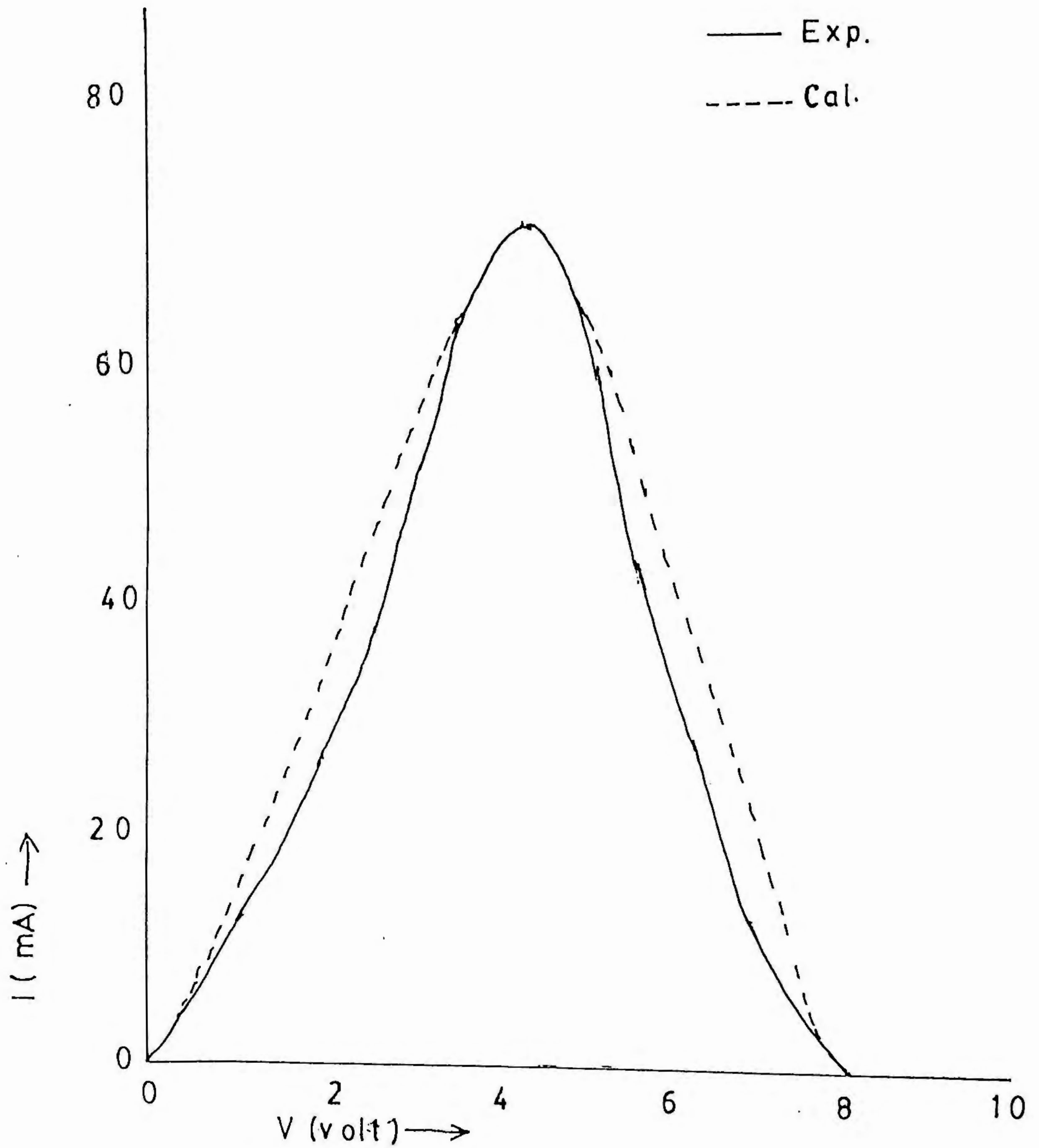

Fig.2.12 The low-frequency or dc behaviour calculated with the distribution of filament resistances.

2.2.2.2 Ralph and Woodcock's Model.

Ralph *et al.*(10) assume with Dearnaley *et al.*(5) that there exists an array of filamentary paths extending from one contact to the other of the MIM structure. Ralph *et al.* proposed that each filament contains an impurity band, which with the Fermi level is assumed to lie approximately in the centre of the forbidden gap of the insulator. They also proposed that due to non-uniformities in the initial layer, before forming this impurity band contains large variations in the density of centers. Due to this and to local fluctuations in the random excess potential V_0 there will be large variations in the mobility bandwidth and the density of states bandwidth. Regions of narrow mobility bandwidth are referred to as constrictions.

Each filament is considered to contain one dominant constriction. This represented in Fig. 2.13 as a symmetrical increase in the density of states bandwidth (E_I) and a corresponding decrease in mobility bandwidth (E_M). These dominant constrictions are assumed to be randomly distributed in position between the electrodes. Trapping in such a system may occur both within the filament in the localized levels and outside the filament in the surrounding unformed material. Those outside are spatially separated from the conducting non-localized levels in the impurity band and should behave differently from those within the filament.

Under small bias the current flow in a given filament is entirely determined by Iso-energetic tunnelling through the unrestricted centre region of the impurity band of Fig.2.13. This gives rise to an I_s-V_s relationship of the form

$I_s \alpha$ Sinhk V_s . . . . (2.72)

Where K is a constant.

As the bias voltage is increased further tilting of the bands occurs as shown in Fig. 2.14. As a result some electrons become trapped in localized states of the impurity band, as shown by arrow a. Over a limited range of potential differences a given filament may continue to conduct via these trapping states by either recombination, thermal degradation or field emission as shown, respectively, by arrows b,c and d until the filaments are switched off.

The VCNR in the I_s-V_s characteristic is explained in the following manner. Two types of traps have been indicated earlier- those within the filament and those outside it. There are also two ways in which these traps might be expected to cause a filament to stop conduction.

In the first process, when electrons, become trapped in the material surrounding the filament, a negative space charge is produced. This will induce a positive charge in the conducting part of the filament. If this occurs in a region where the mobility band is narrow (the constriction of Fig. 2.13), then this depletion of electrons can lower the Fermi level into the region of the localized states at the bottom of the band and the filament ceases to conduct. This situation is shown in Fig. 2.15.

In the second process the electrons may be trapped in the localized states within the constriction. This causes an increases in the random potential V_0 experienced by the states in this region and V_0/B is increased. Here B is the width of the energy band. If

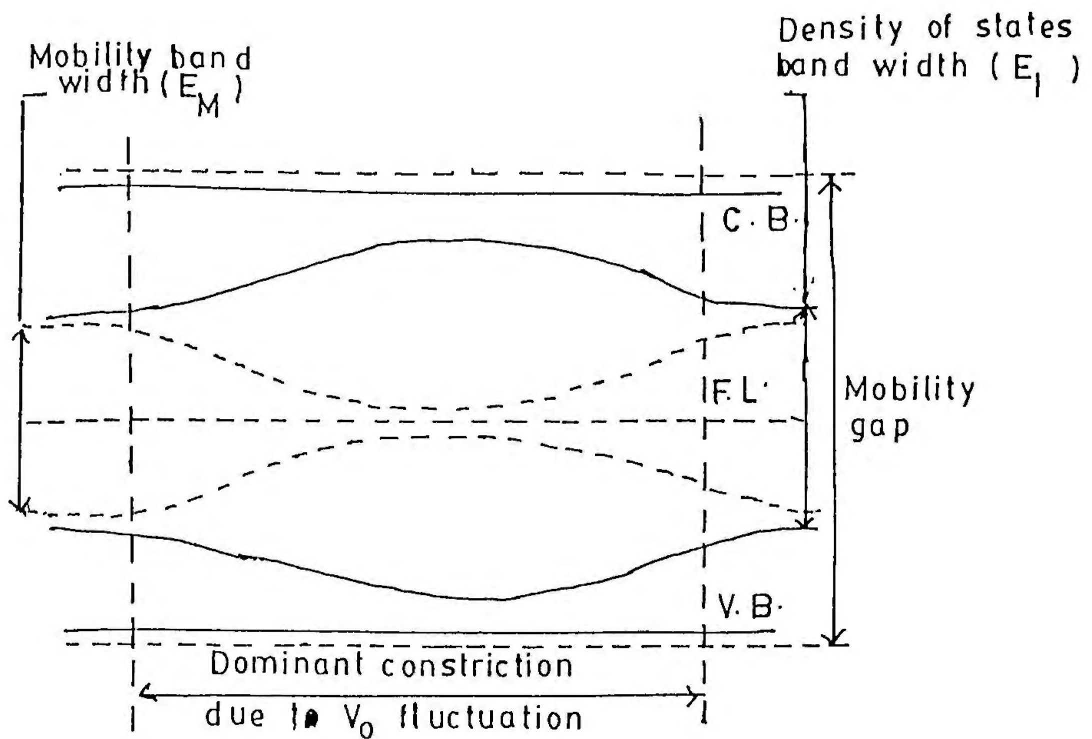

Fig.2.13 The suggested band diagram for a local V_0 fluctuation in a filamentary conducting region of a formed non-crystalline insulator.

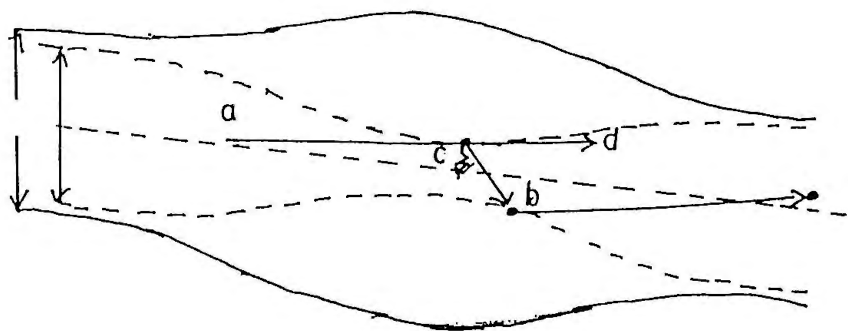

Fig.2.14 Some processes which may occur in the constriction in a formed conducting filament (a) iso energetic tunnelling into the region of localised states ; (b) radiative recombination (c) thermal degradation (d) field emission.

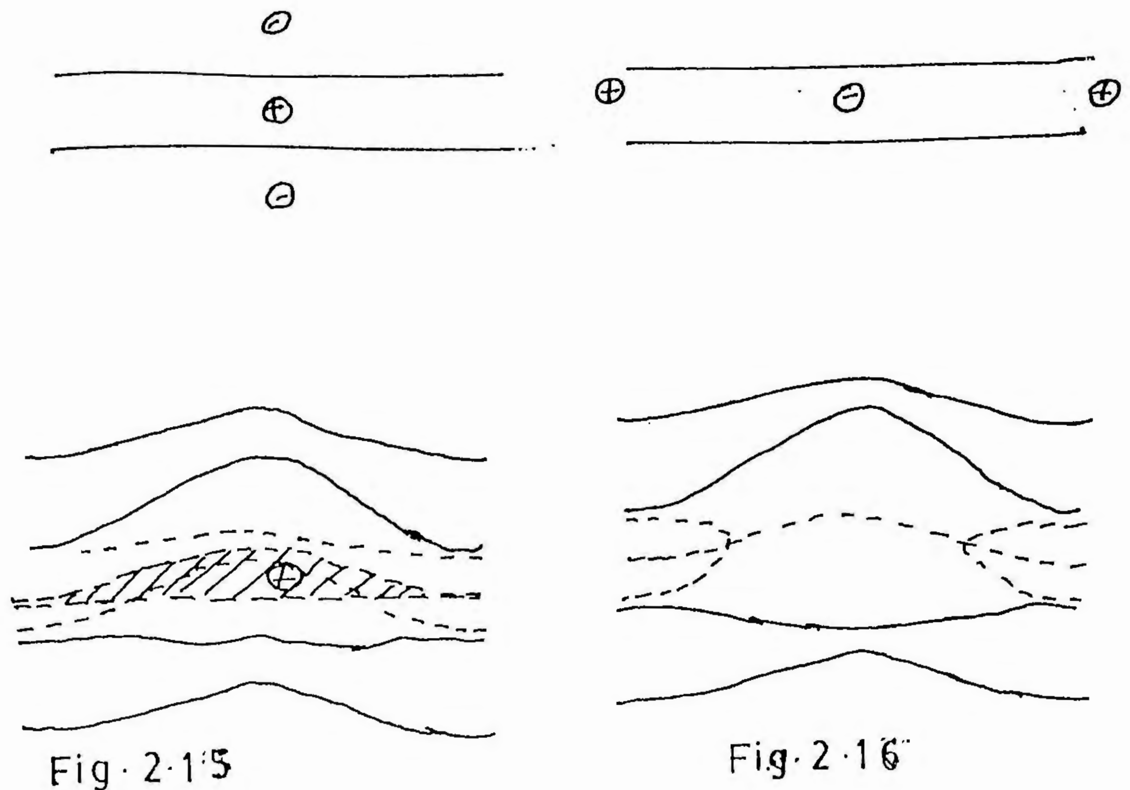

Fig.2.15 A possible non-conducting state of a filament resulting from negative charge trapped in the surrounding unformed material near a constriction (a) geometrical representation ; (b) the corresponding band diagram for the filament constriction.

Fig.2.16 A possible non-conducting state of a filament resulting from negative trapped charge in the localised levels of a constriction. This may give rise to a sufficiently large increase in V_o to locally eliminate the mobilily gap. The local polarisation field is shown as a hump in the whole band scheme (a) Geometrical representation (b) Corresponding band diagram for the filament.

this ratio rises above a critical value the mobility band will disappear as all the states in this region become localized. This situation is represented by Fig. 2.16. On increasing the bias potential difference further the electrons acquire sufficient energy to enter deep lying traps which are considered to have longer relaxation times. The negative space-charge region will induce positive space-charge within the filament as the ends of the constriction to preserve charge neutrality.

Electron emission is interpreted in the following manner. Many small weak spots exist on the anode. In some of these spots, the potential drop may be nearly equal to the whole bias voltage. As a result electrons from the constrictions lying in the vicinity of the anode will be accelerated to a high kinetic energy favorable for emission.

2.2.2.3 Rakhshani, Hogarth and Abidi Model.

This model is also filamentary in origin (9). If was put forward to explain certain experimental observations. In this model it is postulated that a high-field solid state electrolytic process takes place within the filaments. The potential drop across the formed devices is considered to be non-uniform with most of it being dropped across a relatively thin region. The effective electric field across this region is likely to be of the order of $10^{10} Vm^{-1}$, Fi. 2.17 illustrates this process.

In such a high field region electrolysis can occur in which an excess of O^{2-} ions drift towards the positive electrode and metal ions (positive ions) towards the negative electrode. The metal ions lead to an increased local congestion of material, as observed, but

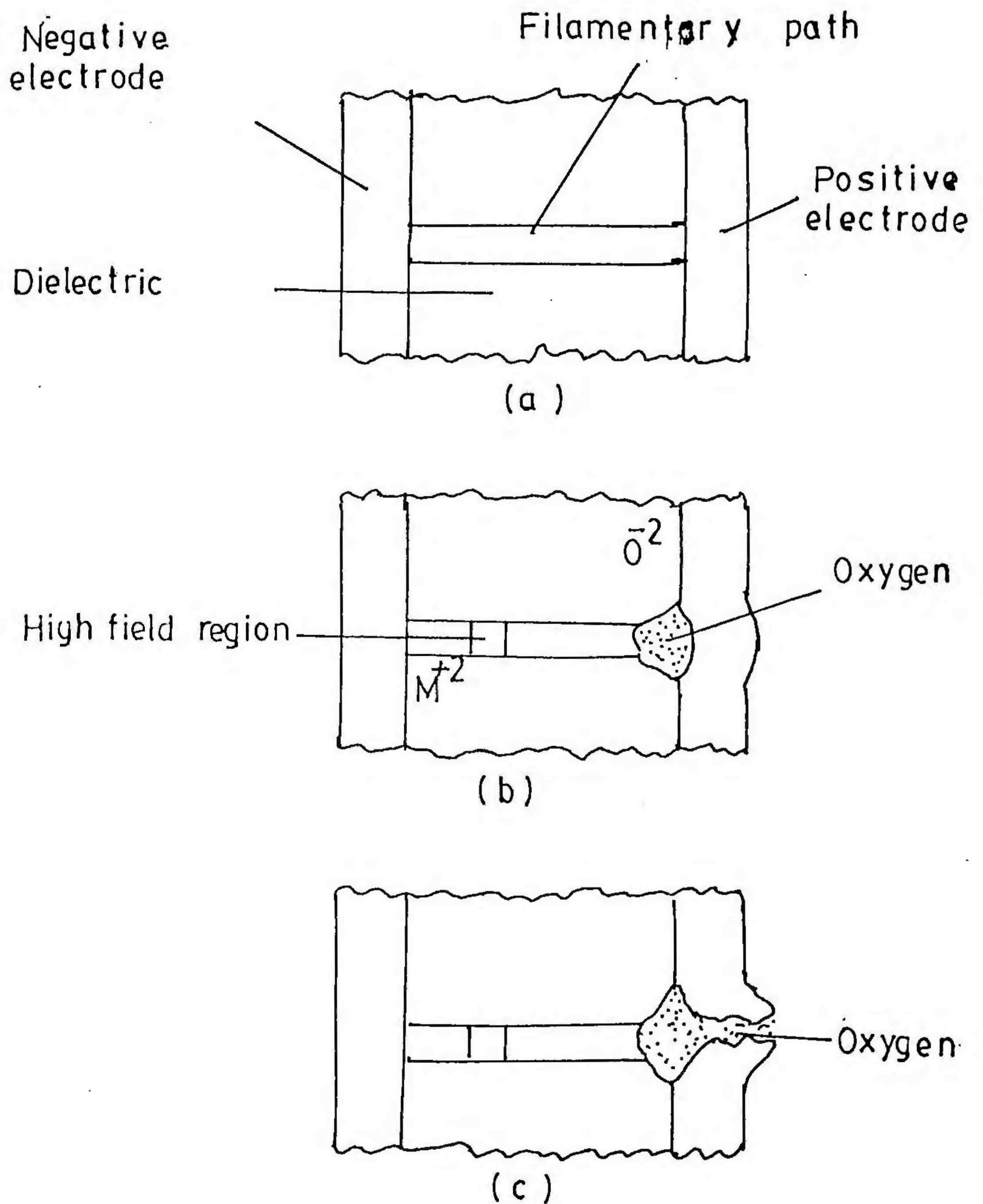

Fig.2.17 Geometry of a postulated grown filamentary path across the insulator of an MIM thin film device.

the oxygen ions will dissociate into oxygen gas and electrons. The increased oxygen pressure will cause electrode peeling and formation of holes, as has also been observed.

At low electric fields, Ohm's law is obeyed but as the applied potential difference is increased, negative space charge builds up near the anode until, at some stage, recombination takes place. This corresponds to the potential difference at which electroluminescence is observed. Electron emission may also occur but generally significant emission results when, with further increase in potential difference, a positive space charge is established near the cathode; diffusion of metal ions into the cathode causes the thickness of the insulating part of the filament to increase. This is the region of high electric field strength. The potential drop across this insulating region thereby increases and the magnitude of the circulating current decreases. This, then, explains VCNR in the I_s-V_s characteristics of the formed device.

With dielectrics of greater thickness a higher forming voltage is necessary. In addition there is also the possibility of dissociated positive ions being trapped by dangling bonds carrying unpaired electrons. Ion migration and the consequent electroforming are, therefore, diminished.

2.2.2.4 Sutherland Modification for the Filamentary Model.

Sutherland's modification of filamentary model accounts the current flowing through the MIM devices according to the following mathematical relation

$$I_s = k \sinh KV_s \quad \ldots \quad (2.73)$$

Where k, K are constants.

2.2.2.5 Our modification to the Filamentary Model.

The following two relation for currents have been used for fitting the complete I_s-V_s characteristic curves of different sizes of the electroformed MIM devices :-

$$I_s = I_o \exp\{(V_F - V_S)K'\} (\mathrm{Sin} \sqrt{KV_S})^9, \quad V_S \le V_F \quad \ldots\ldots \quad (2.74)$$

$$I_s = I_o \exp\{(V_S - V_F)K'\} (\mathrm{Sin} \sqrt{KV_S})^9, \quad V_S \ge V_F \quad \ldots\ldots \quad (2.75)$$

Where I_o ,K,K' are the fitting parameters, V_s and I_s are the sample voltage and current respectively and V_F is the forming voltage. The value of $K = 0.5\ V^{-1}$ was used for fitting all the curves of Fig. 4.13 and Fig. 4.16 of chapter IV.

CHAPTER III

EXPERIMENTAL EQUIPMENTS AND TECHNIQUES

3.1 Preparation of Samples In Vacuo.

Thin film specimens for all experimental investigations (electrical/optical/structural) were prepared in vacuo by using Edwards E306A coating plant having resistive heating and Edwards E306 coater with electron bean heating techniques. The main parts of the coating plants are shown schematically in Fig.3.1 The general layout of the plants E306A and E306 are shown in Fig.3.2 and Fig.3.3 respectively. Each of the coating plants consists of three principal parts:

1. the deposition chamber,
2. the pumping system and
3. the electrical sources.

In case of resistive heating technique, electrical sources are fixed with the coater while in the latter case electrical sources are fed by Edwards EBS power supply unit (model - D325).

Deposition chamber of the coater is covered with a domed type bellar. Evaporation sources with the evaporant chamber placed in the deposition are which is evacuated to the desired pressure level. After obtaining the desired vacuum, the sample is evaporated on the substrates held by the substrate holder. Metallic masks mainly aluminium (Al) sheets were used for device fabrication purposes. The masking system used for the fabrication of devices is shown in Fig. 3.4. and the complete metal-insulator-metal (MIM) sandwich structure is depicted in Fig.3.5. A mechanical shutter

1. Vacuum chamber, 2. Ionization gauge, 3. High vacuum isolation valve, 4. Liquid nitrogen trap, 5. Diffusion pump, 6. Roughing valve, 7. Backing valve, 8. Pirani gauge, 9. Rotary pump.

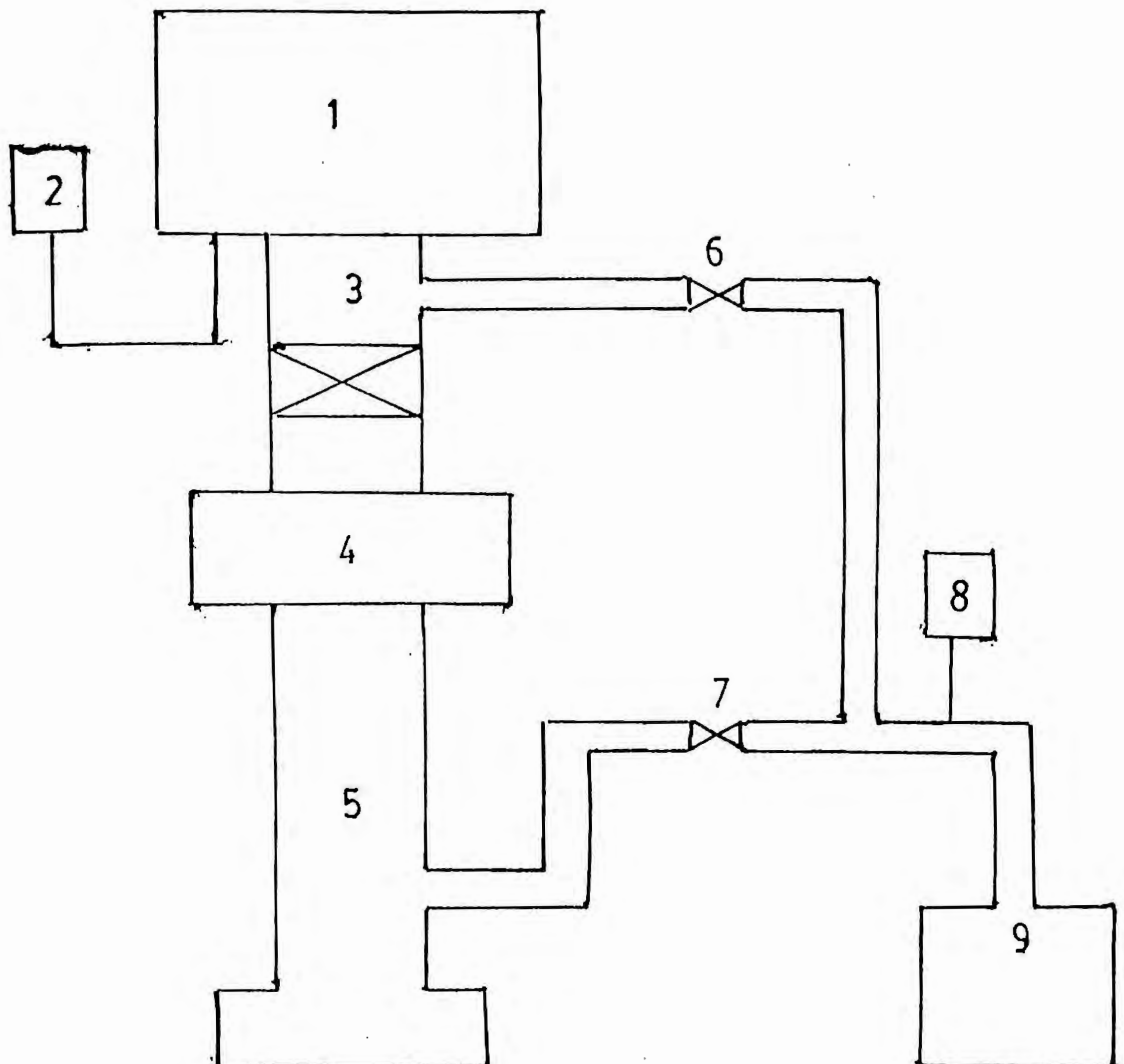

Fig.3.1 Schematic representation of a vacuum coating unit.

Fig.3.2 E306A thermal heating coating unit.

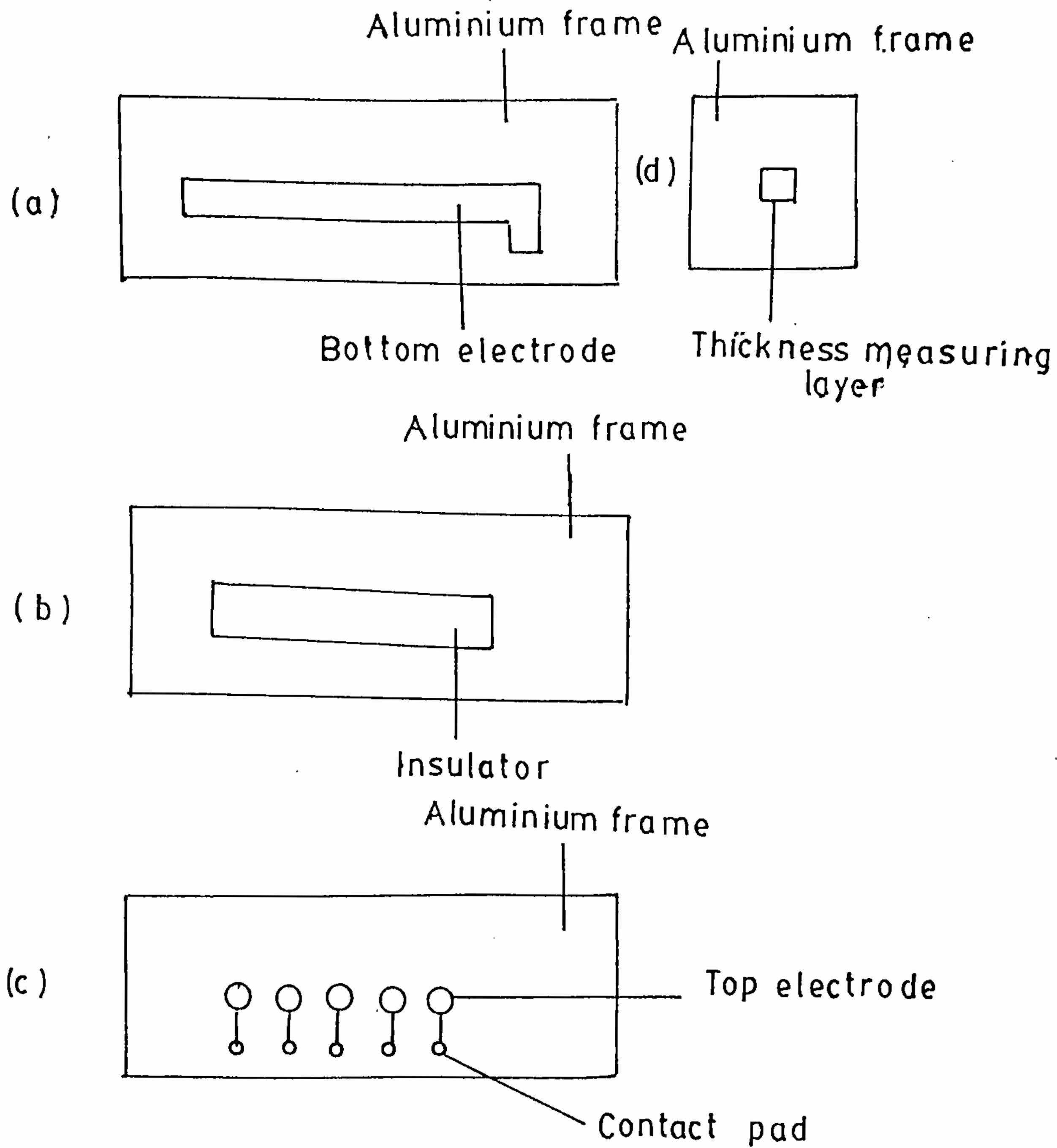

Fig.3.4 Aluminium masks of various sizes.

operated from outside was used for isolating the substrate from the evaporants at desired time.

The chamber is evacuated with a rotary-diffusion pumps group. Rotary pumps of E306A and E306 coaters are Edwards model E2B8 and ESZ00A respectively. The above mentioned series pumps comprise single and two stage direct drive, oil sealed outfits designed for a wide range of basic vacuum pumping duties. The diffusion pumps employed in E306A and E306 coaters are Edwards model E04K. The E04K series oil vapour diffusion pumps are fully fractiorating 3-stage units with final ejector stage. This pump is connected to the coating plant chamber via a high vacuum isolating valve which permits the diffusion pump to be kept evacuated at any time and in conjunction with a stainless-steel liquid nitrogen trap which prevents back streaming and back migration of oil vapour into the coating plant thereby reducing the chances of any oil contamination. Foreline traps fitted with activated alumina (Al_2O_3) are used to minimize the contamination of the system resulting from oil vapour released from rotatory pump oil during normal operation. The pressure in the vacuum system was monitored with a pirani guage (Edwards model PR10K) and a penning gauge (Edwards model Penning 8,07-D043-14-000). Pirani and Penning guages associated with the coaters are capable of recording pressure in the ranges $5-10^{-3}$ and $10^{-2}-10^{-7}$ torr respectively.

3.2 Boats and Filaments.

Boats and helices used for the evaporation of sample materials (Cu, Al, SiO, V_2O_5) are shown in Fig. 3.6. Boat material was

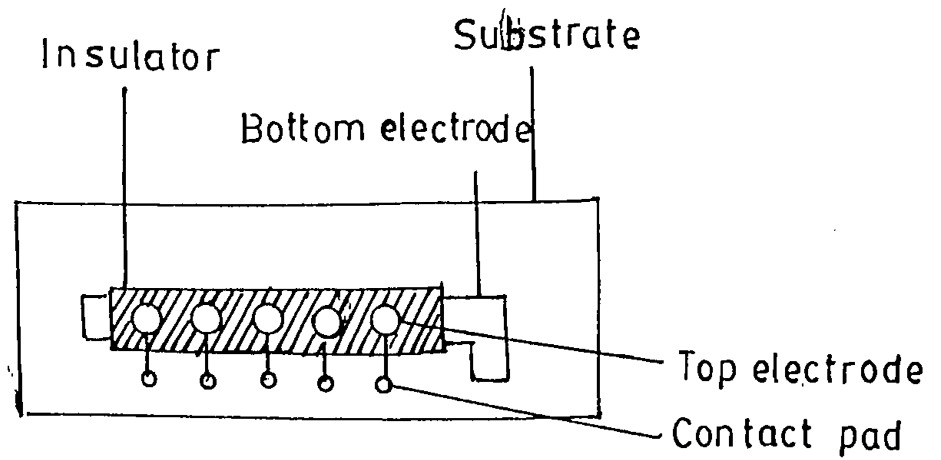

Fig.3.5 Sandwich structure.

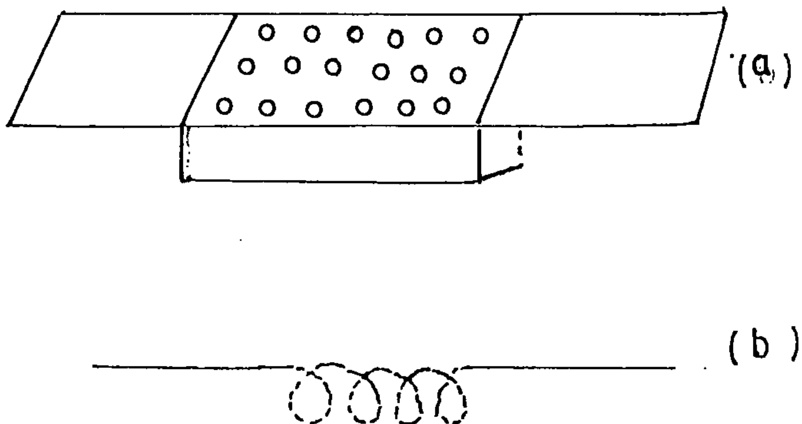

Fig.3.6 (a) Molybdenum boat (b) Tungsten helix.

molybdenum foil and helix material was tungsten wire. Molybdenum boats were used for the evaporation of Cu, SiO and V_2O_5 and tungsten helix was used for Al deposition purposes.

3.3 Electron Beam Source.

Fig. 3.7 shows the filament made of tungsten wire used as a source of electron in the EBS sources. Accelerating voltage and filament current ranges are respectively 0-6 KeV and 0-500 mA. Fig.3.8 shows the source of electrons and the accelerating voltage of electrons. Tungsten filament emits electrons when it is heated by supply AC current. These electrons are accelerated towards the cermet support (which is called hearth) by applying accelerating voltage between filament and cermet support. By raising the cermet support by a spacer, the electron beam can be focussed on the cermet containing sample material for evaporation.

3.4 Substrate Cleaning Procedure.

The substrate cleaning is very important in thin film technology. The following technique was adopted for cleaning the substrate in the present work: Corning glass substrate were cleaned firstly with boiled soda water and dried. After this they were dipped into a solution of distilled water containing 40% nitric acid. The substrate were them transferred to a container having a chromic acid solution. Just before fabricating the sample, the substrate was taken out of the solution and washed with distilled water. It was finally cleaned with acetone and dried with hot air blower and placed in the deposition chamber.

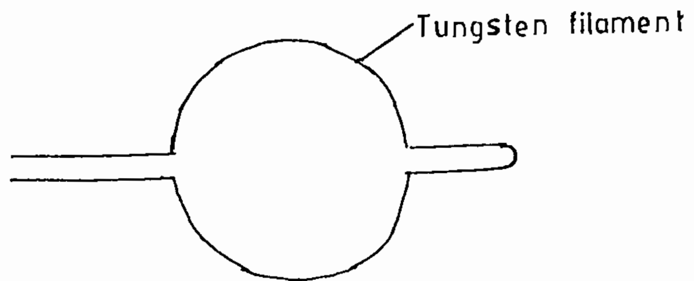

Fig.3.7 Tungsten filament.

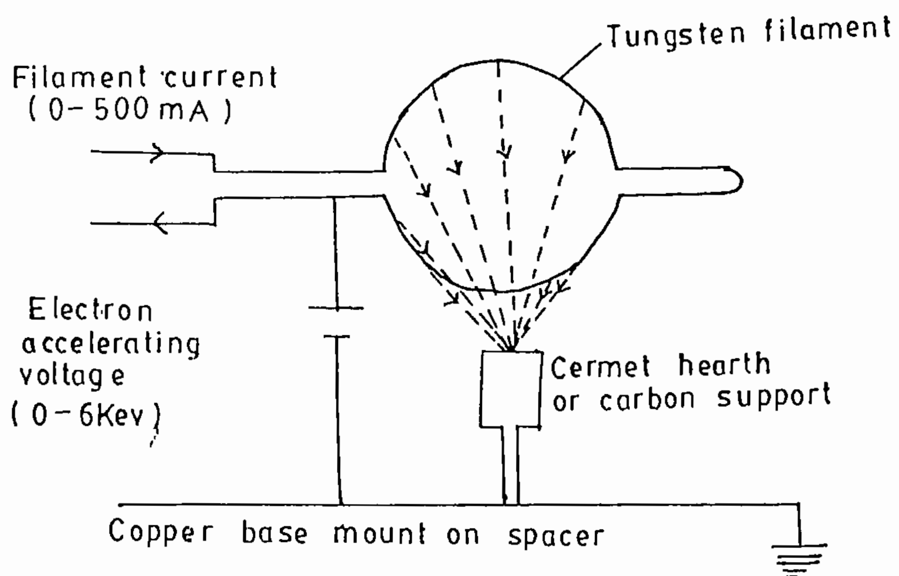

Fig.3.8 Source of electrons.

3.5 Deposition Parameters.

The parameters which have strong influence on the electrical conductivity of the thin film devices are the film-thickness, deposition rate and the residual pressure. The substrate was held at room temperature (~ 28°C). In the present study, the electrode thickness was maintained at nearly 3000 Å for Al and 24000 Å for Cu. The insulator (SiO) thickness was in the range Prior to the device fabrication, the chamber was well cleaned to avoid any contamination affecting the fabricating device.

3.6 Sample Fabrication.

The device materials were SiO powder (Aldrich Chemical Company, Inc., USA), V_2O_5 powder (Matheson Coleman and Bell, USA), Aluminium and Copper of 99.9% purity (Koch-Light Laboratories Ltd.). The chamber was loaded with clean substrate and evaporating sources. When the chamber pressure is about 10^{-5} torr. evaporation of sample had begun. The steps adopted in the fabrication of MIM sandwich structures were as follows: Firstly device fabrication procedure by resistive heating technique is described. Keeping shutter in place, the LT supply was increased slowly in order to outgas the filament. The shutter was removed when the residual pressure was reached 10^{-5} torr and the bottom aluminium electrode was deposited. After an interval when the pressure was again stabilized at 10^{-5} torr, SiO/V_2O_5 (as desired) was deposited. Finally the top electrode was deposited. In this way fabrication of MIM devices was completed. In the same run samples for optical and structural studies were prepared using different masking system.

the same manner using EBS source device were fabricated.

3.7 Sample Thickness Measurement

The thickness of a film is a very important parameter and hence its measurements are of great importance in thin film investigation. The sample thickness was measured using multiple beam interferometric technique. The fringe pattern observed in the interferometer is shown in Fig.3.9. The thickness 'd' of the specimen is related to wavelength (λ) by the formula:

$$d = (S/D_ \times (\lambda/2) \quad \ldots\ldots\ldots\ldots\ldots\ldots \quad (3.1)$$

where λ is the wavelength of sodium light employed to illuminate the film surface. The distances S and D are the step height and interfringe separation respectively as shown in the diagram (Fig.3.9).

3.8 Electrical Measurement Systems.

All the electrical measurements were carried out inside a vacuum system at normal as well as under reduced pressure and in the temperature range 300-600 K. The electrical measurements were classified into two divisions DC measurements and AC measurements.

3.8.1 DC Measurement.

The unformed, preformed and switching behaviour of the samples were investigated using the circuitry depicted in Fig. 3.10.

The formed and electron emission characteristic of the devices were investigated employing the circuitry depicted in Fig. 3.11.

3.8.2 AC Measurement.

AC measurements were carreid out by employing AC Wayne Kerr bridge (4250).

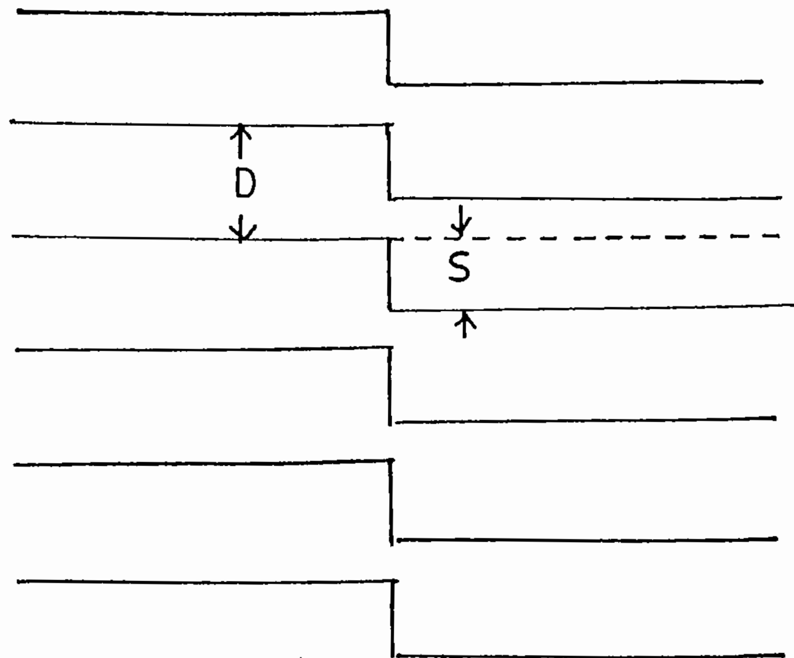

Fig.3.9 Typical interference fringe pattern.

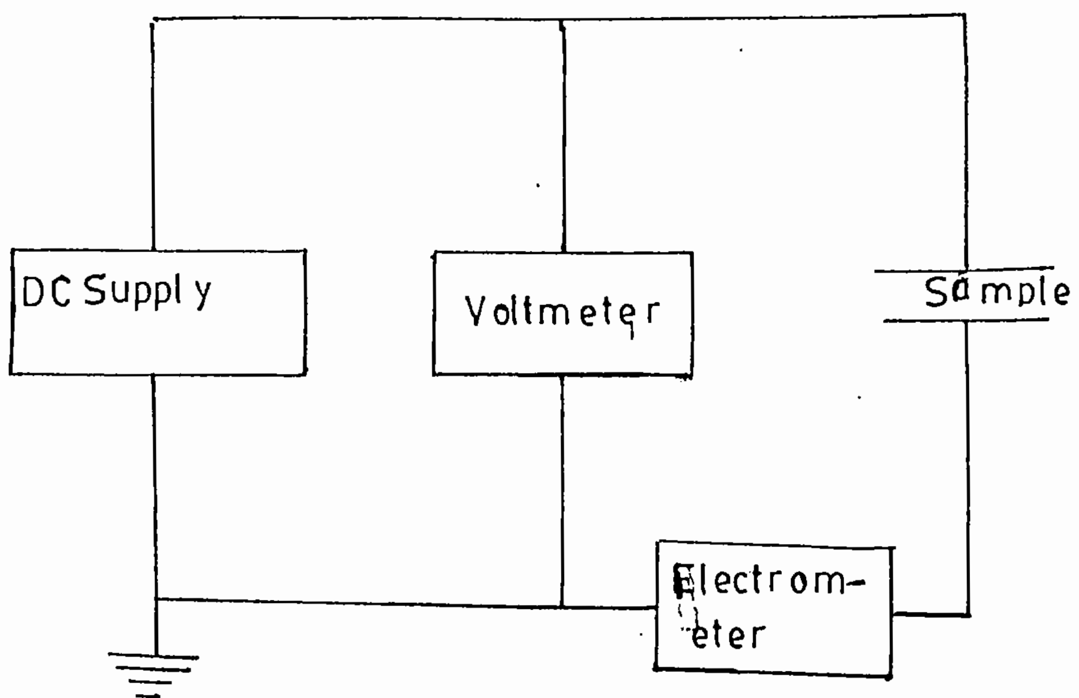

Fig.3.10 DC V-I measuring circuit.

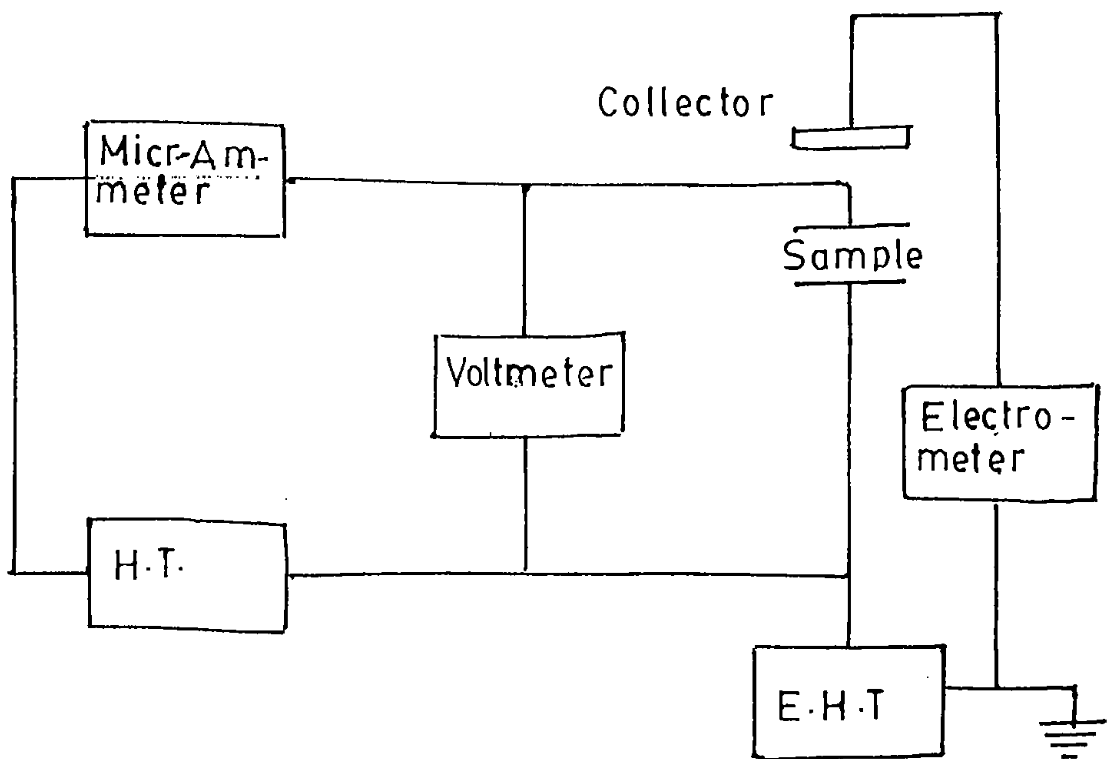

Fig.3.11 Electron emission measuring circuit.

3.9 Optical Measurements.

For studying optical properties in the visible range of the optical spectra, SiO and V_2O_5 films were deposited on well cleaned corning glass substrate as discussed in section 3.6. The specimens were investigated using Shimadzu UV-180 double beam spectrophotometer. For IR investigation SiO and V_2O_5 films were deposited on monocrystalline silicon watfer (n-type, (100)). These specimens were studied using Pye Unicam SP3-300 infrared spectrophotometer.

3.10 Structural Study.

The structural studies of SiO and V_2O_5 films were made using a X-ray diffractometer (model JDX-8P, JEOL, JAPAN). The samples for these studies were deposited on microscope slides.

CHAPTER IV

EXPERIMENTAL RESULTS AND DISCUSSIONS

In this chapter the experimental results of electrical, optical and structural measurements and their detailed analyses have been presented.

4.1 Electrical Measurements:

The MIM devices for electrical measurements were of two categories: (1) unformed and pre-formed devices (2) Electroformed devices.

Firstly, experimental results and analyses of unformed and pre-formed devices are described below:

4.1.1 DC Measurements.

Current-Voltage (I_s-V_s) characteristics of unformed Al-SiO-Al and pre-formed Al-SiO-Cu sandwich devices for different SiO film thicknesses are shown in Figs. 4.1(a) and 4.1(b) respectively.The above measurements were carried out at normal temperature and pressure. It is also found that under vacuum the Al-SiO-Al devices displayed unformed characteristics. The Al-SiO-Cu devices were found to show preformed characteristics under pressure > 10^{-2} torr. It is seen from these graphs that the lower the insulator thickness higher the current flowing through the devices.

In Figs. 4.1(c) and 4.1(d) the effect of temperatures on the I_s-V_s characteristics of unformed and pre-formed devices are exhibited. It is observed from the graphs that higher the temperature higher the current flowing through the devices.

It is evident from the I_s-V_s graphs of Figs. 4.1(a) -4.1(d) that the electrical conduction is non-ohmic under the electric field > 10^6V^{-1}. This non-ohmic behavior of MIM unformed and preformed devices under high field conditions may be explained normally by employing one of the following models.

1. electron tunnelling;
2. space-charge limited current (SCLC) conduction;
3. Schottky emission and
4. Poole-Frenkel emission.

It is the purpose to find out the suitable high field conduction model for the present unformed and pre-formed MIM devices.

Electron Tunnelling.

Electron tunnelling mechanism is inapplicable in the present case because of the SiO film thickness (>> 100 Å) and strongly temperature dependent conductivity observed in the devices.

Space-Charge-Limited-Current (SCLC) Conductivity.

Secondly, SCLC conduction model is employed to test the high field experimental results. Each of the graphs of Figs. 4.1(a)-4.1(d) were examined by the SCLC relation $I_s=aV_s^n$. The values of the exponent in the I_s-V_s were found to be 2.

Fig. 4.2(a) shows the variation of current with SiO film thickness for Iv, 8V, 16V applied bias. The experimental data were tested using the relation $I_s \propto d^{-n}$. The maximum value of the exponent was found to be 3. Therefore, the combination of these two results support Mott-Gurney SCLC model ($I_s \propto V_s^2 / d^3$).

For a surer test of M-G SCLC model a further test is carried out showing the variation of I_s/d with V_s/d^2 for the IV, 4V, 8V applied bias (Fig. 4.2(b)). Each of the curves follows the relation I_s/d = constant $(V_s/d^2)^n$. The estimated value of the exponent was found to be 2. This test confirms the Mott-Gurney SCLC model. It is seen from Figs. 4.1.(d) that the device current increases with temperature. Temperature dependent I_s-V_s characteristics are generally explained using the concept of traps. Trap filled model has been employed in the present devices. It is seen apparently that trap filled SCLC model is in good agreement with the experimental results.

Arya and Singh ( ) carried out measurements in NB_2O_3, Ti_2O_3, Bi_2O_3 and SiO_2, chari and Mathur (1981) in Al_2O_3, Wiktorczyk and wesolowska (1982) in Yb_2O_3, Gould (1983) in Nd_2O_3, Dharmadhikari (1983) in Nd_2O_3, Efendiev *et al.* (1989) in Bi_2O_3, Gould and Ismail (1990) in Cd Te. All of them explained their high field results in terms of trap filled SCLC model.

Schottky and Poole-Frenkel Emission.

Although it is found that apparently SCLC model does fit our high field experimental results of MIM devices, it is our interest to find out an exact model for MIM devices.

Schottky model is invoked for explaining our high field DC results. Fig. 4.3(a) is a typical I_s-V_s characteristics which shows the variations of log I_s with E^{12}_s for an unformed Al-SiO-Al sandwich device with insulator thickness 1600 Å and Fig. 4.3(b) shows that for a pre-formed Al-SiO-Cu sandwich device having insulator thickness 2000 Å for different temperature. The curves of Figs. 4.3

(a) and 4.3 (b) are linear in the field region $\leq 4 \times 10^7$ vm^{-1}. This linearity reveals that the conduction mechanism may be due to schottky emission or due to the Poole-Ferenkel emission. The I_s-V characteristics of Figs. 4.3(a) and 4.3(b) may be redrawn in terms of Schottky or Poole-Frenkel ($I_s = I_o$ exp $(e\beta E_s^{1/2}/KT)$) where $\beta = (e/\pi\eta\epsilon\epsilon_o)^{1/2}$. Theoretical values of $\beta_{sch.}$ and β_{PF} are 1.90×10^{-5} and 3.6×10^{-5} respectively. The experimental values of $\beta_{exp.}$ were calculated from the slopes of curves of Figs. 4.3(a) and 4.3(b). Values of the dielectric constant ϵ were calculated from the experimental values of $\beta_{exp.}$ for Schottky and Poole-Frenkel emission cases $(\beta_{PF}) = (e\pi\epsilon\epsilon_o)^{1/2}$. The values of β_{exp} and dielectric constants are listed in the following tables:

Table 1: Measured Schottky and Poole-Frenkel Parameters at different temperatures for an unformed Al-SiO-Al device.

Temperature (K)	Experimental Values of $\beta_{exp.}$ (10^{-5})	Dielectric constant (n=4, Schottky) estimated	Dielectric constant (n=1, Poole-Frenkel) estimated)
300	0.97	15.30	60.10
50	1.29	8.70	34.30
425	2.16	3.30	12.30
475	2.53	2.30	8.90

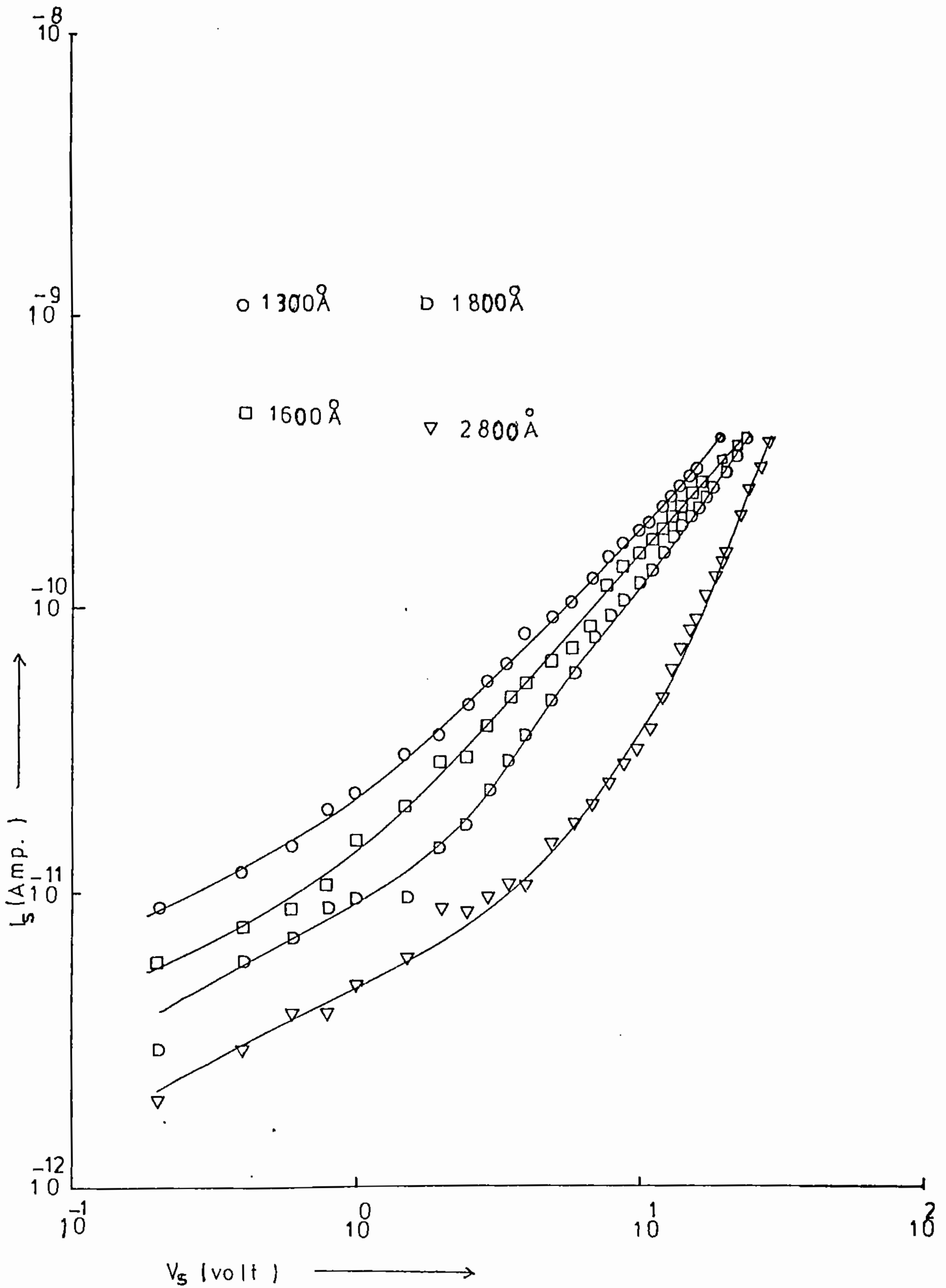

Fig.4.1(a) I_s-V_s characteristics of unformed Al-SiO-Al devices.

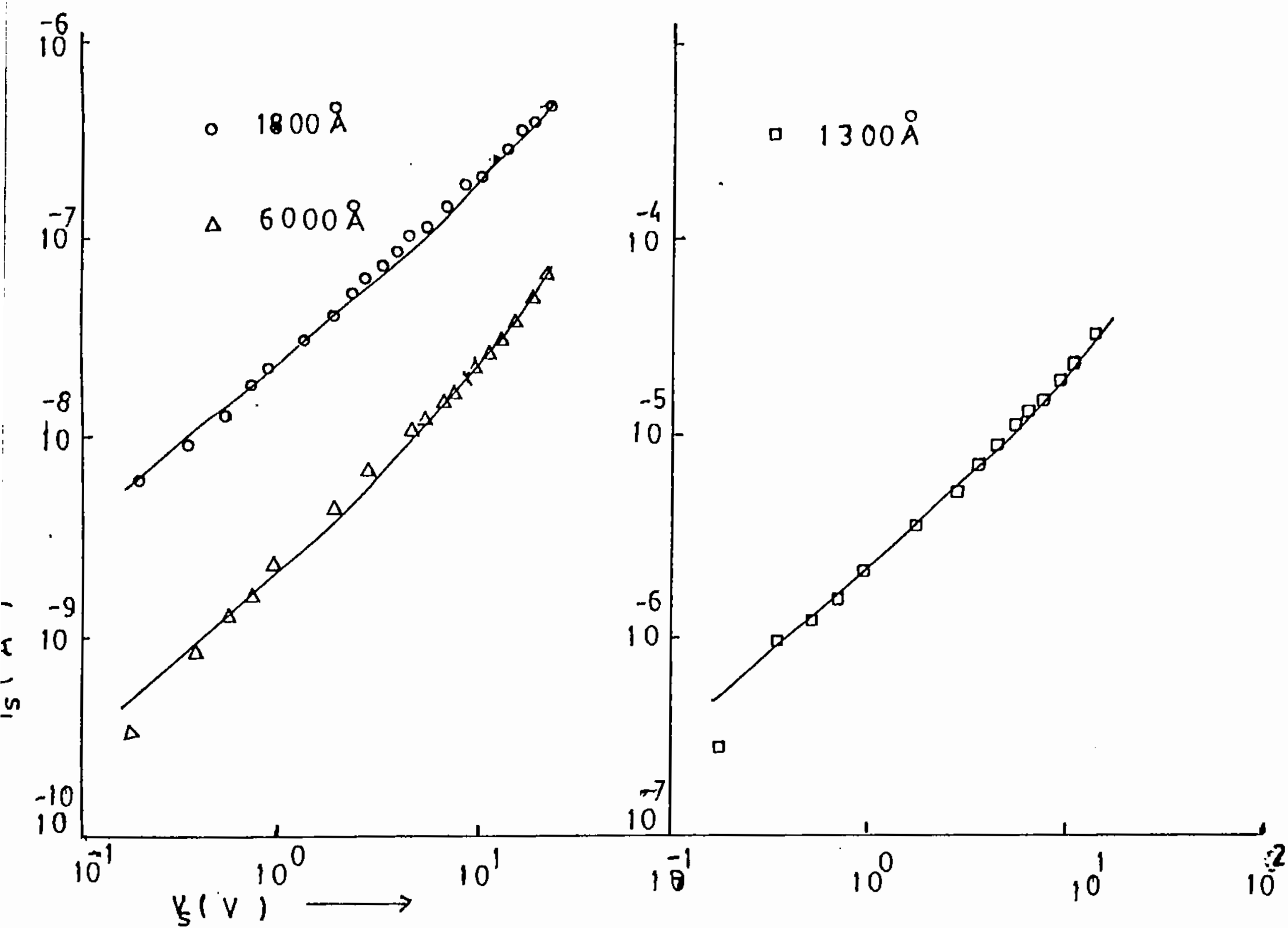

Fig.4.1(b) I_s-V_s characteristics of pre-formed Al-SiO-Cu devices.

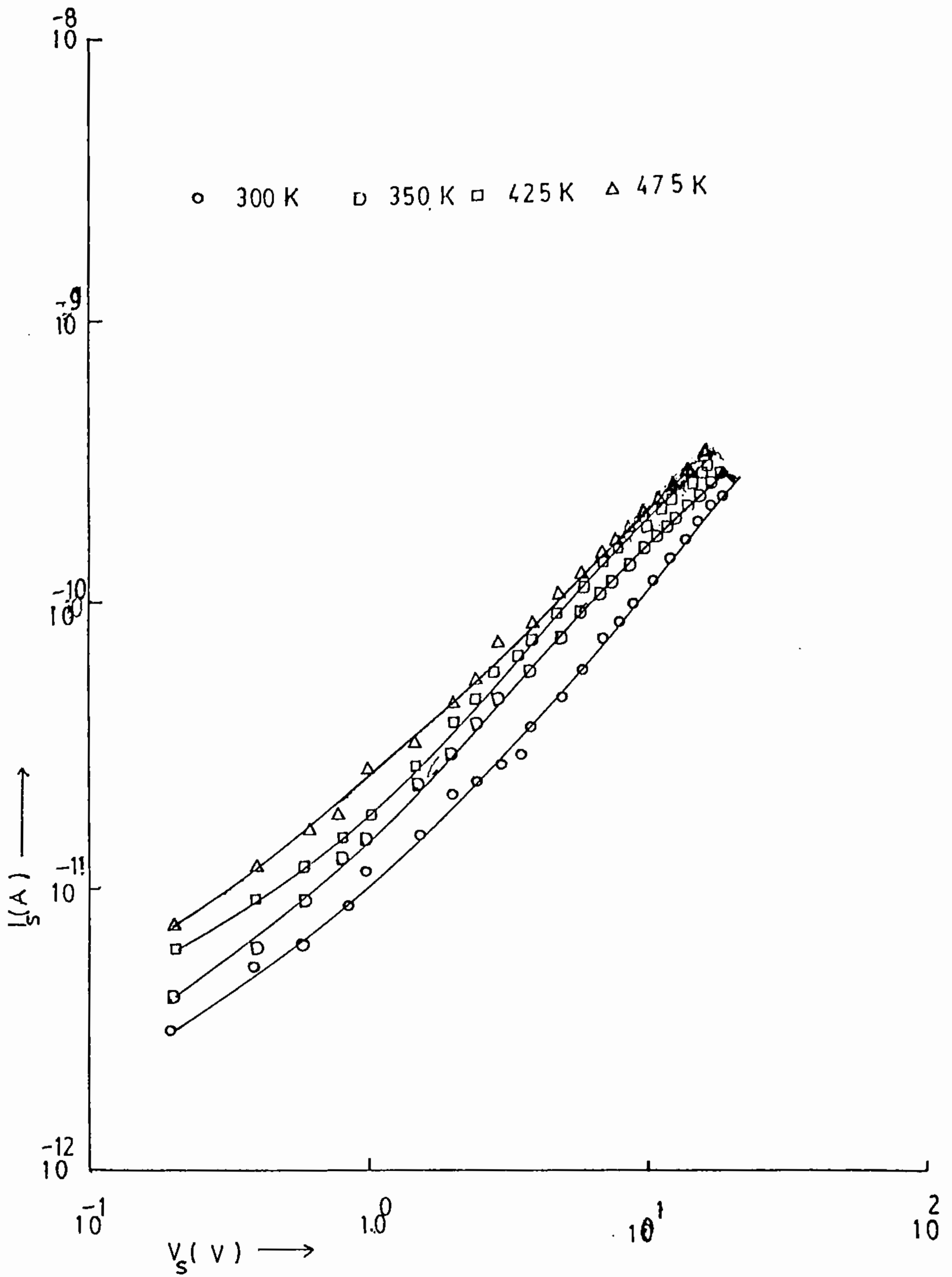

Fig.4.1(c) I_s-V_s characteristics of an unformed Al-SiO-Al device at different temperatures.

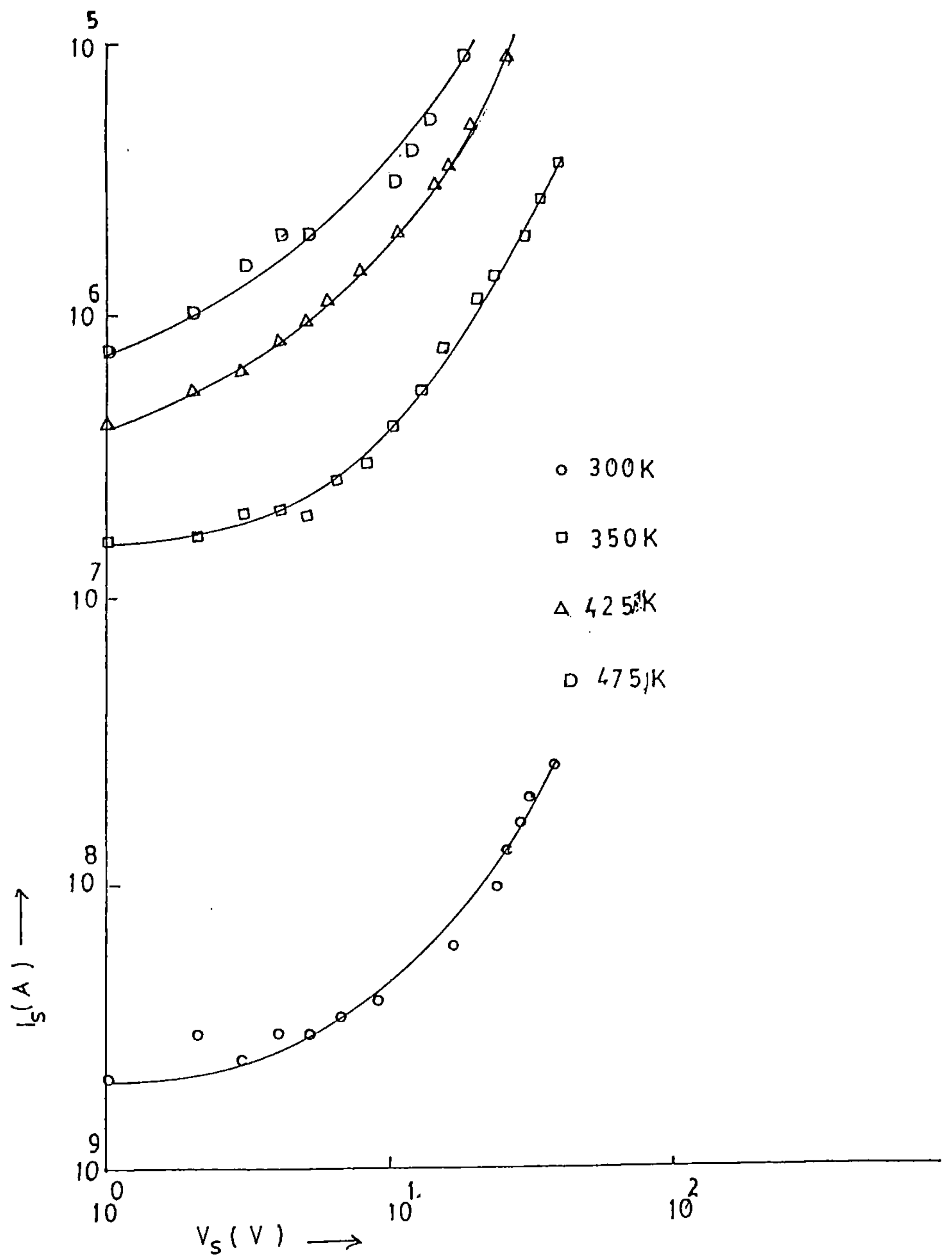

Fig.4.1(d) : I_s-V_s characteristics of a pre-formed Al-SiO-Cu device.

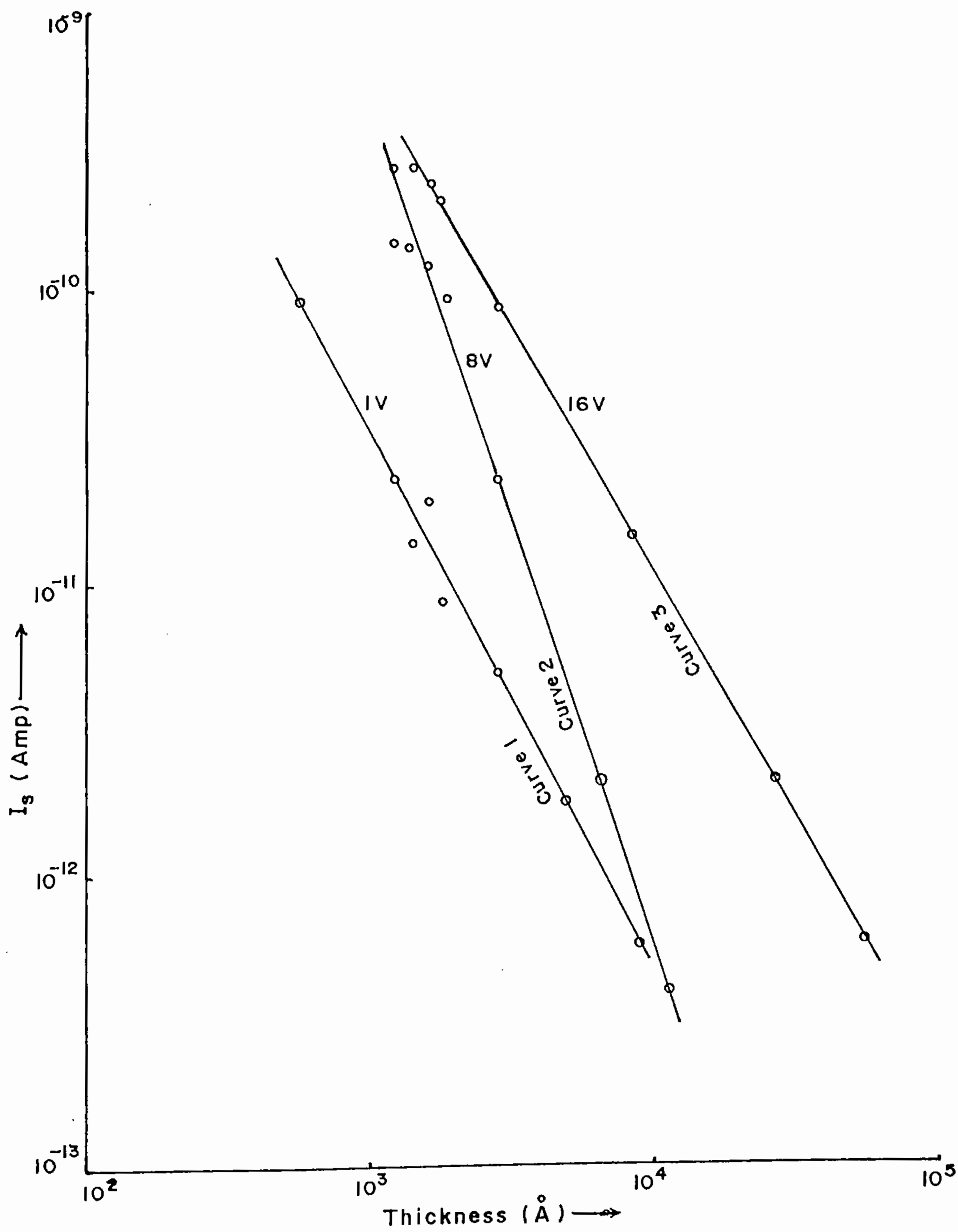

Fig.4.2(a) Current VS thickness curves of unformed Al-SiO-Al devices at different voltages.

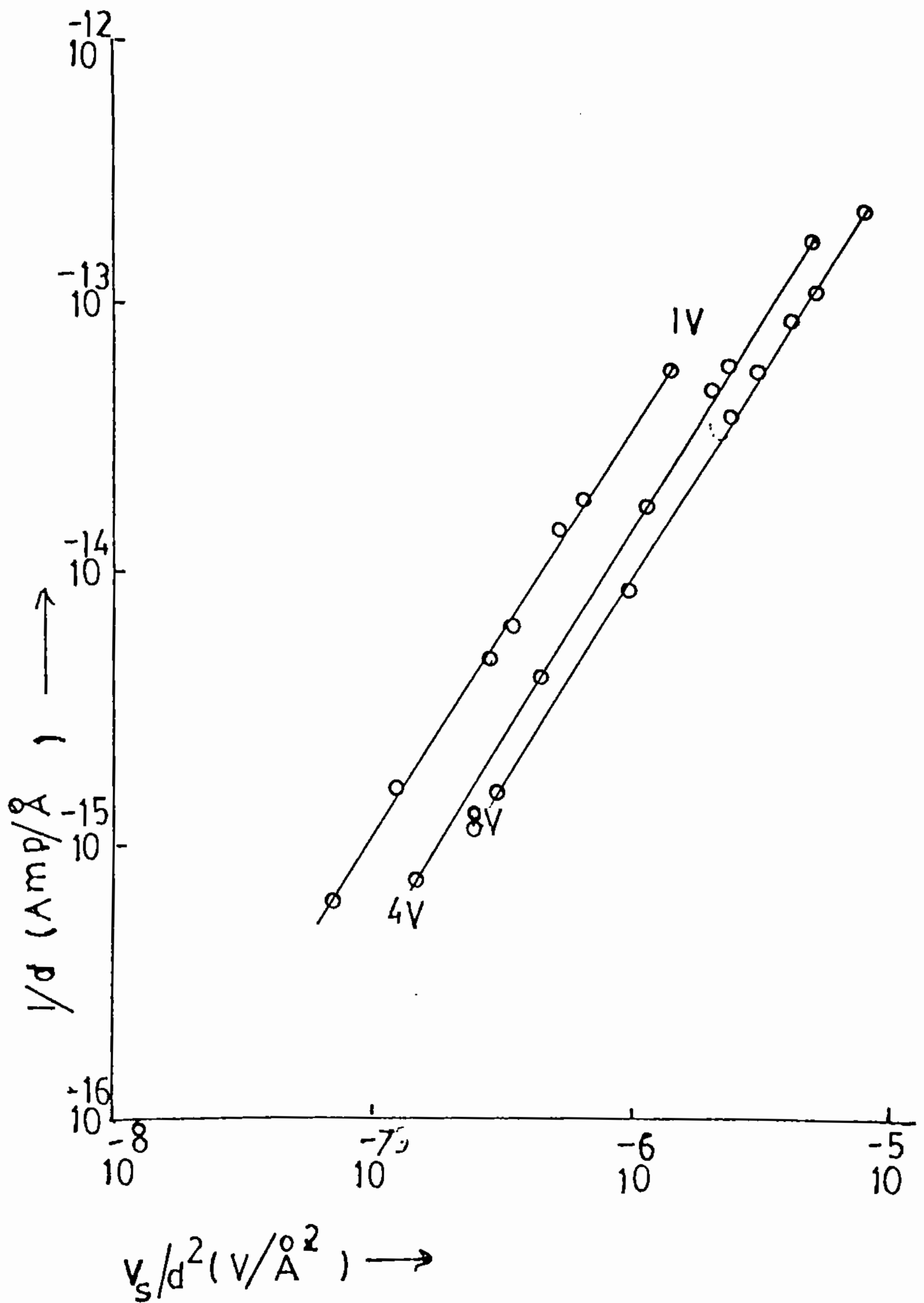

Fig.4.2(b) I/d versus V_s/d^2 curves of unformed devices.

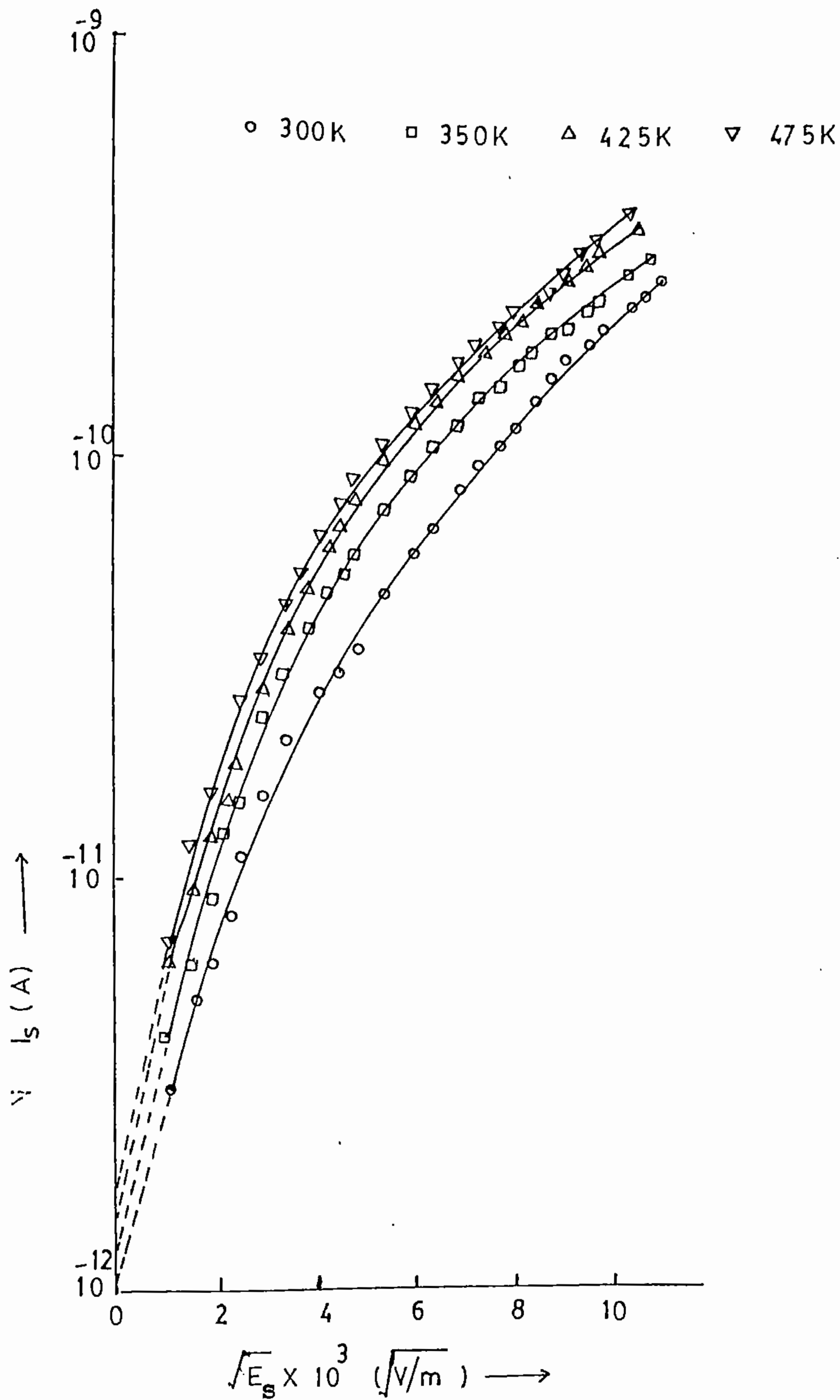

Fig.4.3(a) $I_s \sim E_s^{1/2}$ curves of an unformed Al-SiO-Al device at different temperatures.

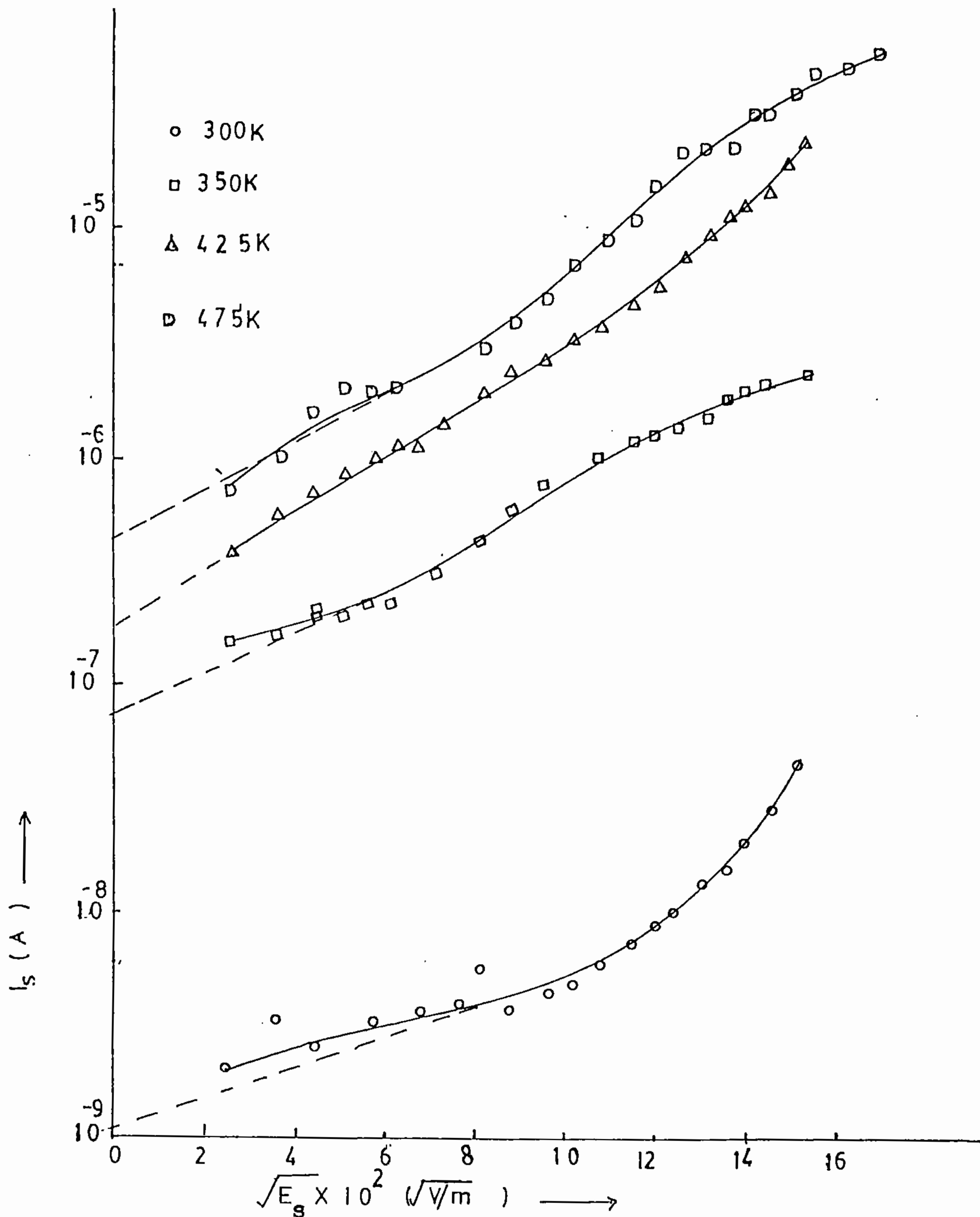

Fig.4.3(b) I_s-$E_s^{1/2}$ curves of a pre-formed Al-SiO-Cu device with insulator thickness 2000Å at four different temperatures.

Table 2: Measured Schottky and Poole-Frenkel parameters at different temperatures for a pre-formed Al-SiO-Cu Sandwich device.

Temperature (K)	Experimental Values of $\beta_{exp.}$ (10^{-5})	Dielectric constant (η=4, Schottky) estimated	Dielectric constant (η=1, Poole-Frenkel) estimated)
300	1.57	5.90	23.20
50	3.75	1.02	4.10
425	5.35	0.50	2.00
475	6.93	0.30	1.20

From tables 1 and 2 we see that some experimental values of β_{exp}. are in close agreement with the theoretical values of β_{sc} Suggesting that the electrical conduction is governed by Schottky emission mechanism.

The values of the dielectric constant ϵ found from the capacitance measurements of Al-SiO-Al/Al-SiO-Cu in the frequency range 10^2-10^5 Hzs lie in the range 1.30-4.30 and the values of the dielectric constant ϵ estimated from the optical measurements lie in the range 4.20-6.00. The values of the dielectric constant ϵ found from Schottky model lie in the range 2.30-5.90. It is observed that the values of dielectric constant obtained from different measurements have some agreement favoring schottky emission.

But the activation energy estimated from Figs. 4.4(a) and 4.4(b) for unformed device is found to lie in the range 0.12-0.20 eV and for pre-formed devices, the activation energy is 0.1 eV only. But for schottky emission, the activation energy should be 0.85 eV. so it is evident that schottky emission is not possible in the present devices.

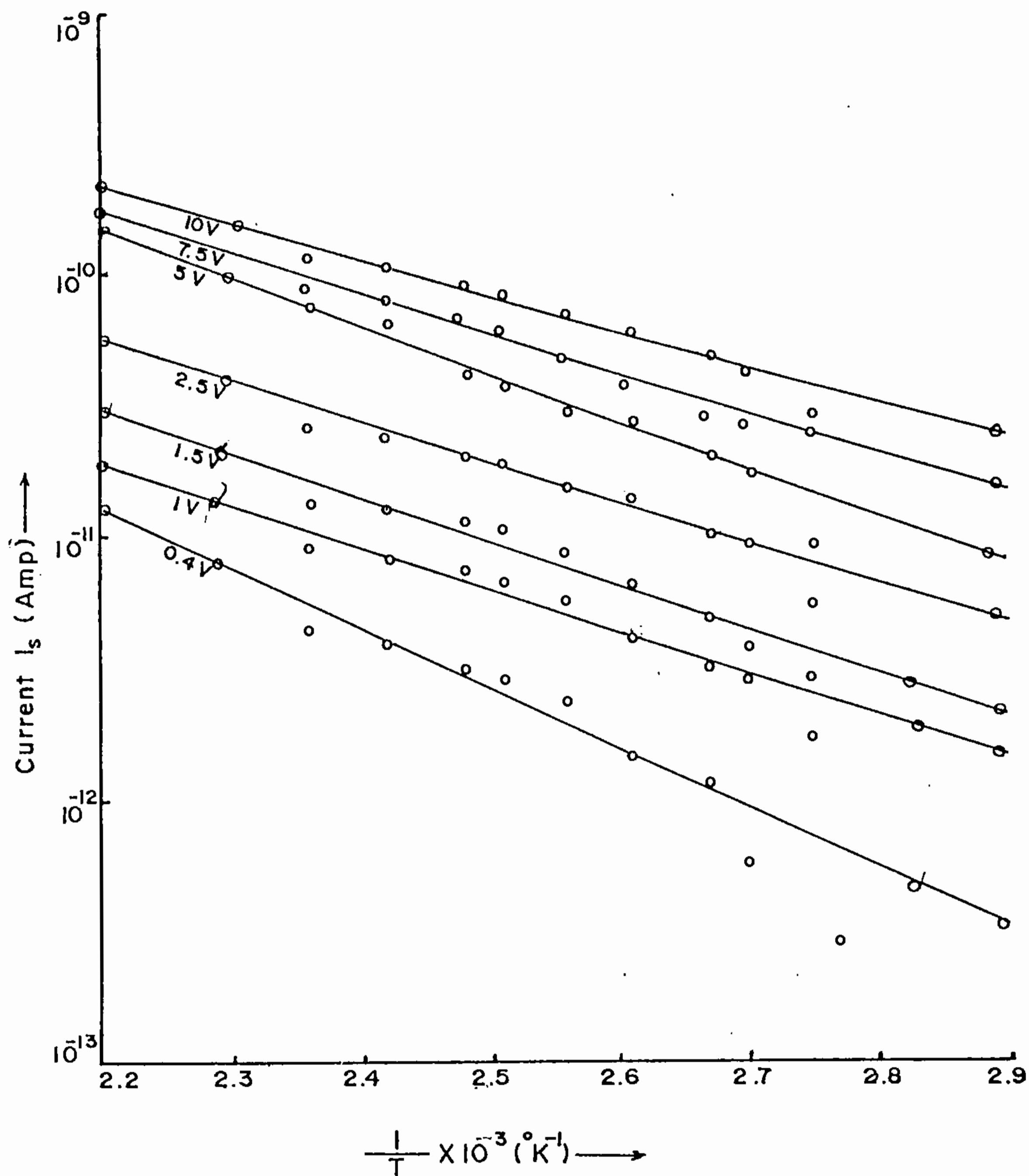

Fig.4.4(a) I_s-T^{-1} curves of an unformed Al-SiO-Al device at different applied voltages (1600Å).

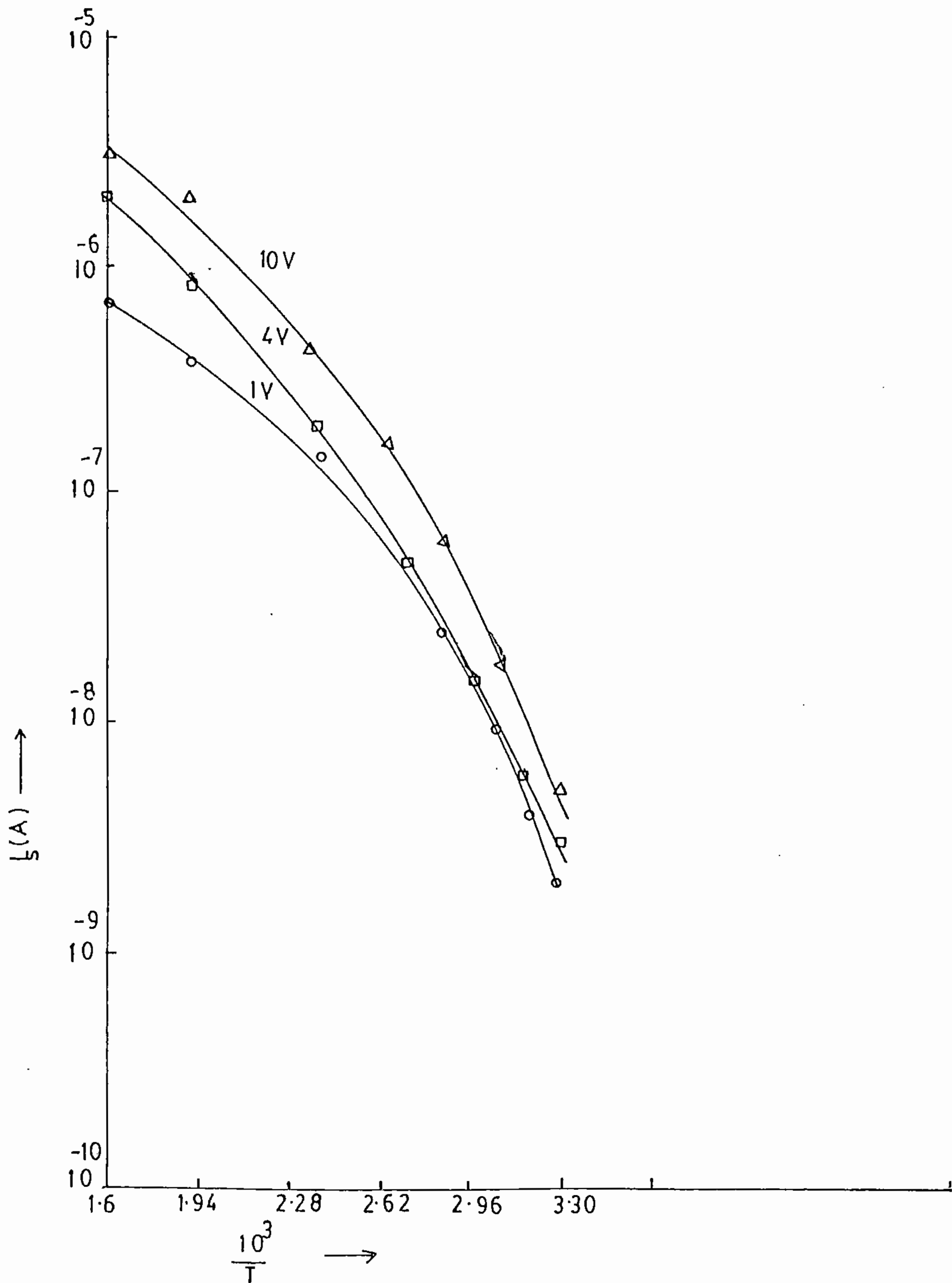

Fig.4.4(b) $I_s - T^{-1}$ curves of a pre-formed Al-SiO-Cu device with insulator thickness 2000Å at different applied voltages.

Furthermore, the device current haa pronounad thickness dependency, Hence the conduction mechanism cannot be schottky emission. Therefore there is possibility of operating Poole-Frunkel emission mechanisim.

Table 3. Estimated Activation Energy from experimental data for unformed Al-SiO-Al device.

Applied voltage in volts	Thermal activation energy, E_{th} (eV)	
	300-400K	400-455K
0.4	0.19	0.19
1.0	0.14	0.14
1.5	0.14	0.15
2.5	0.13	0.14
5.0	0.16	0.15
7.5	0.13	0.13
10.0	0.12	0.12

Table 4. Estimated Activation Energy from experimental data for pre-formed Al-SiO-Cu device.

Applied voltage in volts	Thermal activation energy, E_{th} (eV)	
	300-440K	440-625K
1	0.09	0.10
4	0.10	0.11
10	0.11	0.11

Poole-Frenkel Emission

In the previous section $\log I_s$ versus $E_s^{1/2}$ graphs are discussed (Figs. 4.3(a) and 4.3(b) which were common to both Schottky and Poole-Frenkel emission models. For confirmation of Poole-Fernkel model $\log(I_s/T^2)$ versus T^{-1} graphs for unformed and pre-formed

devices are drawn. These graphs are depicted in the Figs. 4.5(a) and 4.5(b) respectively. It is seen from the above figures that all the curves are non-linear. The non-linearity of these curves confirms the Poole-Frenkel conduction mechanism operating in the present case.

From tables 3 and 4 we see that the thermal activation energy of SiO film was fond in the range 0.09-0.19 eV.

Ignoring the anomalous values of ϵ obtained from different measurements (Dc, AC and optical measurements) and taking into account of log I_s versus $E_s^{1/2}$, Log (I_s/T^2) versus T^{-1}, ß (from DC measurements) and activation energy (0.1-0.2 ev) it is seen that the conduction mechanism operating in the unformed Al-SiO-Al and preformed Al-SiO-Cu devices are of Poole-Frenkel type.

For further confirmation of Poole-Frenkel model operating in the present devices Hill's generalized model (I_sT^{-3} exp Ei/KT) $E_s^{1/2}$ T^{-1}) has been employed using three different activation energies 0.12eV, 0.16eV, 0.19eV for the unformed Al-SiO-Al and 0.09eV, 0.10eV, 0.,11eV for the pre-formed Al-SiO-Cu sandwich device. The best fits for the unformed/pre-formed MIM devices were obtained for the energies 0.12eV, 0.09eV respectively. Figs. 4.6(a_1, a_2, a_3) indicate plots for Hill's generalized model for the unformed and Figs. 4.6(b_1, b_2, b_3,) indicate plots for the same model for the pre-formed MIM devices respectively. From the graphs of Figs. 4.6(a_1) and 4.6(b_1) . Value of $ß_{PF}$ were estimated which show an excellent agreement with the Poole-Frenkel model. The above graphs are shown in Fig.4.6(a_1-a_3) and 4.6(b_1-b_3).

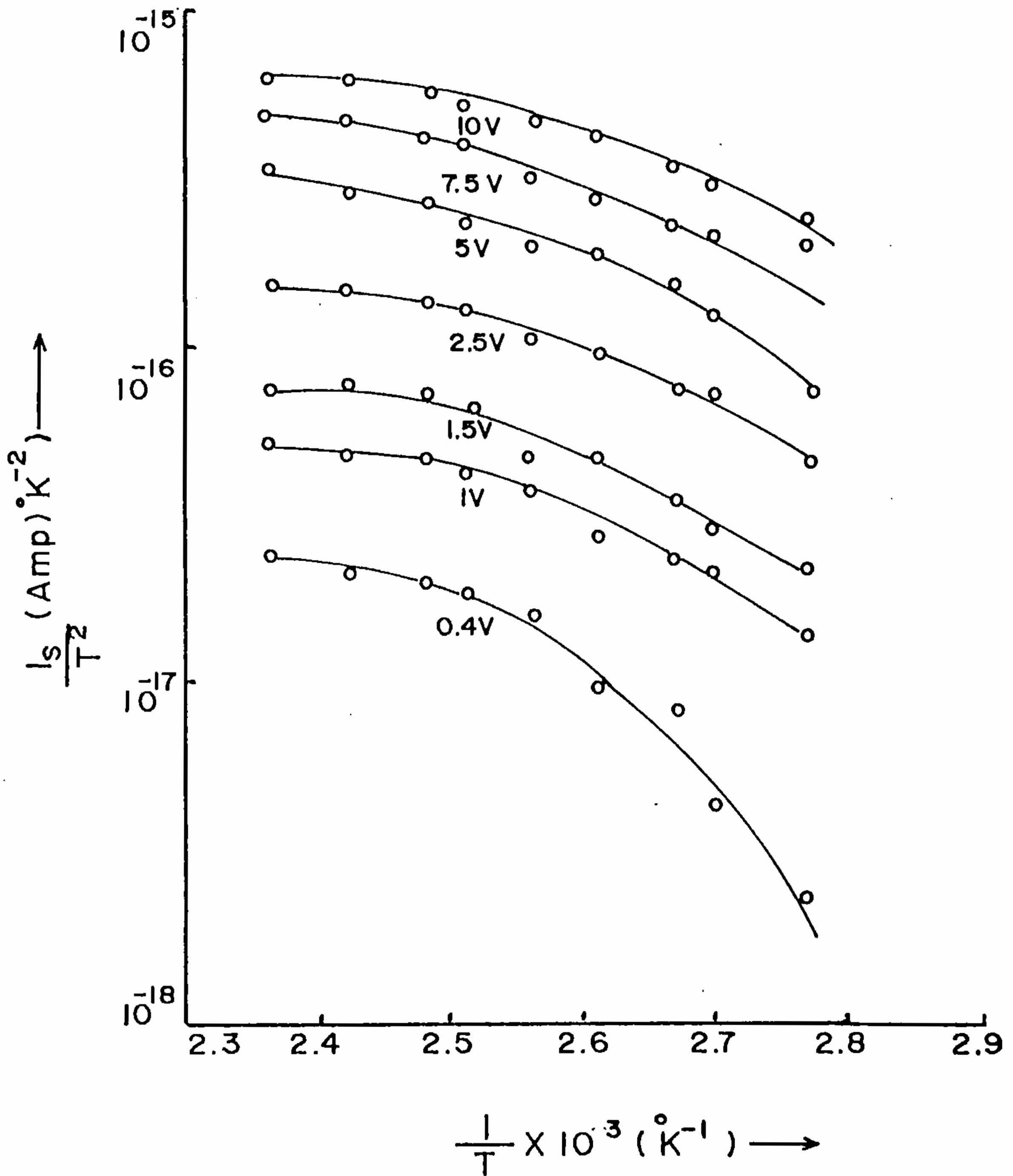

Fig.4.5(a) $I_s T^{-2}$- T^{-1} curves of an unformed Al-SiO-Al device with insulator thickness 1600Å at different voltages.

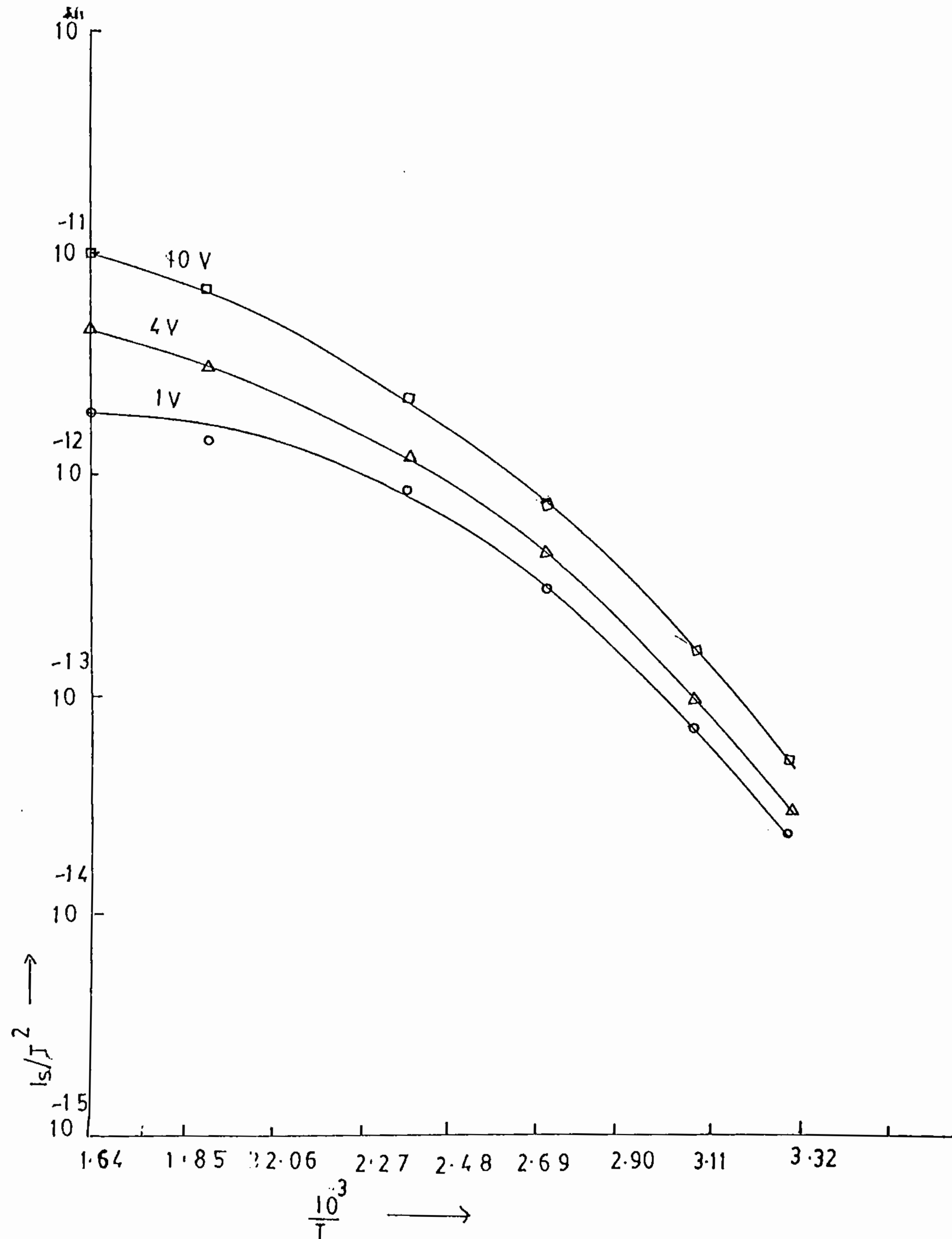

Fig.4.5(b) $I_s T^{-2} \sim T^{-1}$ curves of a pre-formed MIM device with insulator thickness 2000Å at different applied voltages.

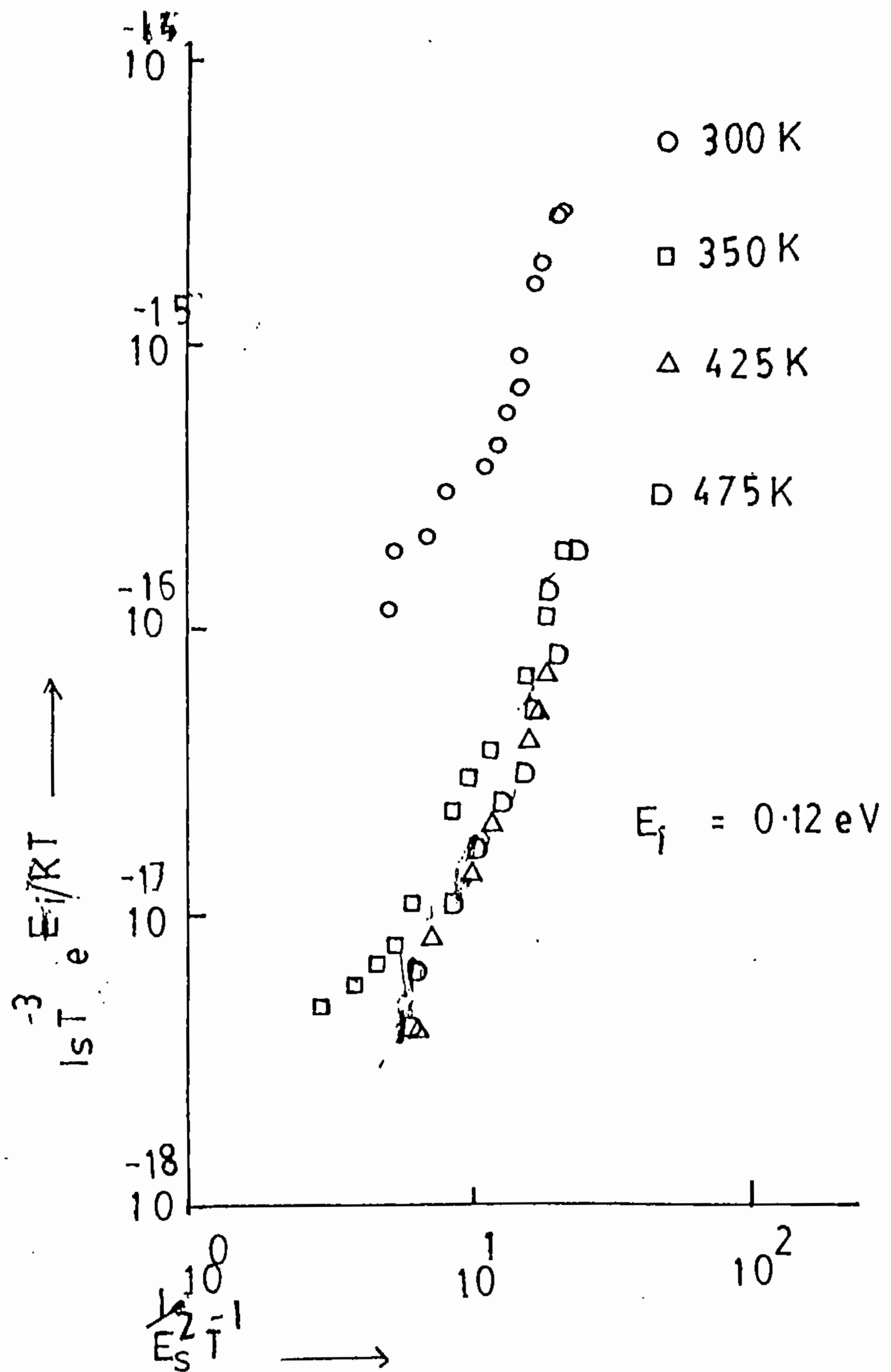

Fig.4.6(a_1) $I_s T^{-3} e^{Ei/KT} \sim E_s^{1/2} T^{-1}$ curves of an unformed MIM device with insulator thickness 1600A at E_1=0.12 ev at different temperatures.

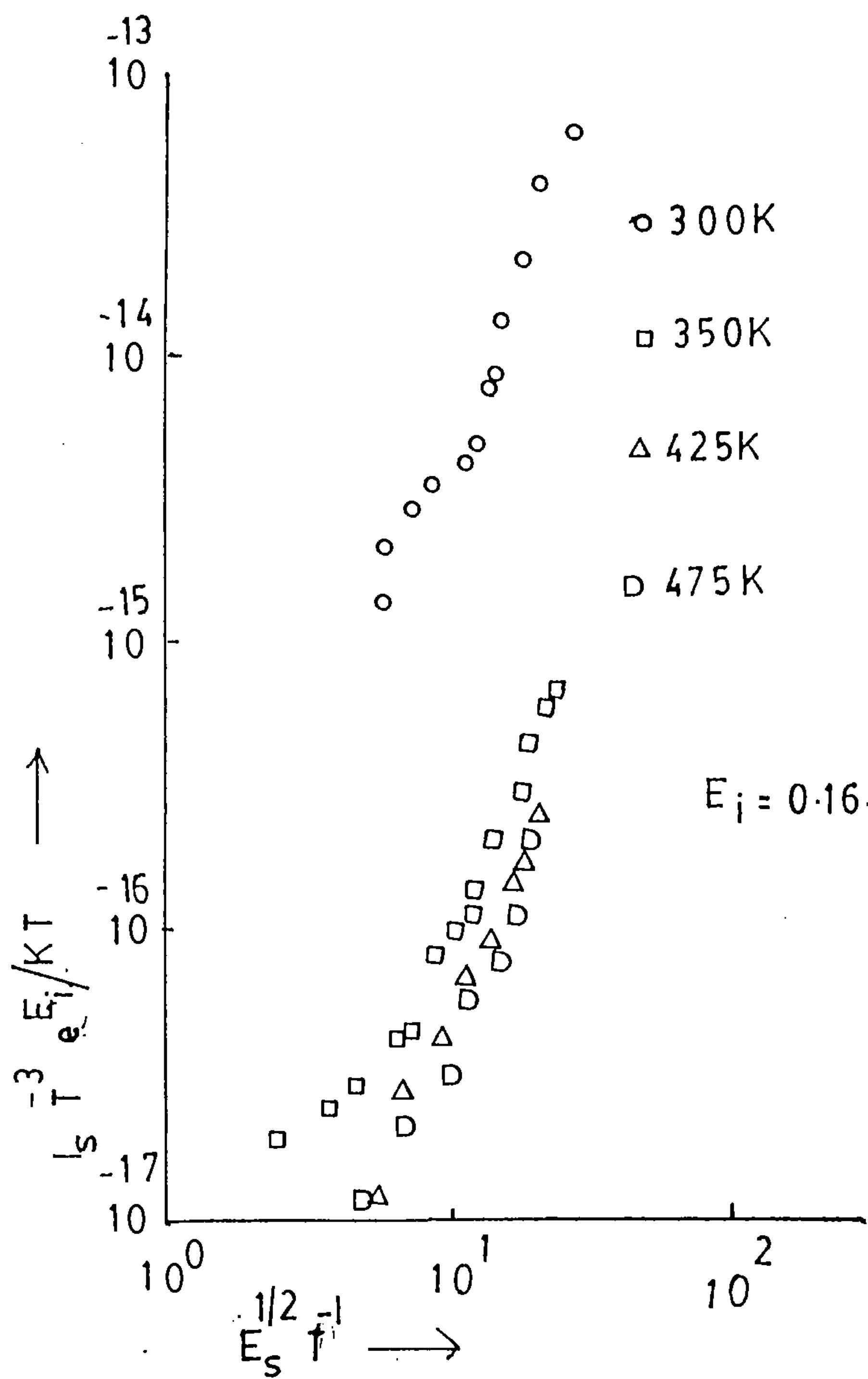

Fig.4.6(a_2). $I_s T^{-3} e^{E_i/KT} \sim E_s^{1/2} T^{-1}$ curves of an unformed MIM devices with insulator thickness 1600Å at E_i = 0.16 ev at different temperatures.

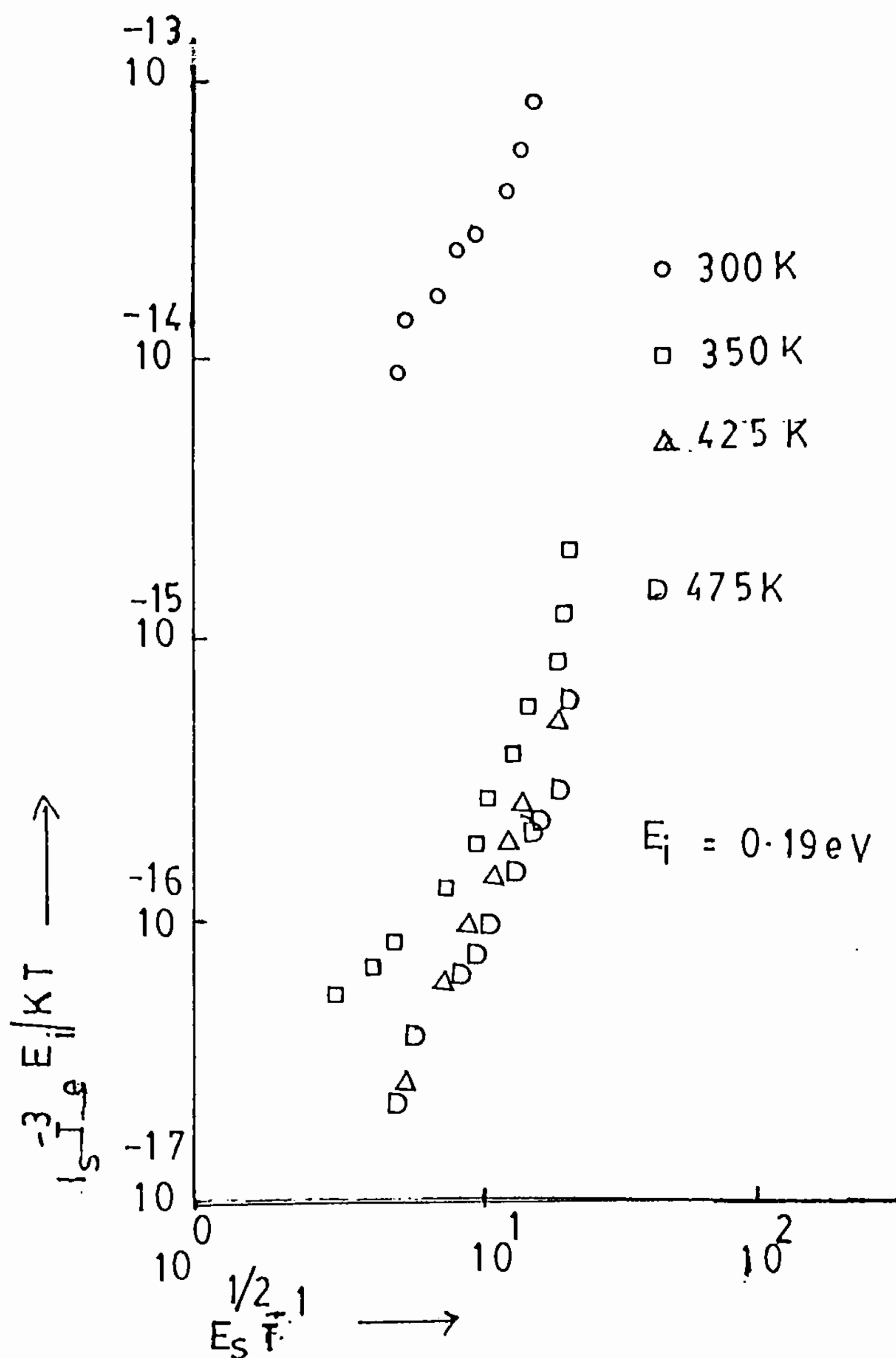

Fig.4.6(a_3) $I_s T^{-3} e^{Ei/KT} \sim E_s^{1/2} T^{-1}$ curves of an unformed MIM device with insulator thickness 1600Å at different temperatures.

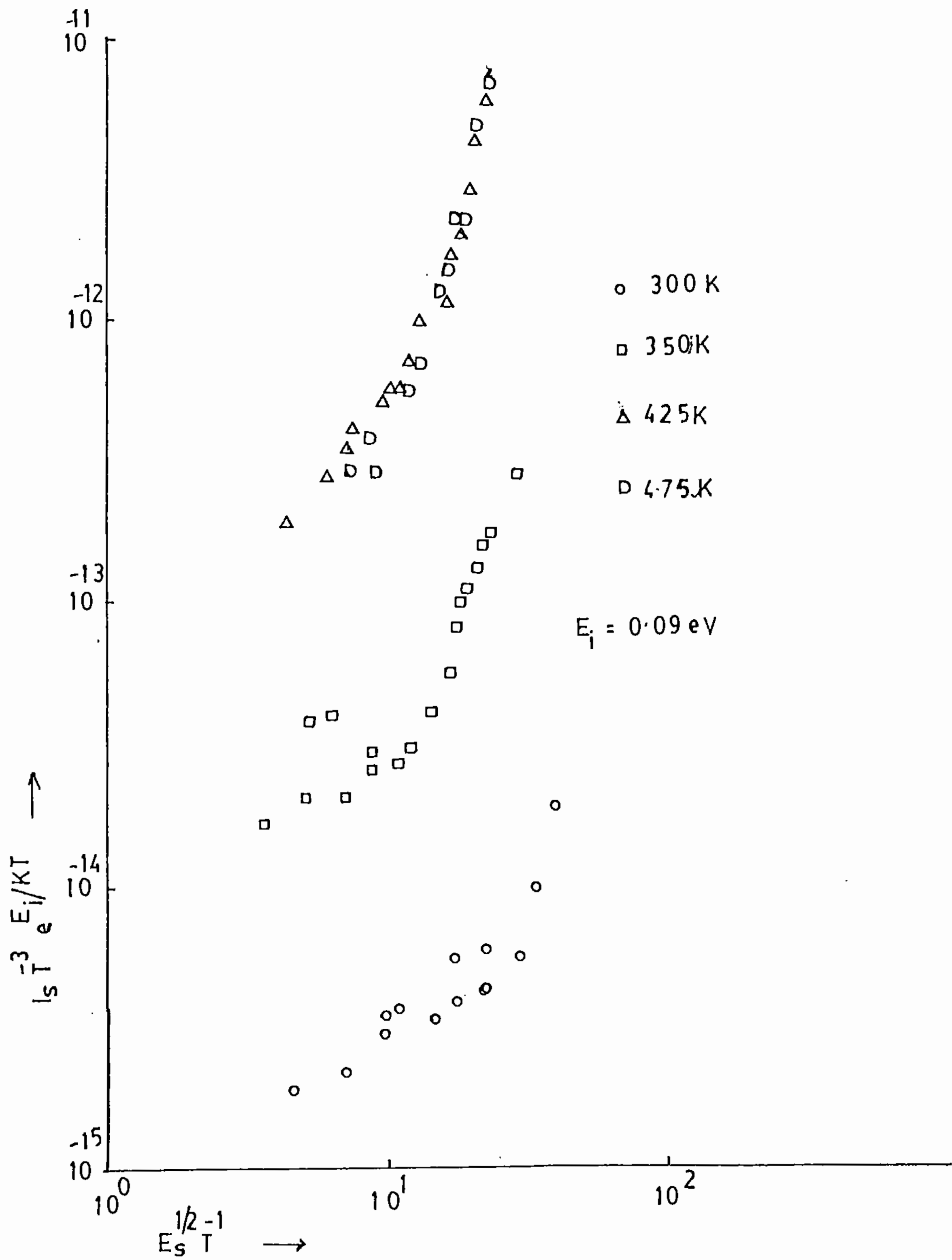

Fig.4.6(b_1) $I_s T^{-3} e^{Ei/KT} \sim E_s^{1/2} T^{-1}$ curves of a pre-formed MIM device with insulator thickness 2000Å at different temperatures at E_i = 0.09ev.

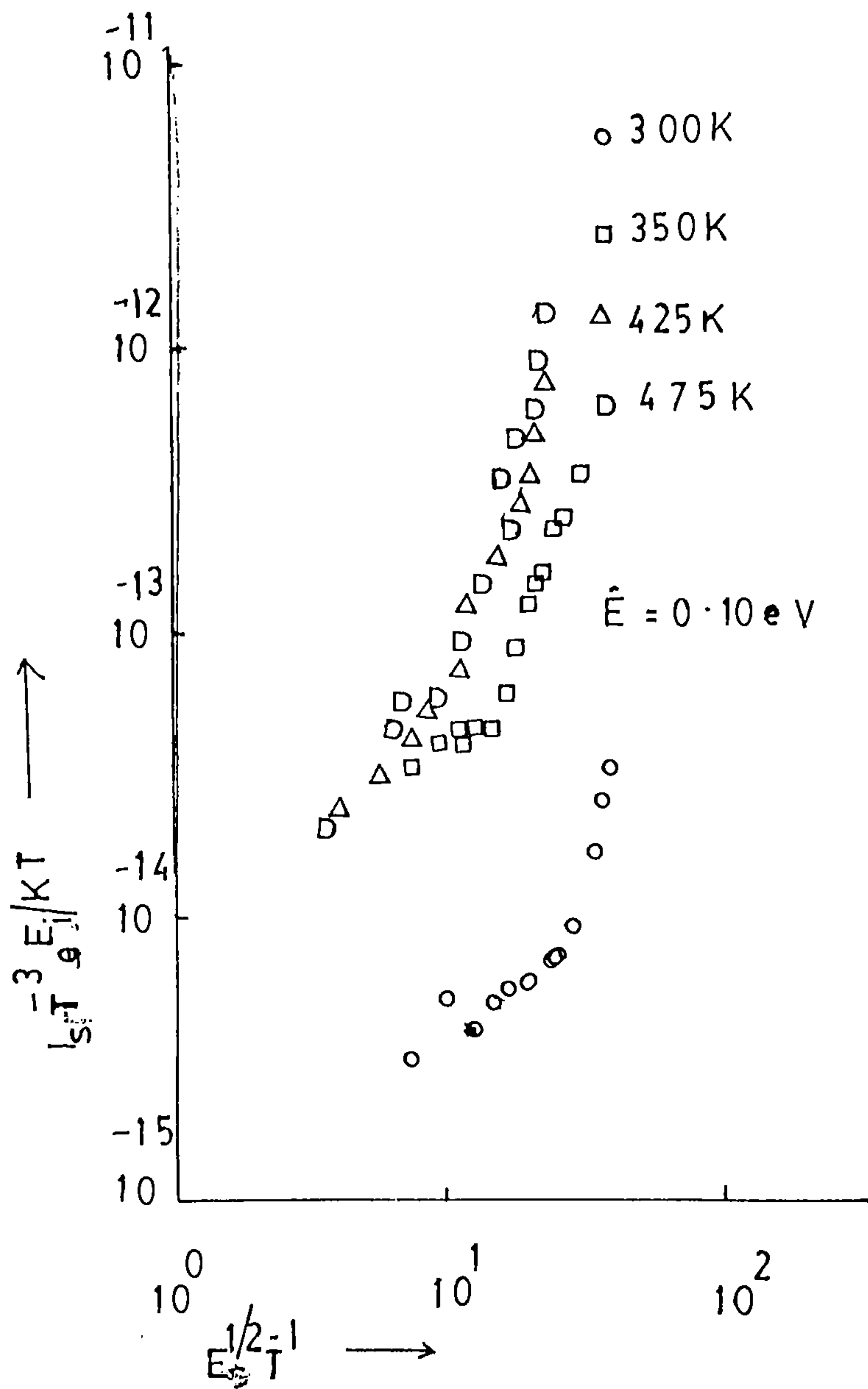

Fig.4.6(b_2) $I_s T^{-3} e^{Ei/KT} \sim E_s^{1/2} T^{-1}$ curves of a pre-formed MIM device with insulator thickness 2000Å at E_i = 0.10ev at different temperatures.

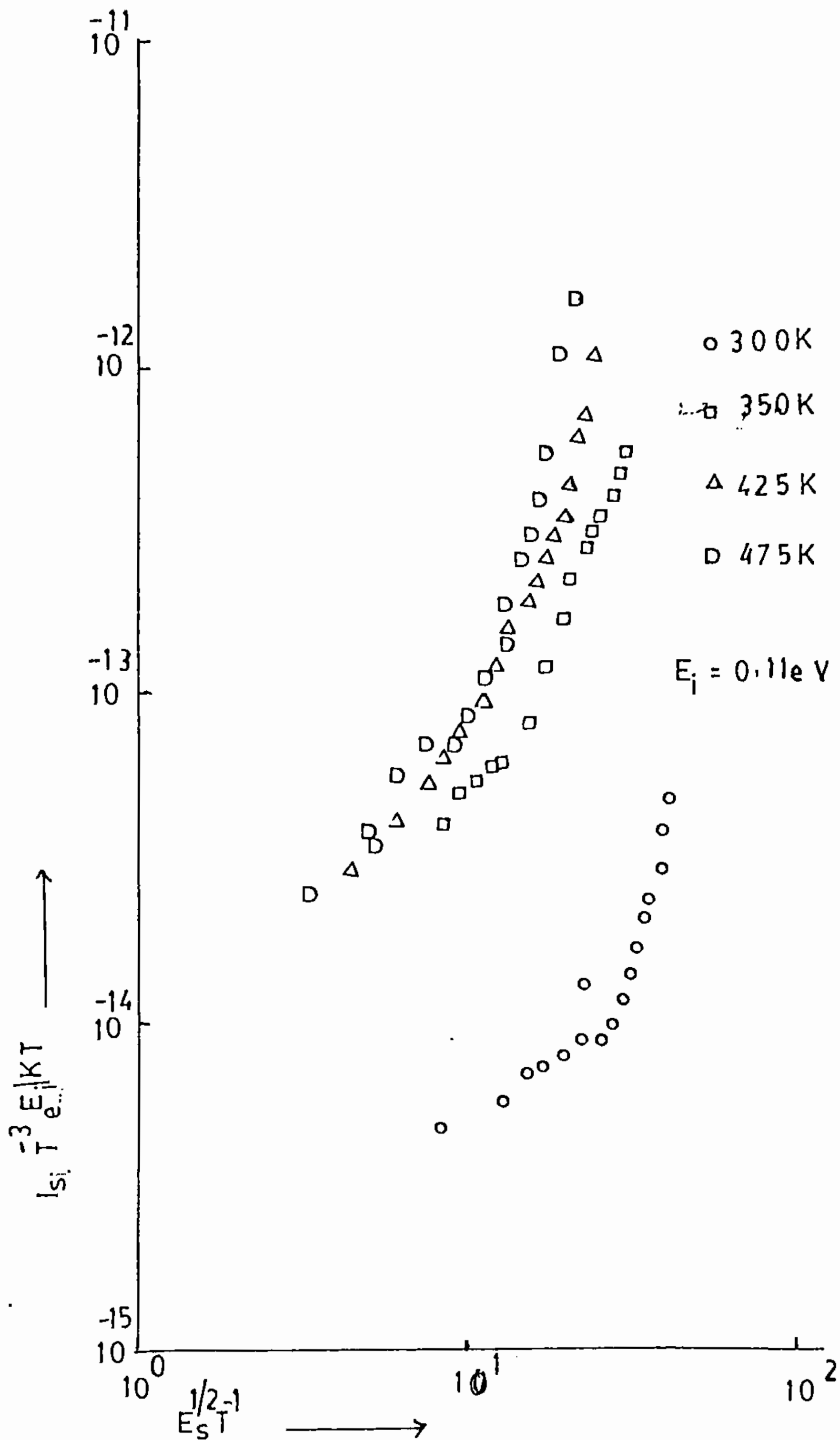

Fig.4.6(b_3) $I_s T^{-3} e^{Ei/KT} \sim E_s^{1/2} T^{-1}$ curves of a pre-formed MIM device with insulator thickness 2000Å at E_i = 0.11ev at different temperatures.

Table 5. Values of $\beta.\epsilon$ for the MIM devices.

MIM device	Minimum value of $E_s^{1/2}T^{-1}$	Value of β (10^{-5})	Values of the dielectric constant ϵ (n=4, Schottky) estimated	Values of the dielectric constant ϵ (n=1 Poole-Frenkel) estimated
Unformed Al-SiO-Al sandwich structure.	3.00	2.88	2.00	7.00
Preformed Al-SiO-Cu sandwich structure	3.60	2.44	2.50	10.00

4.1.2 AC Measurements In Unformed and Pre-formed MIM Devices

Ac measurements in thin insulating films provide precise information about the film materials. AC measurements have been carried out in unformed Al-SiO-Al as well as pre-formed Al-SiO-Cu sandwich devices. The AC results and their interpretation are presented below.

4.1.2.1 Analysis and Discussion of conductance G.

Fig. 4.7(a) represents the typical variations of conductance G with frequency for SiO films of different thicknesses in the unformed Al-SiO-Al sandwich devices whilst Fig. 4.7(b) represents the variations of conductance with frequency for SiO films of the various thickness in the pre-formed Al-SiO-Cu sandwich devices. Fig.4.7(c)-4.7(f) represent the variation of capacitances with thicknesses and temperatures for unformed pre-formed MIM devices.

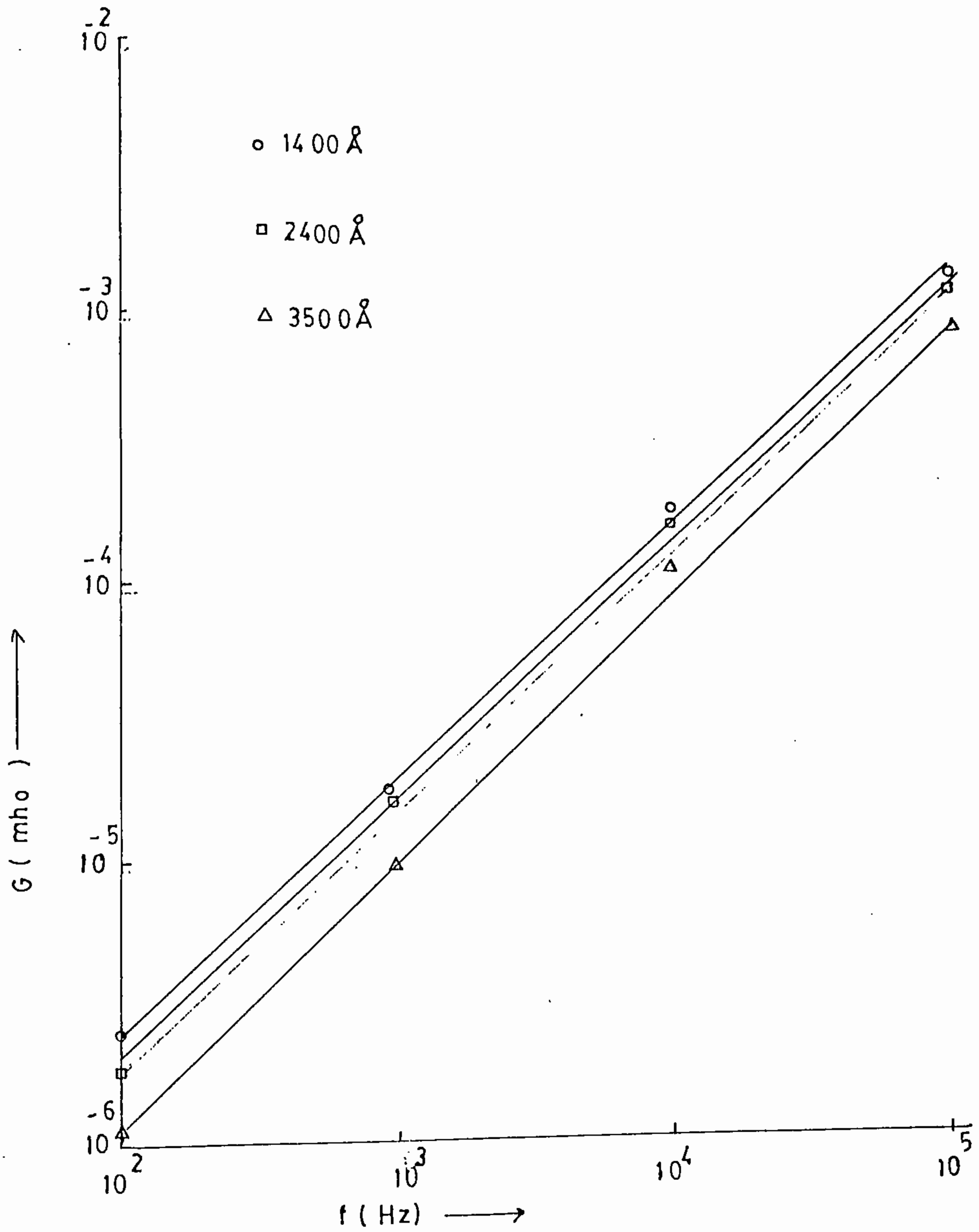

Fig.4.7(a) G~f curves of unformed Al-SiO-Al devices for different SiO thicknesses.

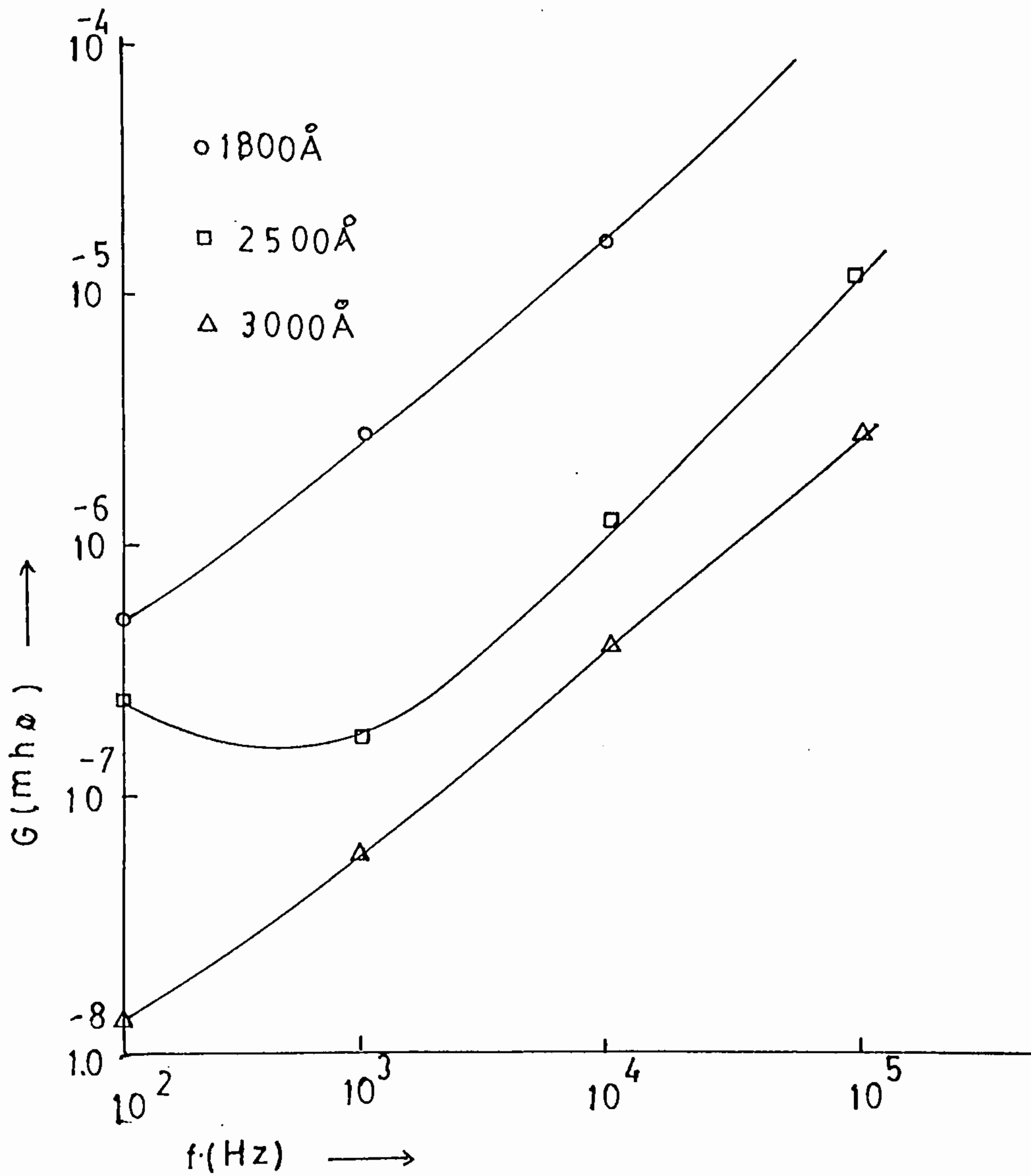

Fig.4.7(b) G ~ f curves of pre-formed Al-SiO-Cu devices with different insulator thicknesses.

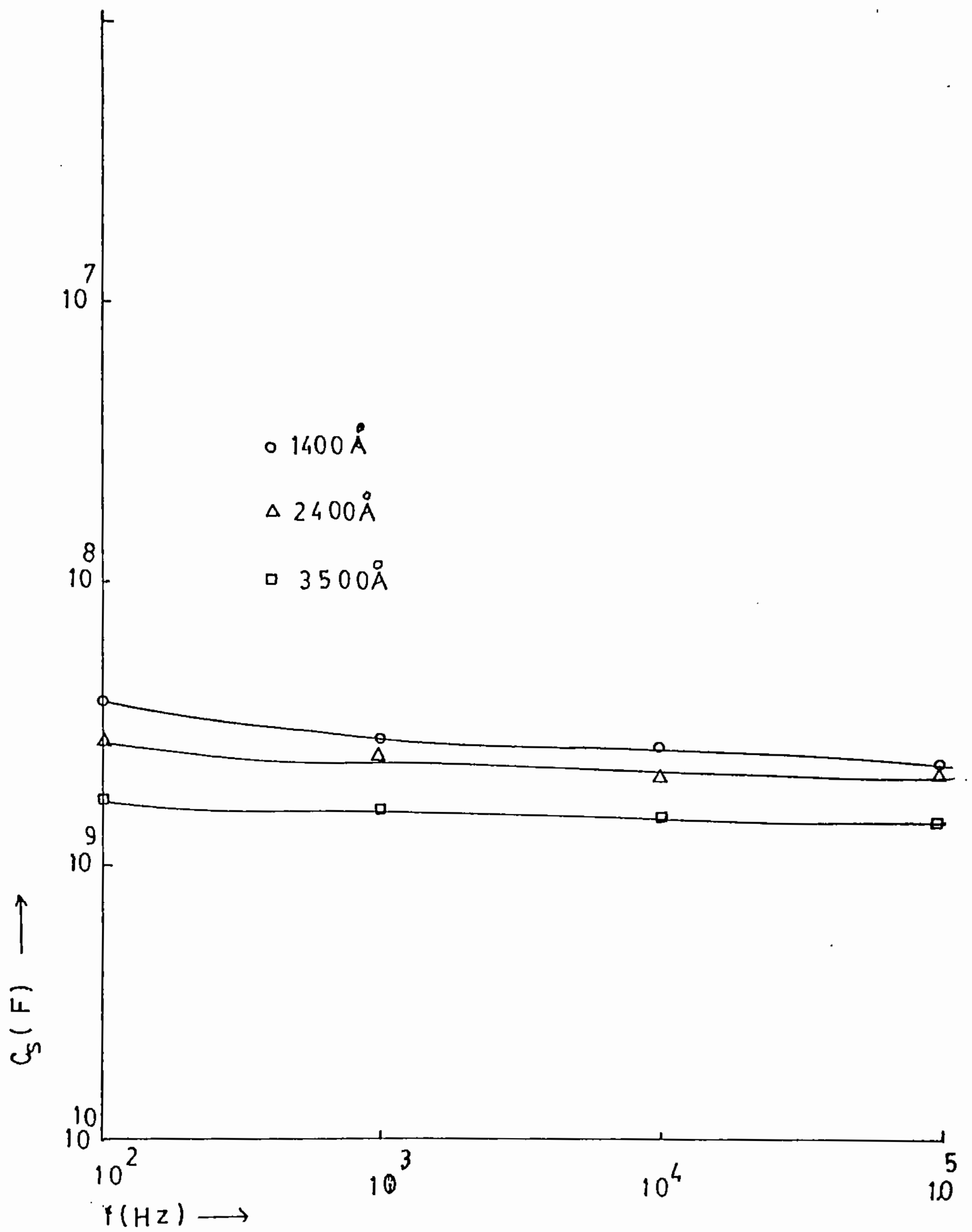

Fig.4.7(c) C - f curves of unformed Al-SiO-Al devices with different insulator thickness.

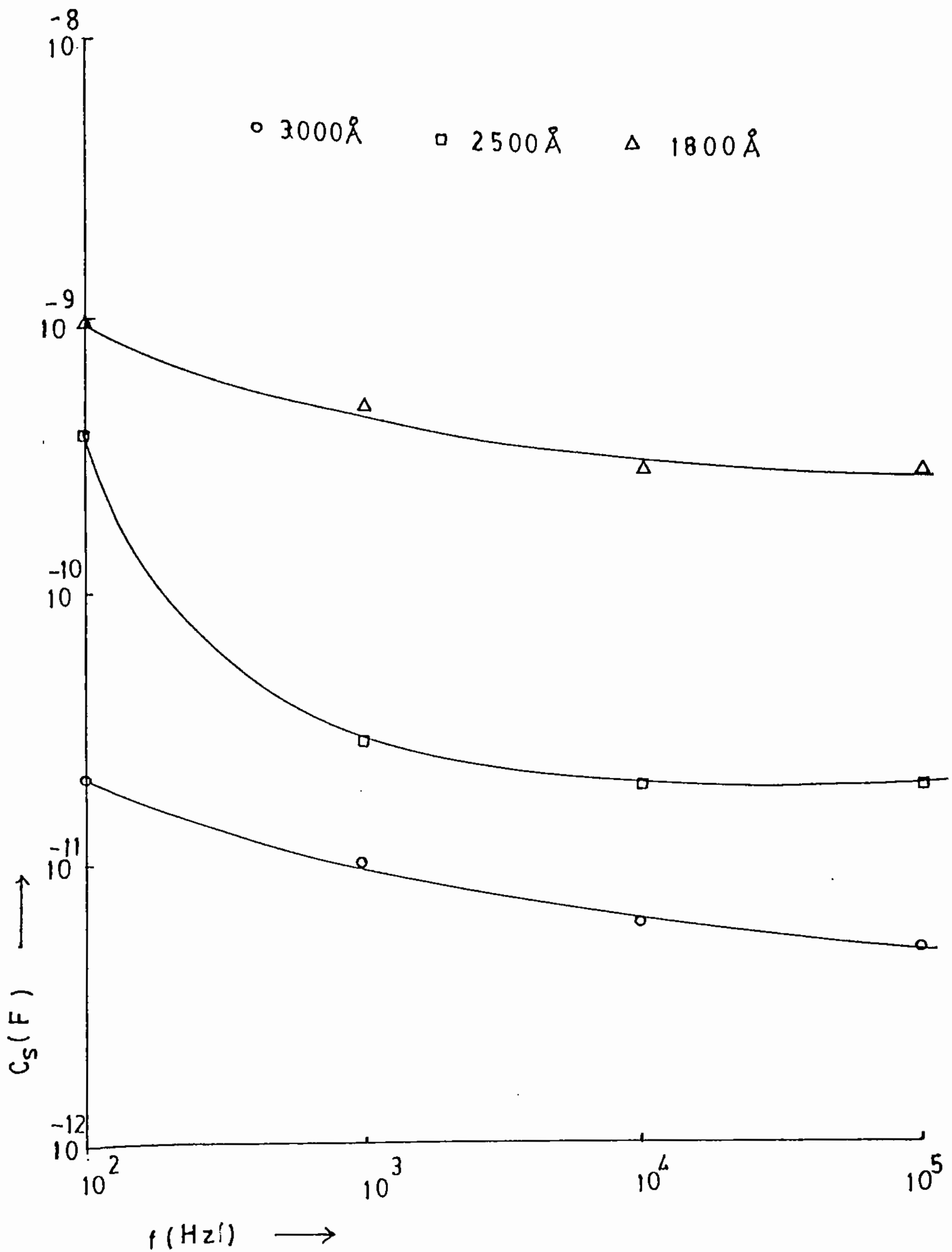

Fig.4.7(d) $C_s \sim f$ curves of pre-formed MIM devices with different insulator thicknesses.

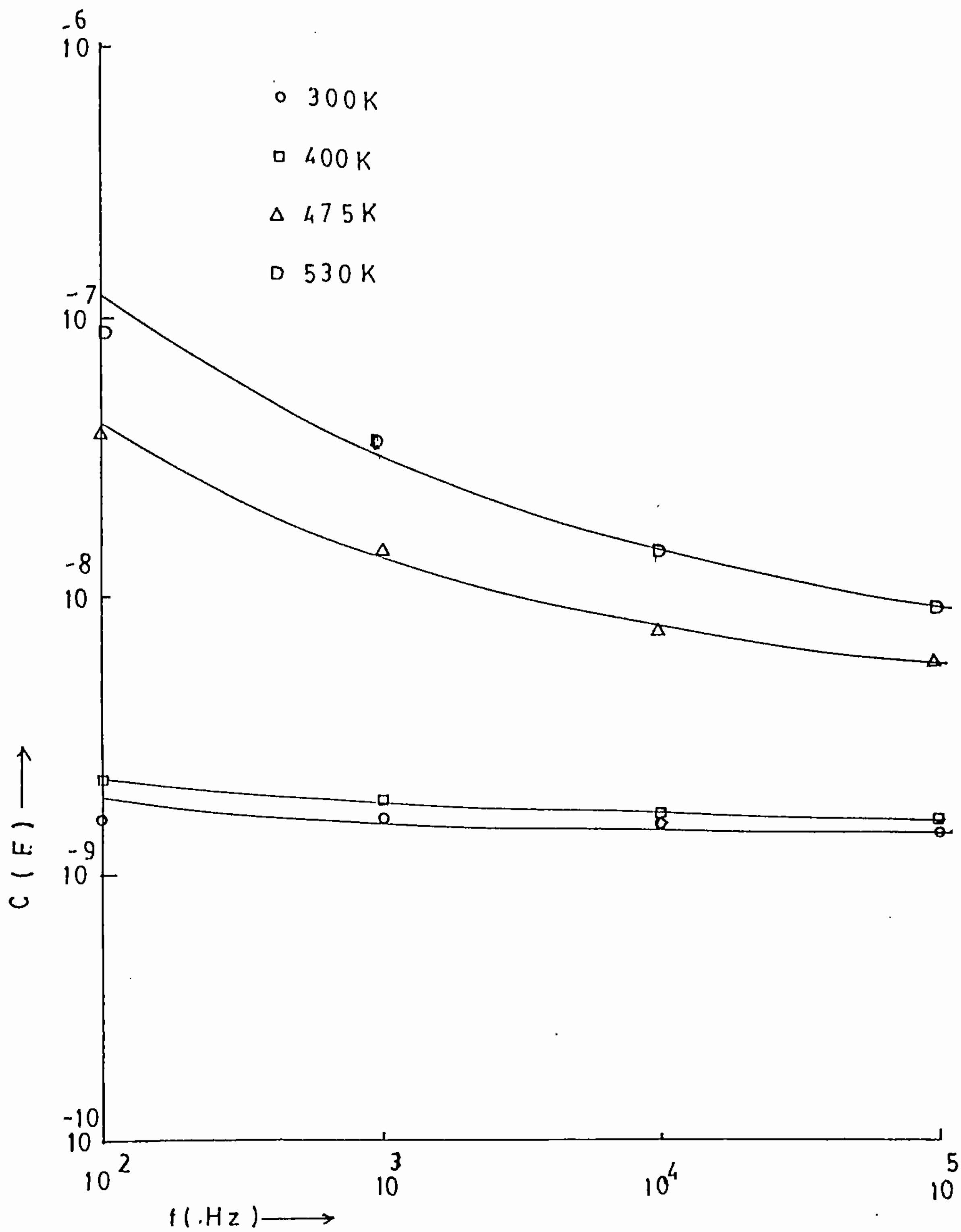

Fig.4.7(e) $C_s \sim f$ curves of an unformed Al-SiO-Al device with insulator thickness. 1400Å at different temperatures.

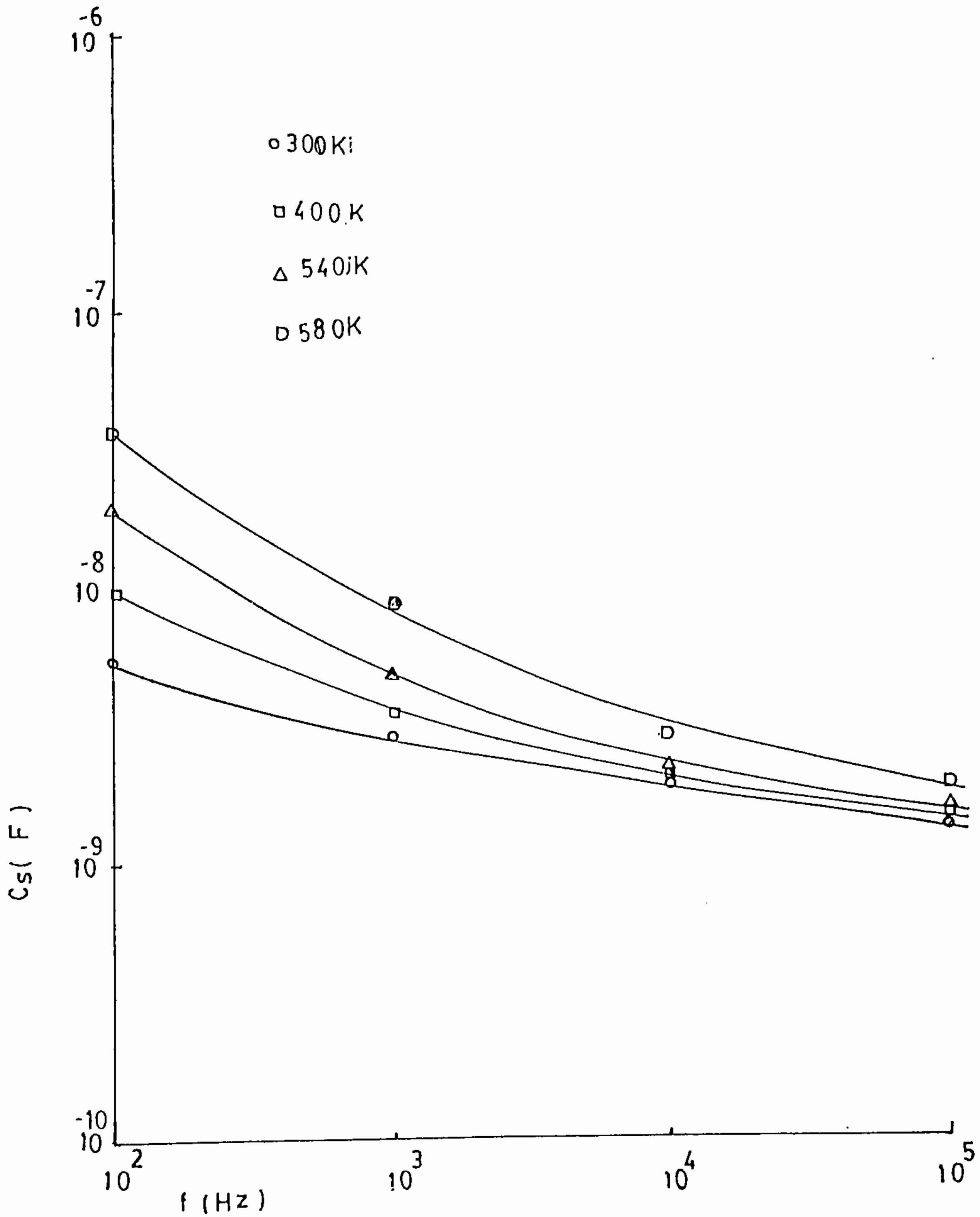

Fig.4.7(f) $C_s \sim f$ curves of a pre-formed MIM device with insulator thickness 2000Å at different temperatures.

It is seen from the graphs that the measured conductance obeys the following relation:

$$G = AW^{s} \quad \ldots \ldots (1)$$

where W is the angular frequency of the applied AC signal, A is a constant (complex in nature) which is weakly temperature dependent and the exponents is temperature dependent. Fig. 4.8(a) shows the variations of S with temperature for unformed Al-SiO-Al device while Fig.4.8(b) shows the variations of S with temperature for pre-formed Al-SiO-Cu device. From the graphs it can be shown that

$$S = (d\log G/d\log f) = -BT+C \quad \ldots \ldots (2)$$

where B and C are constants, f is signal frequency and T is the absolute temperature. Using equation 2 in equation 1 the following relation is obtained

$$G_{AC} \alpha f^{-(BT-C)} \quad \ldots \ldots (3)$$

Values of the parameters T, B, C & S are listed below in Table 5 for unformed and Table 6 for pre-formed MIM devices.

Table 5. Measured Values of the parameters T.S. B and C for an unformed MIM device.

Temperature(K)	Values of S	Value of B	Value of C
300	0.95		
400	0.90	1.65×10^{-3}	1.45
475	0.58		
530	0.57		

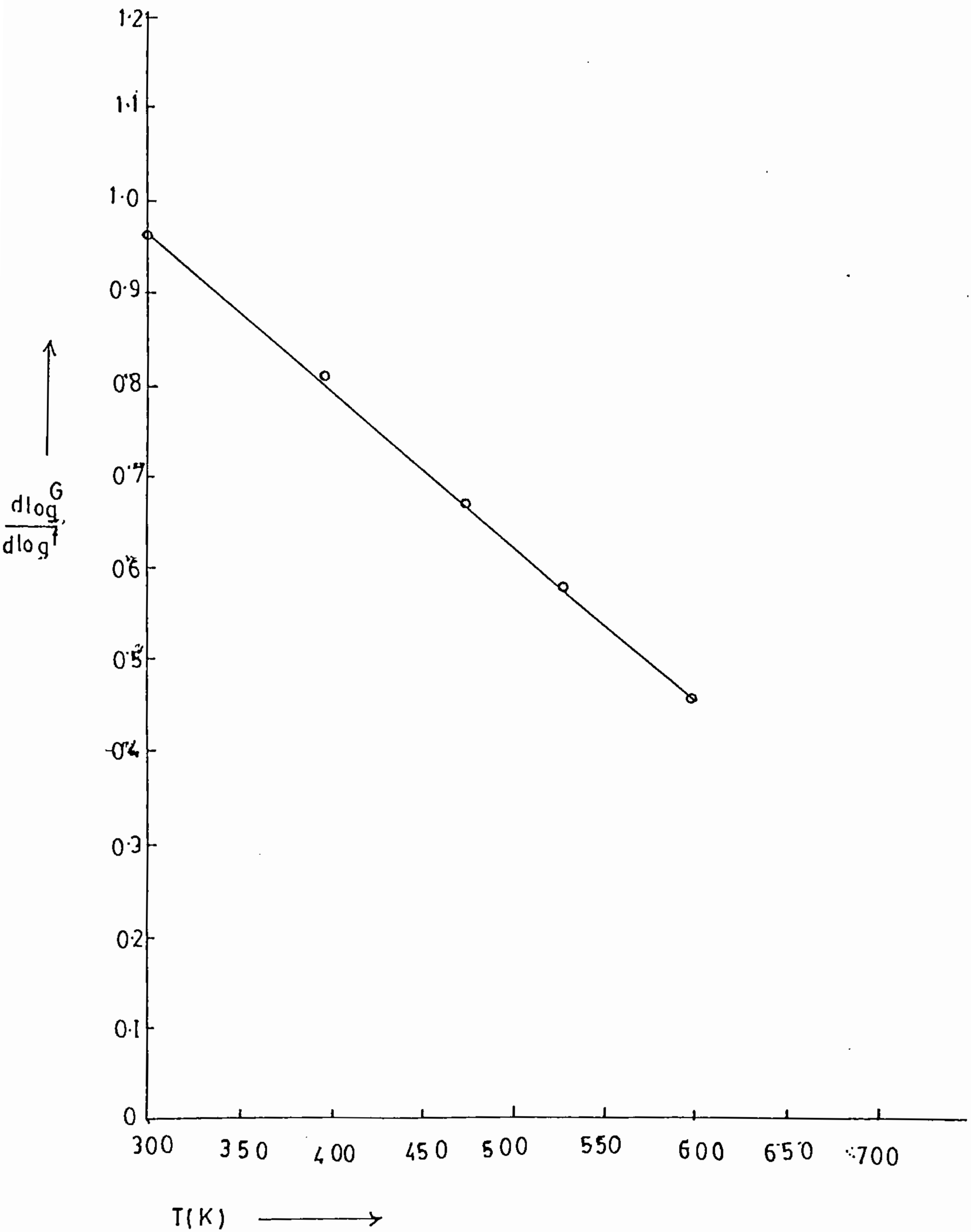

Fig.4.8(a) (dlogG/dlogf)$\sim$T curve of an unformed device with insulator thickness 1400Å.

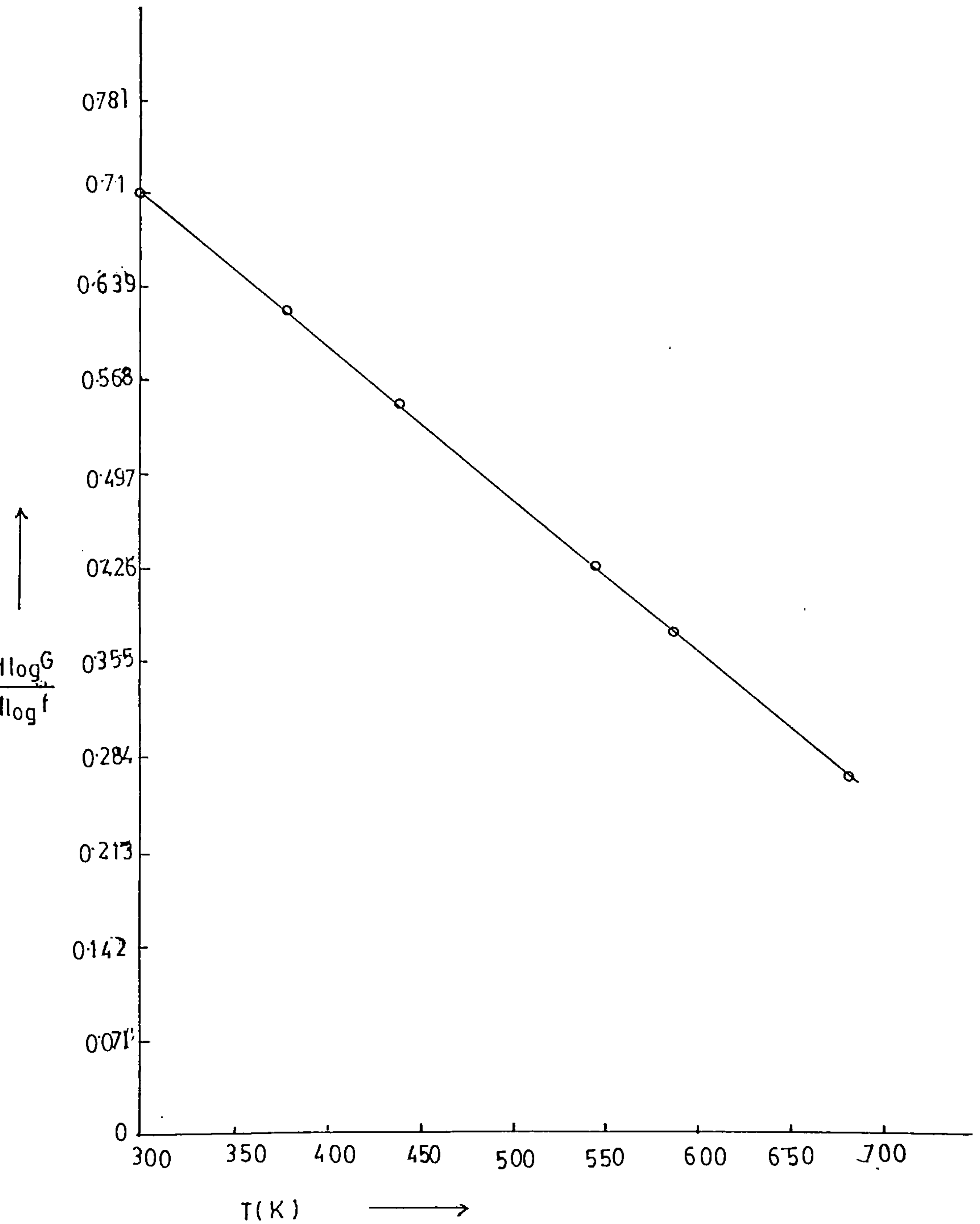

Fig.4.8(b).(dlogG/dlogf) ~ T curve of a pre-formed MIM device with insulator thickness 2000Å.

Table 6. Measured Values of the parameters T.S. B and C for a pre-formed MIM device.

Temperature(K)	Values of S	Value of B	Value of C
300	0.71		
400	0.47	1.18×10^{-3}	1.06
540	0.43		
580	0.38		

Fig.4.9(a) shows the variations of conductance with frequency at different temperatures for the unformed device and the Fig. 4.9(b) shows the similar variations for the pre-formed device.

Figs. 4.10(a) and 4.10(b) show the logG versus T^{-1} graphs at different fixed frequencies for the unformed and pre-formed devices respectively. Values of activation energy in different ranges of temperatures were calculated from the above figures and they are recorded in the tables 7 and 8.

Table 7. Values of the measured activation energy for the unformed devices.

Frequency	Thermal activation energy, E_{th}(eV)	
	300-450K	450-550K
100 Hz	0.070	0.170
1KHz	0.040	0.160
10 KHz	0.030	0.056
100 KHz	0.010	0.080

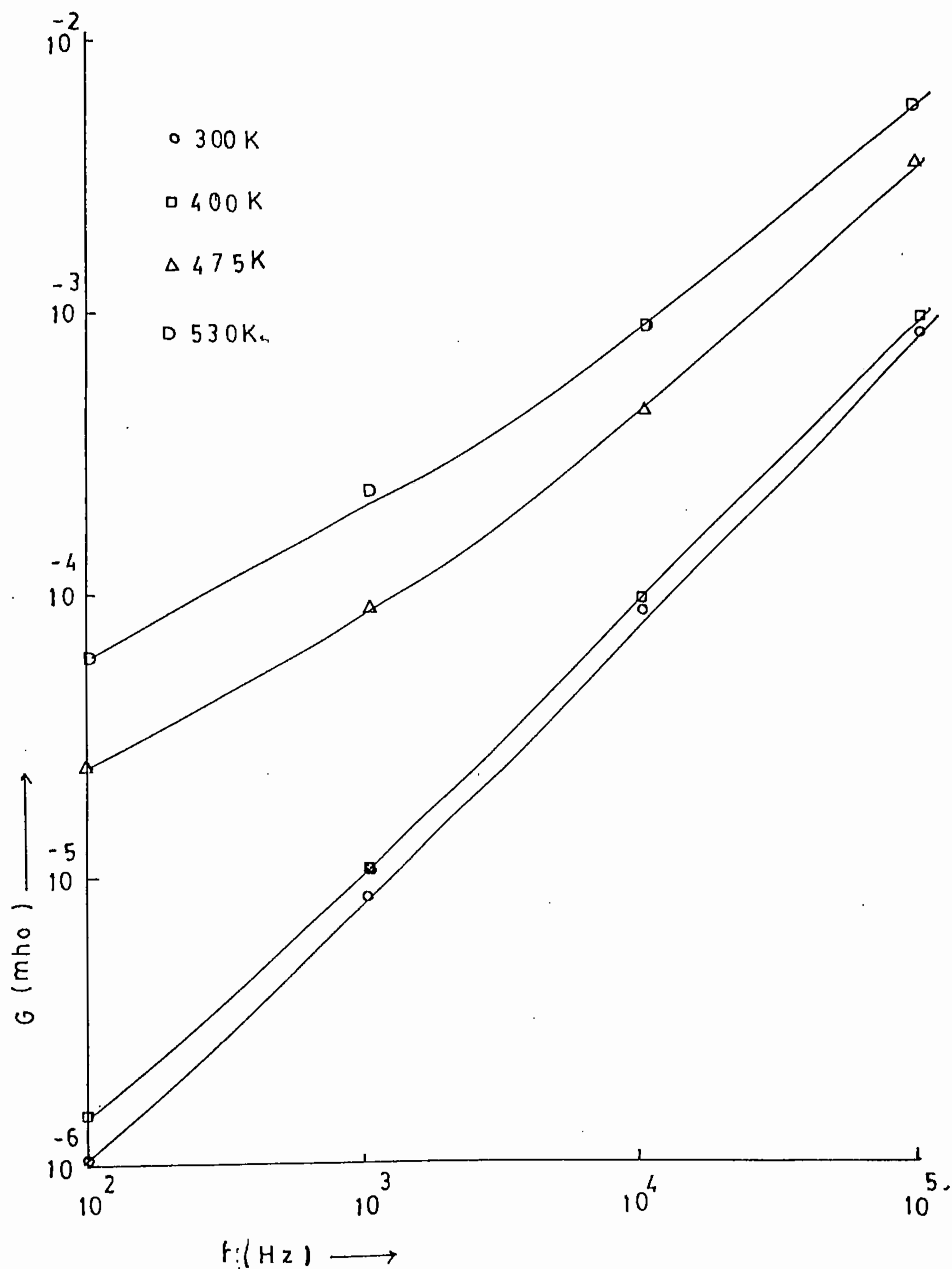

Fig.4.9(a). G~f curves of an unformed device with insulator thickness 1400Å at different temperatures.

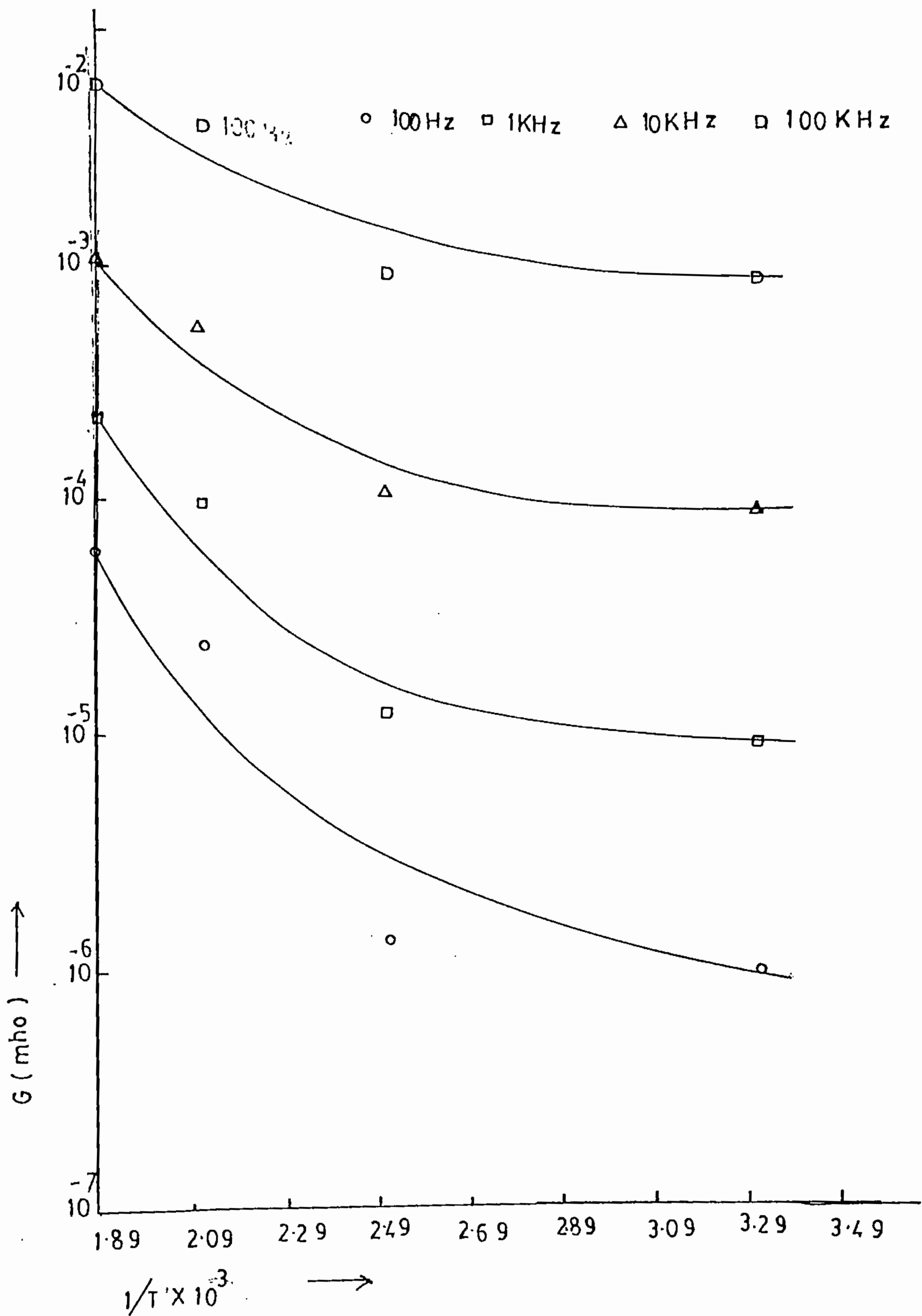

Fig.4.10(a). $G \sim T^{-1}$ curves of an unformed device with insulator thickness 1400Å at different frequencies.

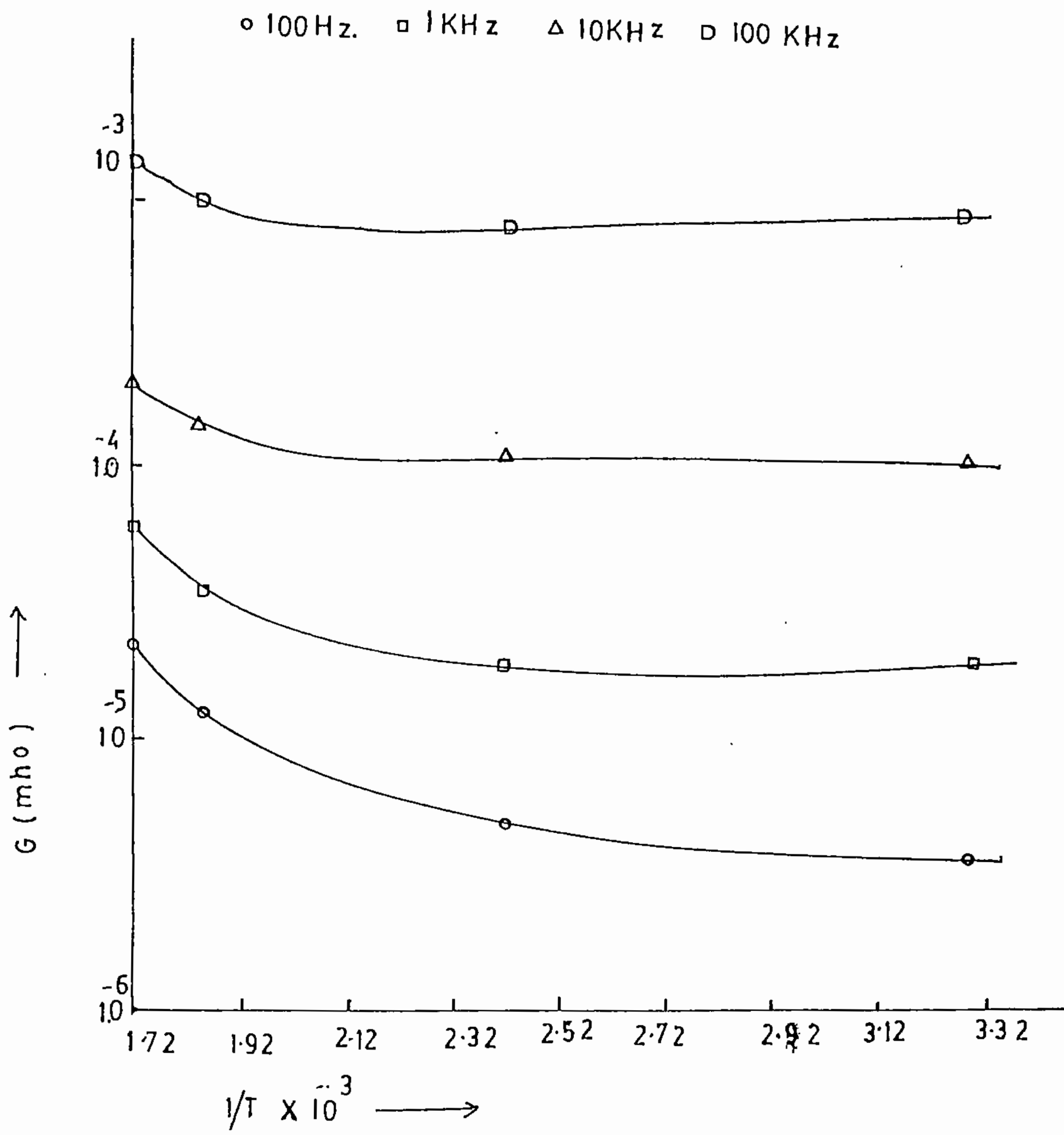

Fig.4.10(b). $G \sim T^{-1}$ curves of a pre-formed device with insulator thickness 2000Å at different frequencies.

Table 8. Values of the measured activation energy for the pre-formed devices.

Frequency	Thermal activation energy, E_{th}(eV)	
	300-450K	450-550K
100 Hz	0.020	0.090
1KHz	0.020	0.070
10 KHz	0.006	0.046
100 KHz	0.002	0.029

From tables 7 and 8 we see that in the low temperature regions the activation energies lies in the range 0.002-0.080 ev. This low values of activation energy may be attributed to electronic hopping conduction operating in the devices. In the highr temperature regions the values of the activation energy lie in the range 0.16-0 17 ev. The conduction at higher temperatures is seemingly a process and so a transition from hooping to free band conduction takes place. The gradual transition from hoping to free band conduction may be due to a overtopping of localized levels and the free band (Anwar and Hogarth, 1989).

It can be seen from the logG˜Logf graphs of Figs. 4.9(a) and 4.9(b) that at low values of frequency the logG˜Logf relation is found to be truly linear. The values of S evaluated from Fig.4.9(a) lie in the range 0.60 - 0.95 (Table 5) and the values of S found from Fig. 4.9(b) lie in the range 0.40 -0.70 (Table-6). It is seen that the values of S are nearly unity and are temperature sensitive.

It is also seen from Fig. 4.9(a)-4.9(b) and 4.10(a)-4.10(b) that the values of the conductivity increase with decreasing

frequency and increase with increasing temperature. The multiple hops will result in a decrease frequency dependence and increasing temperature dependence (Pallak, June 14, 1965). Thus we should say that the multiple hopping processes are responsible for the AC conductivity in our samples.

Similar Ac behavior has also been observed in dielectric films by many investigators () Elliott, 1977, Nadkarni *et al.* 1982, Balasubramanian *et al.* ( ), Kannan *et al* 1990, Jayaraj *et al*, 1989, Dutta *et al* 1982. They have explained their results on the basis of rapid transitions between localized vacancy states.

The oxygen vacancies in the oxide compounds capture electrons from the donors and the captured electrons are transformed to the conduction band thereby increasing the conductivity. Oxygen deficiency results in the formation of dipoles which contribute to the conductivity of SiO films. The observed behavior of the AC conductivity may also be attributed to defects in SiO films caused by composition during the evaporation process and by movement of the dipoles under the influence of the external field.

4.1.3 VCNR, Swichings and electron emission in the Al-SiO-Cu/Al-V_2O_5-Cu/Al-V_2O_5-Al Sandwich devices.

Fig.4.11 shows the I_s-V_s characteristics of pre-formed and formed Al-SiO-Cu sandwich device for oxide thickness 1800Å. The impedance of a pre-formed sample measured at ambient is very high as observed in Fig.4.12. But the sample placed in a modest vacuum a few micron pressure or less) showed conductivity having magnitude three orders (minimum) higher than that of th preformed value for

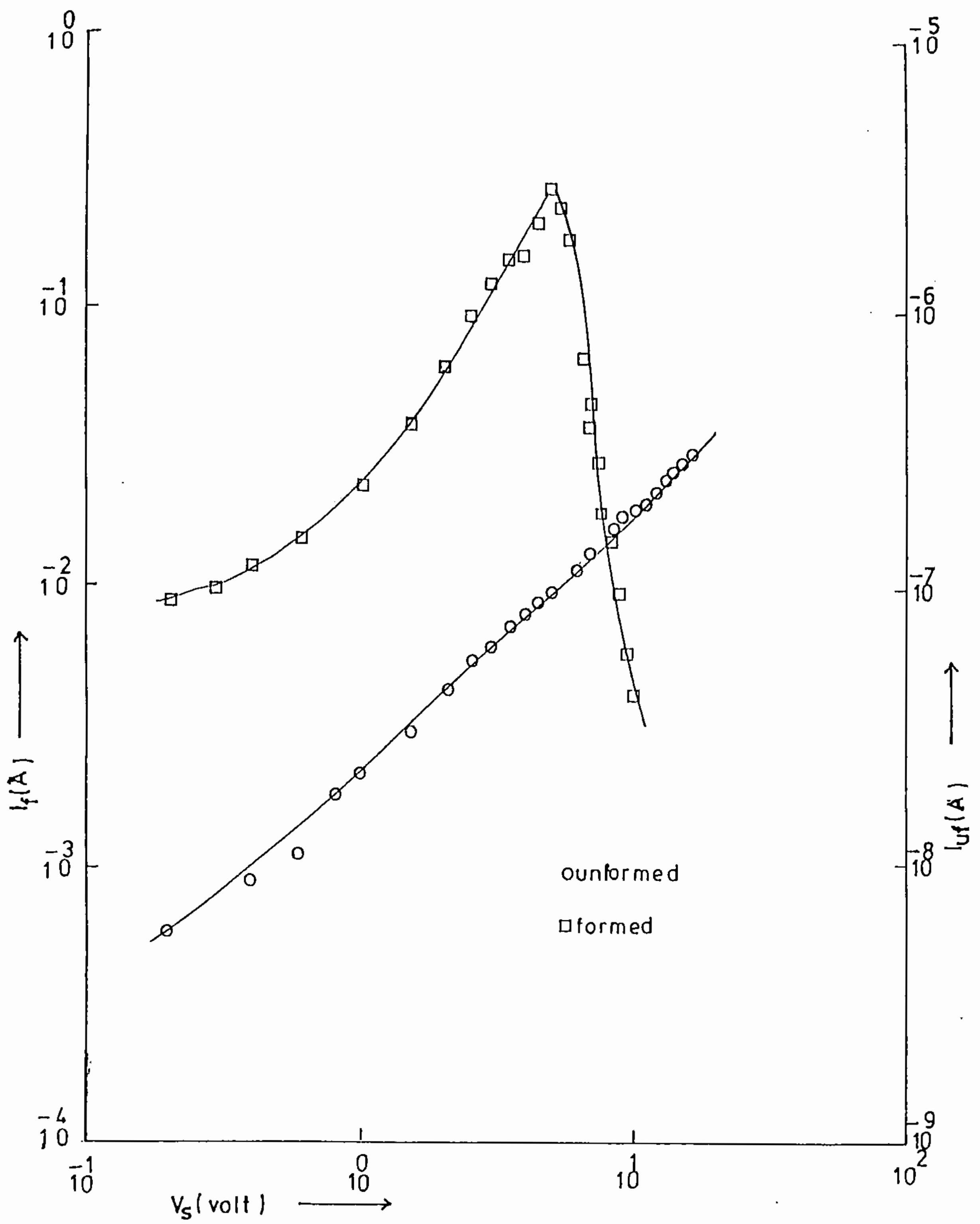

Fig.4.11. Unformed and formed I_s-V_s characteristics of an Al-SiO-Cu sandwich with insulator thickness 1800Å.

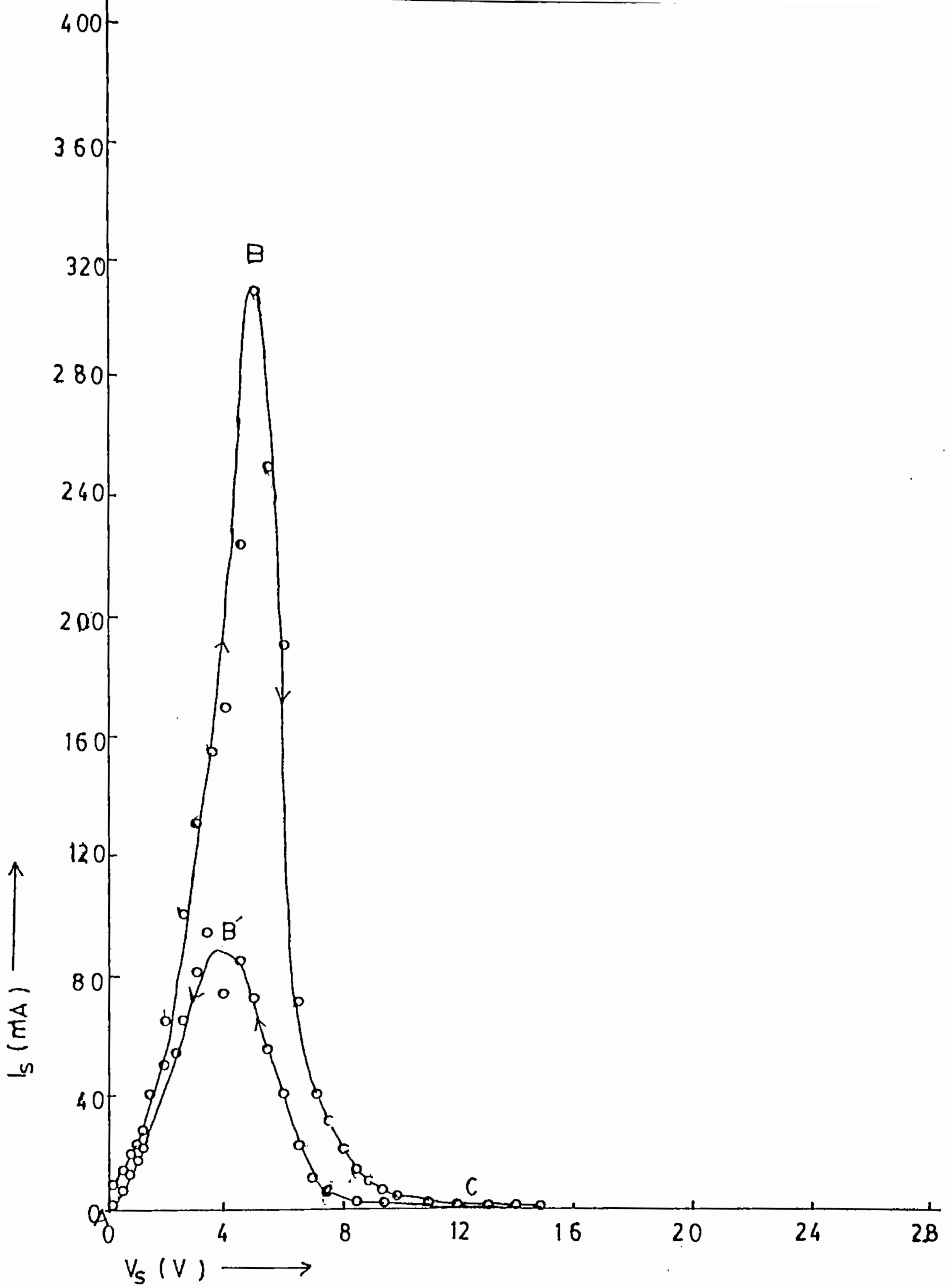

Fig.4.12. Formed I_s-V_s characteristics with increasing and decreasing bias voltages of an Al-SiO-Cu sandwich with insulator thickness 1800Å.

the same applied bias. In addition to this effect a pronounced VCNR region is also observed in both forward and reverse cycling of voltages shown in the Figs. 4.12-4.15 Switching and electron emission phenomena were also found in these devices.

There are various models to explain these anomalous behavior. In the present devices modified filamentary model of Hogarth *et al.* has been employed. The changes in conductivity is permanent. This is termed electroforming. According to this model the forming process can be readily shown to be due to ion injection into the insulator. The source of these ions being the positively biased copper electrode. The filaments are formed due to the migration of copper ions from the positive copper electrode.

The forming process brings about the growth of conducting filamentary paths between the two electrodes.These conducting paths are ohmic i.e., with a negligible activation energy for migration of carriers. The peak values of the current in the graphs of Figs. 4.12-4.15 which appear at the bias 4.5V correspond to the growth of filaments across the electrodes while the current on right side of the peak current values correspond to the rupturing of filaments due to Jaule heating effect. The humps on the I_s-V_s characteristics as shown in the Figs. 4.12-4.15 appear due to growth, rupturing regrowth of filaments. From the above figures we see that the value of the forming current depends on the value of the film thickness.

Fig.4.16 shows the variation of forming voltage and current with temperature. The forming voltage is approximately temperature independent and the pattern of the variation of forming current with temperature is still unknown..

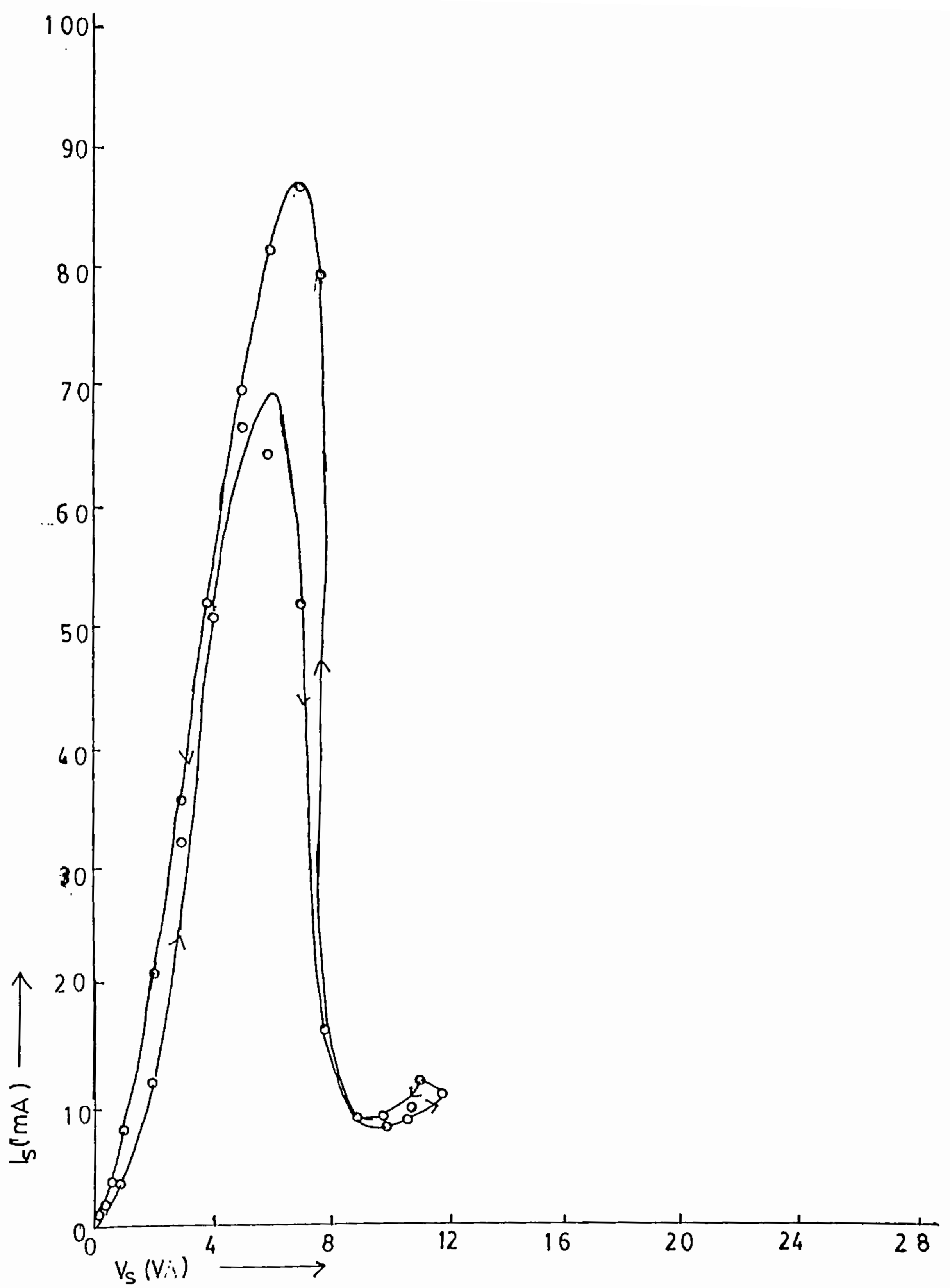

Fig.4.13. Formed I_s-V_s characteristics with increasing and decreasing bias voltages of an Al-SiO-Cu sandwich structure with insulator thickness 2000Å.

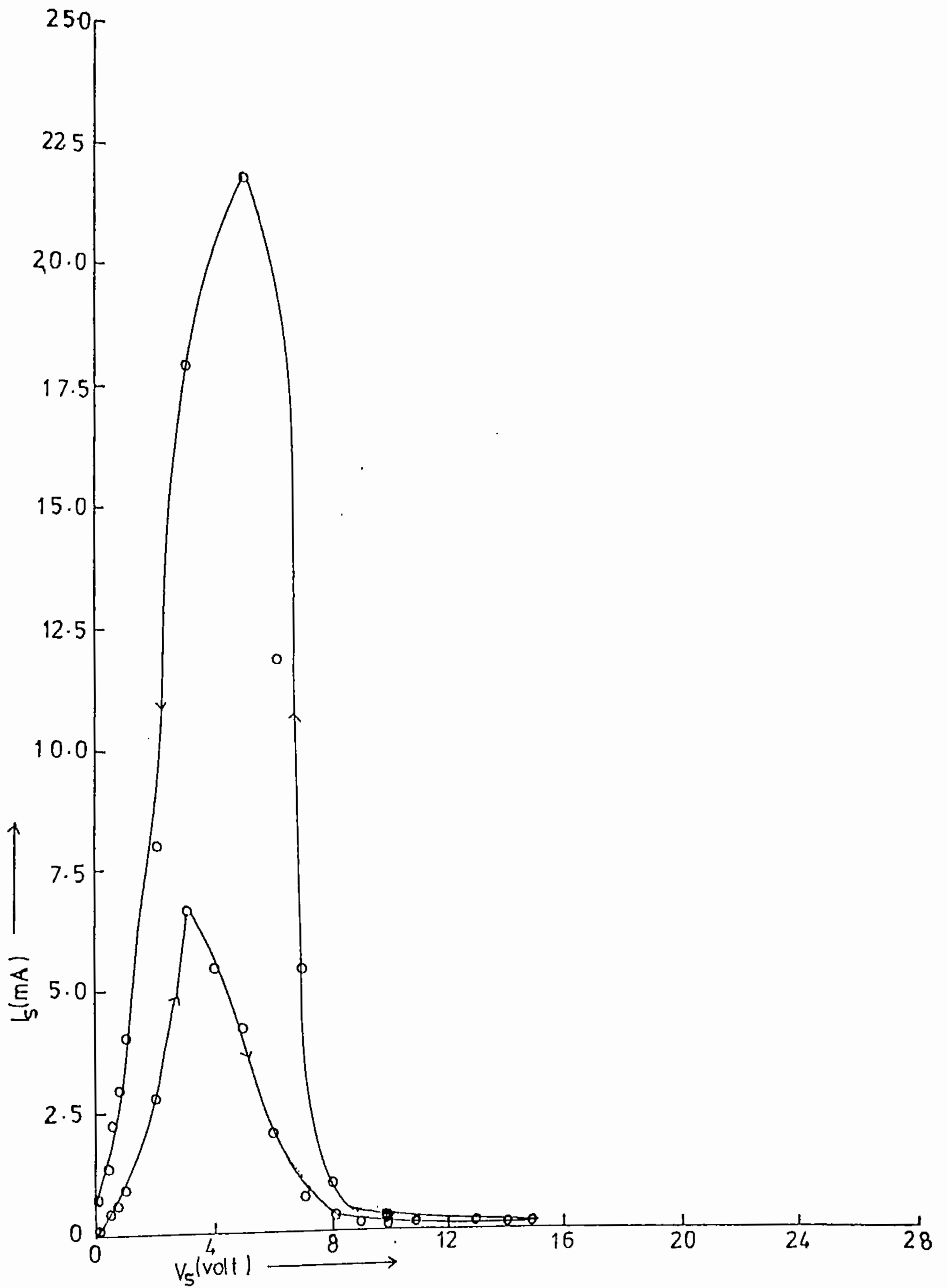

Fig.4.14. Formed I_s-V_s characteristics with increasing and decreasing bias voltages of an Al-SiO-Cu sandwich structure with insulator thickness 3700Å.

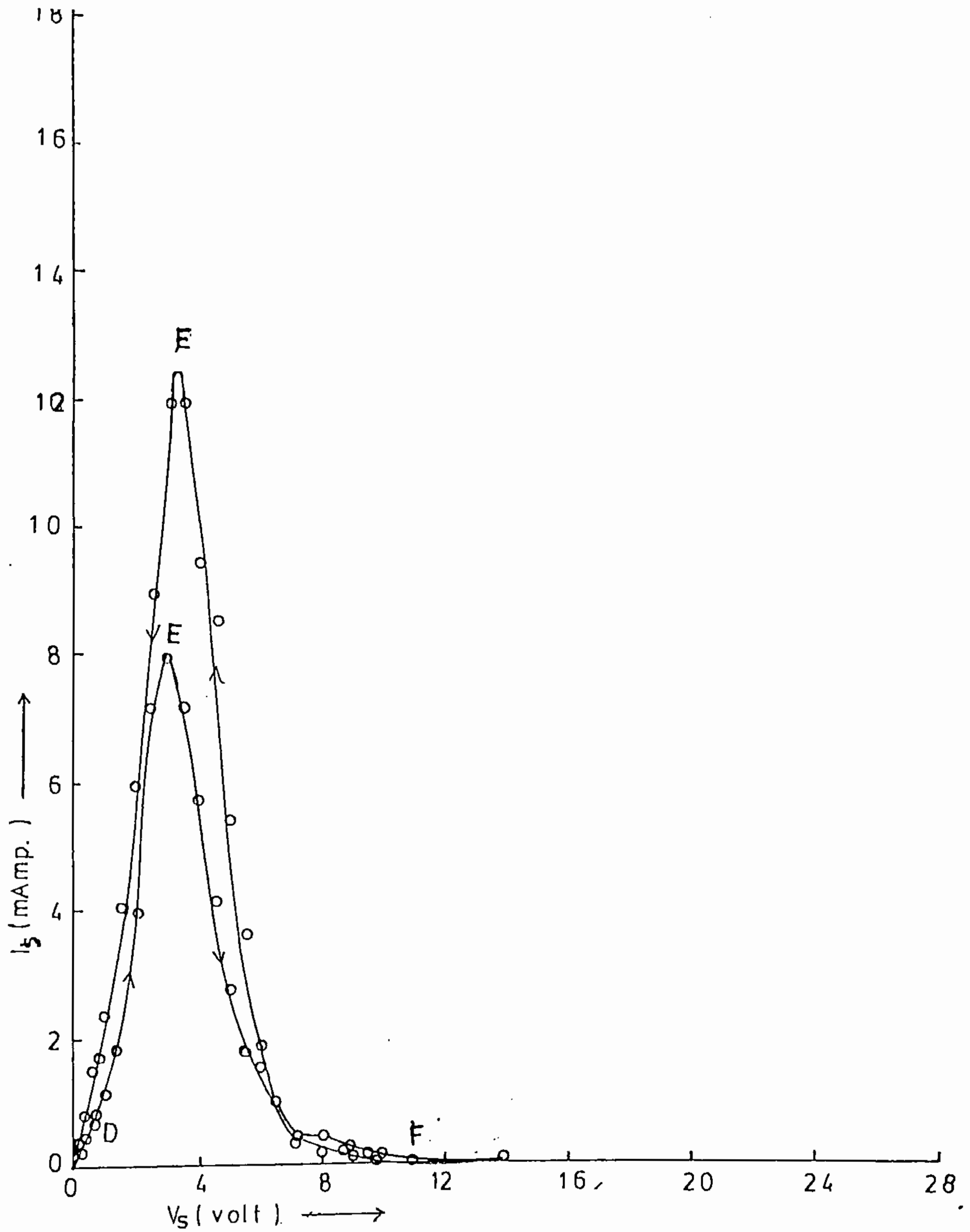

Fig.4.15. Formed I_s-V_s characteristics with increasing and decreasing bias voltages of an Al-SiO-Cu sandwich structure with insulator thickness 5900Å.

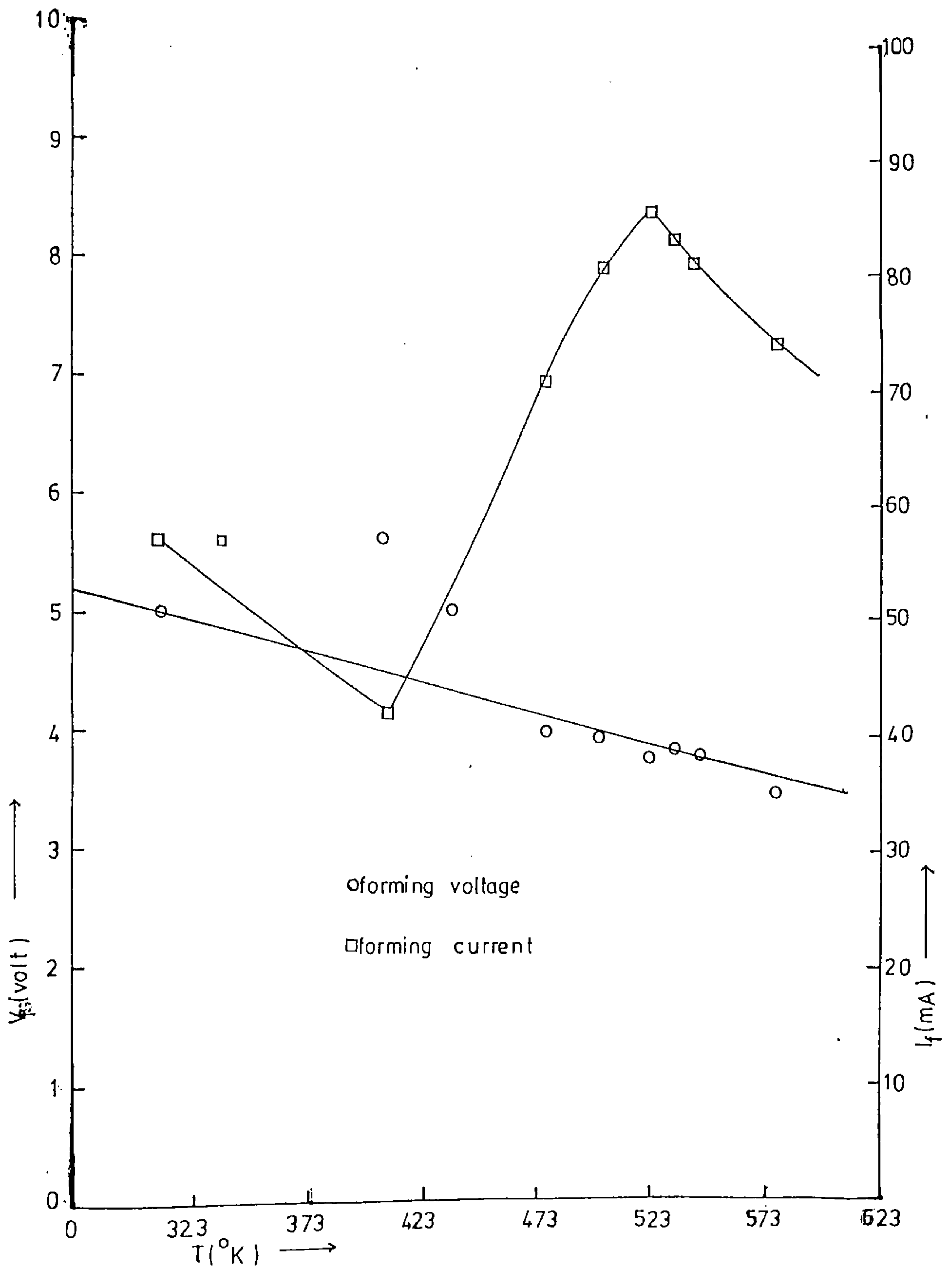

Fig.4.16. Variations of forming voltage V_f and current I_s with temperature of an Al-SiO-Cu sandwich structure with insulator thickness 5900Å.

The experimental results (Figs. 4.12 nd 4.15) were tested with the model expressed by the expressions (2.74) and (2.75). These are shown in Figs. 4.17-4.20.

Figs. 4.21-4.23 show the electrical switching measured at about 10^{-3} torr pressure and normal temperature in the Al-SiO-Cu/Al-V_2O_5-Cu/Al-V_2O_5-Al sandwich structures respectively. Figs. 4.21-4.22 show switching from "On" state to "off" state while Fig. 4.23 shows switching from "Off" state to "On" state. Appearance of switching can be explained in the following way using the same model. the reasons for appearing the switching "off" and "on" are due to rupture of filaments due to Joule heating effect and regrowth of filaments within the dead time.

Figs. 4.24 and 4.25 represent the emissions of electrons in the Al-SiO-Cu and Al-V_2O_5-Cu sandwich structures respectively. Emission from the surface of the devices will be due to the generation of hot carriers by the high electric fields which exist at high resistance spots of the filaments. It is possible in the case of a filament with a weak spot near to the anodes for electrons to be accelerated through a large potential difference just below the anode layer. Emitted electron energies to spread almost upto that corresponding to the full applied potential difference. One can further understand why electron emission should first be detectable near to the voltage V_F at which filaments begin to rupture.

4.1.4 Optical Measurements.

Optical measurements (UV, visible and Infrared) were made on SiO and V_2O_5 films of five different thicknesses. The principal

Fig.4.17

Fig.4.18

Fig.4.17 & 4.18. Represent both the experimental results and theoretical model. Solid represents experimental results and dotted line theoretical model.

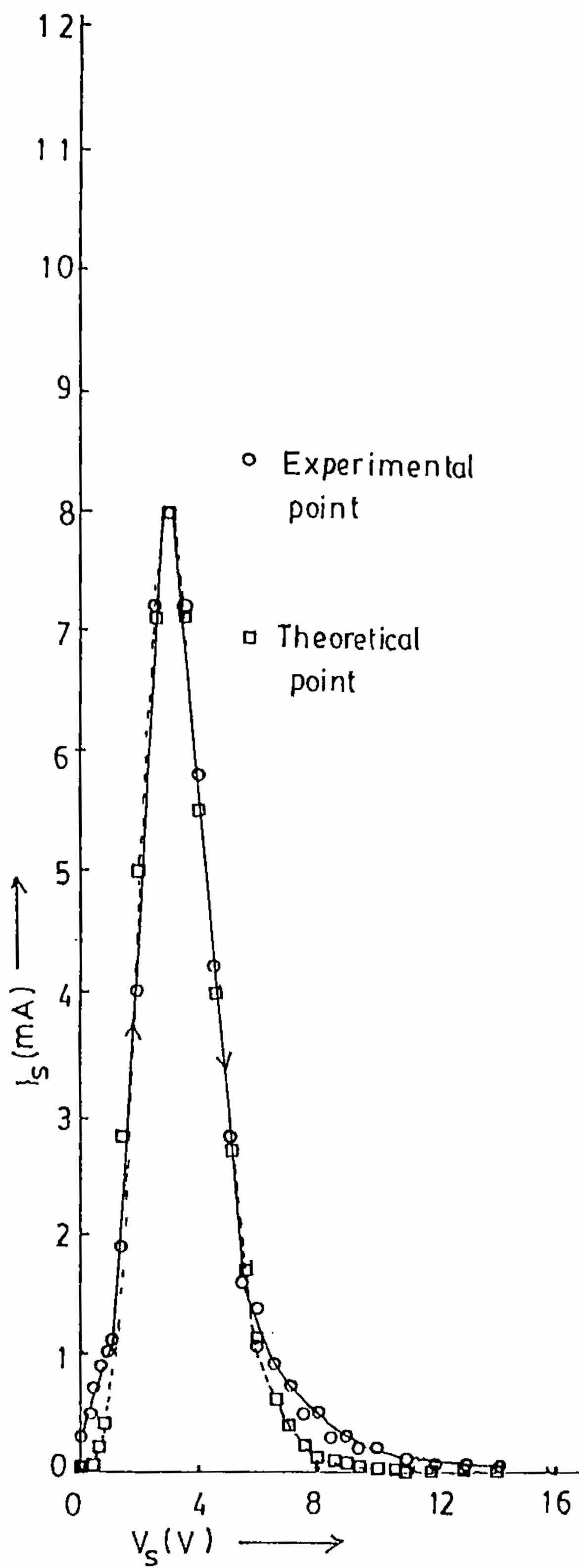

Fig.4.19

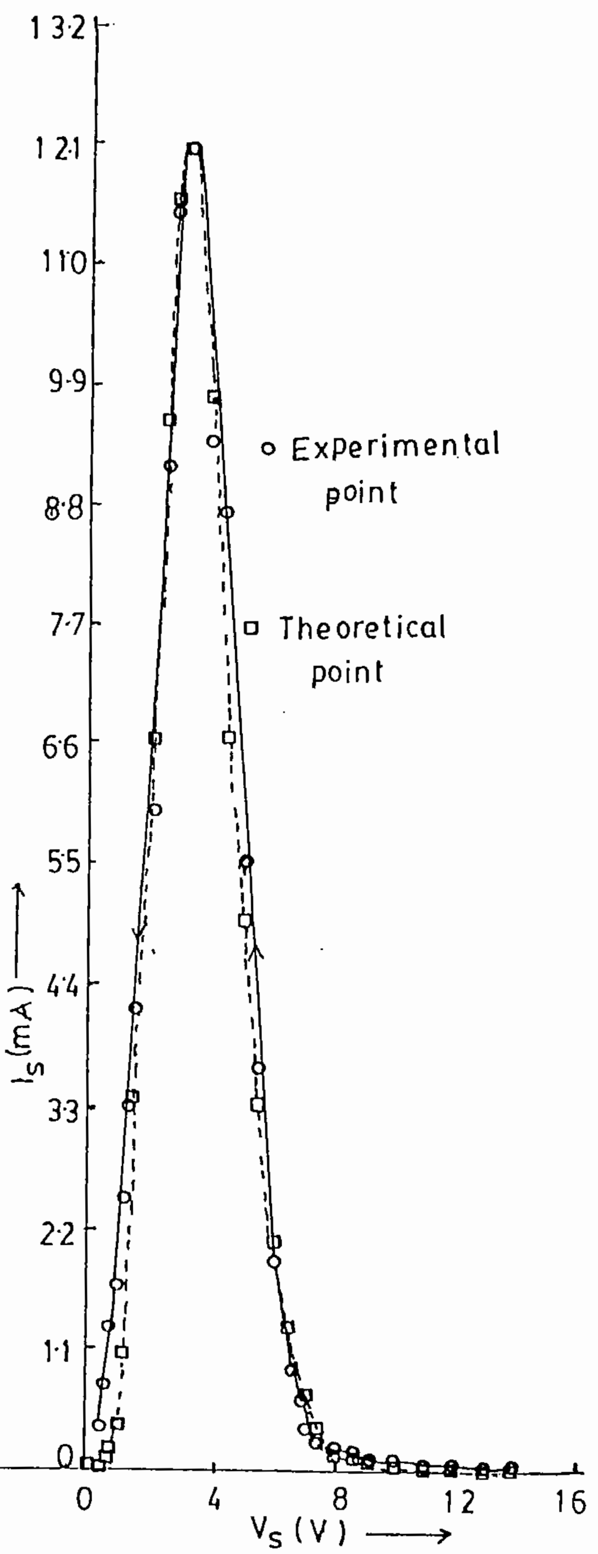

Fig.4.20

Fig.4.19 & 4.20 indicate the fitting curves of the curves of Fig.4.15.

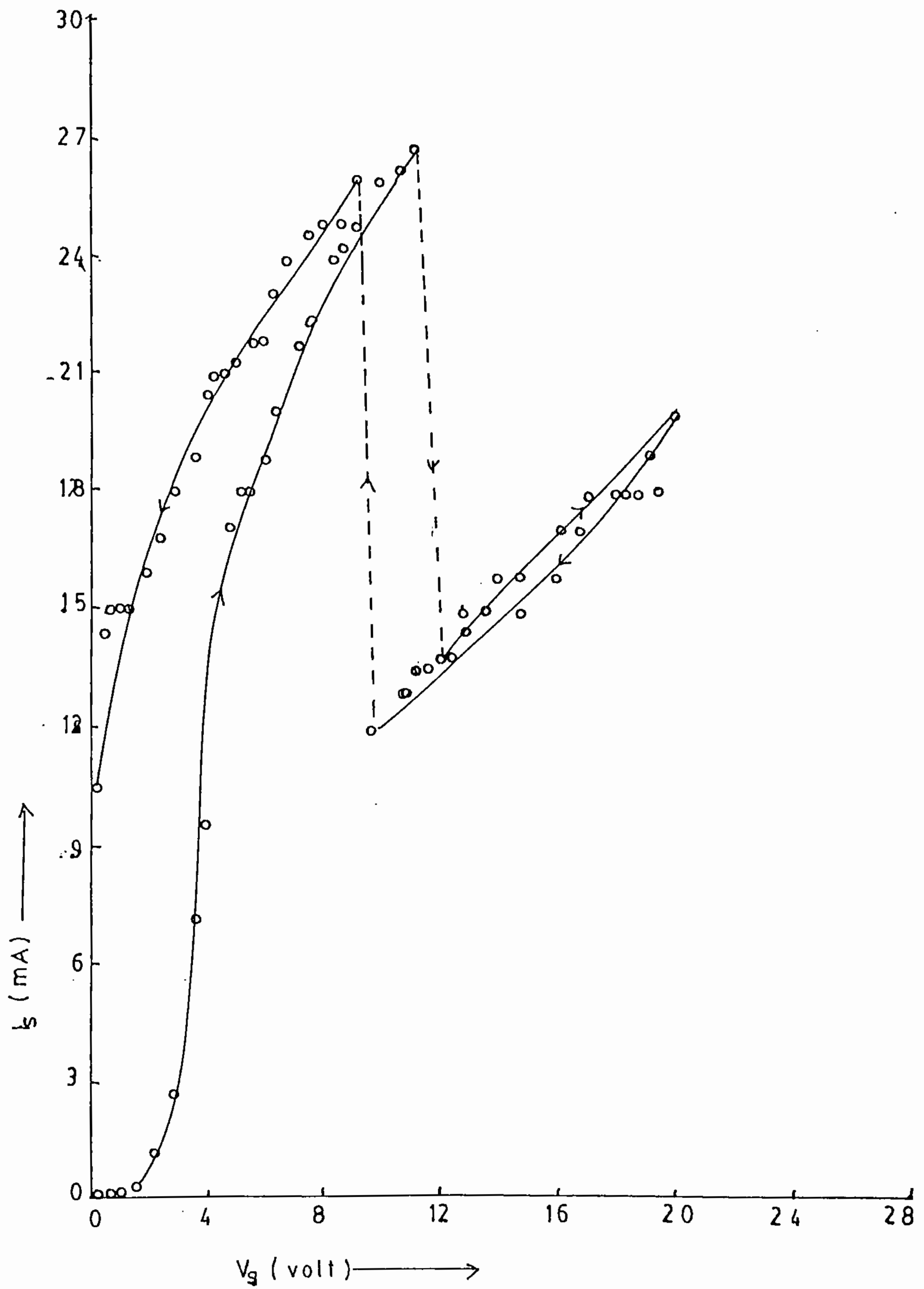

Fig.4.21. Switching I_s-V_s characteristics of an Al-SiO-Cu sandwich structure with insulator thickness 900Å.

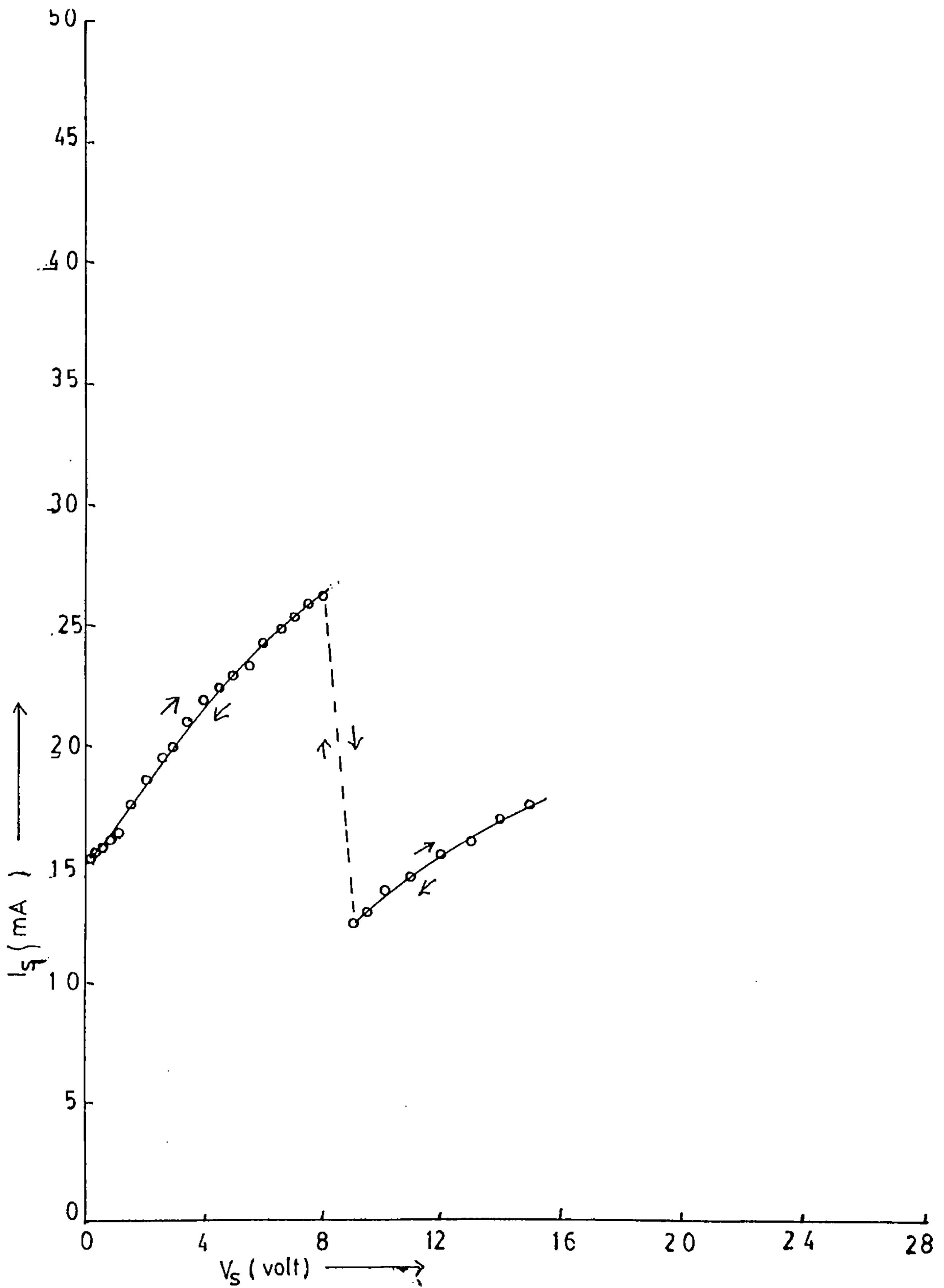

Fig.4.22. Switching characteristics of an Al-V_2O_5-Cu sandwich device with insulator thickness 1900Å.

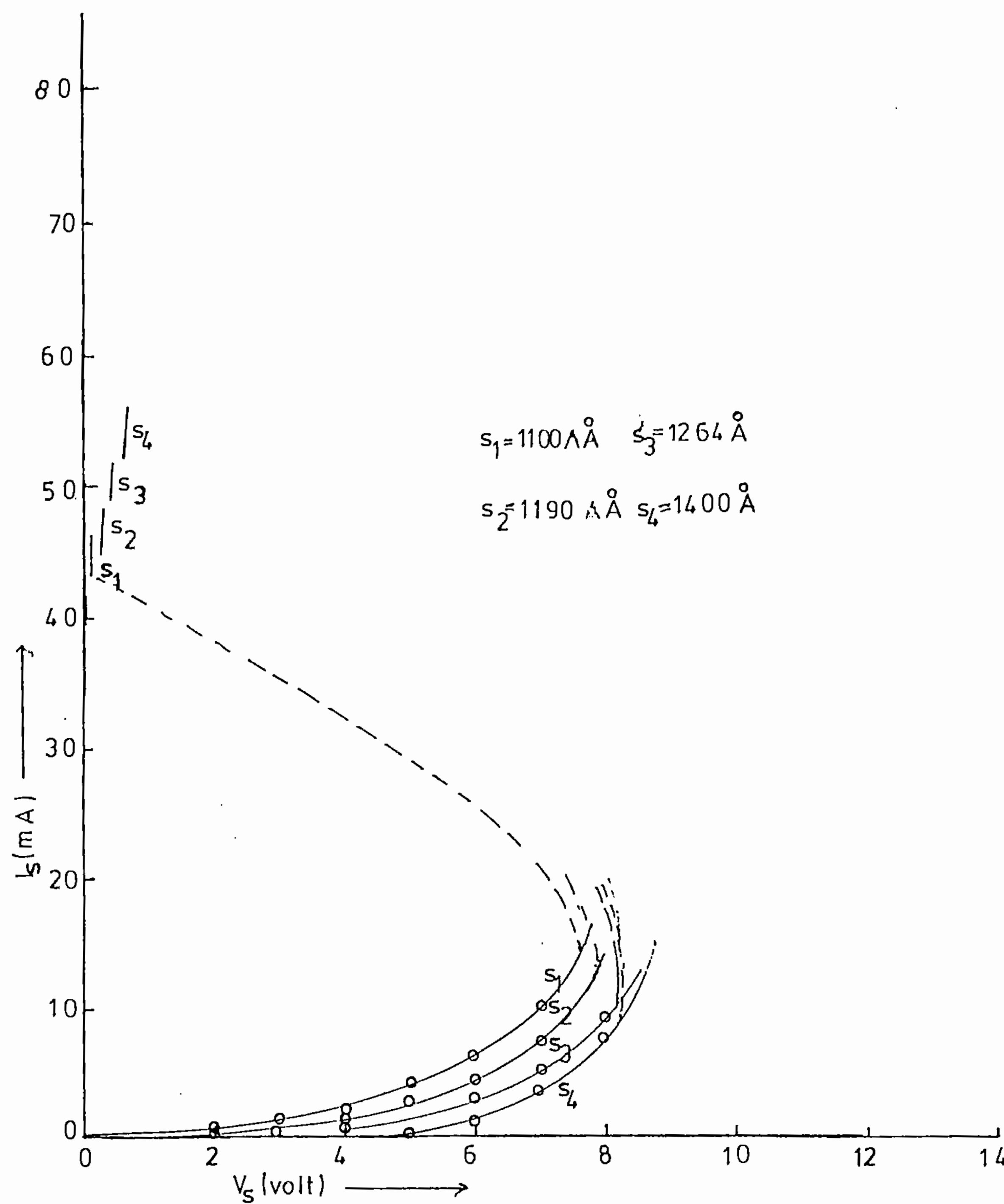

Fig.4.23. Switching I_s-V_s characteristics of Al-V_2O_5-Al sandwich structures with different insulator thicknesses.

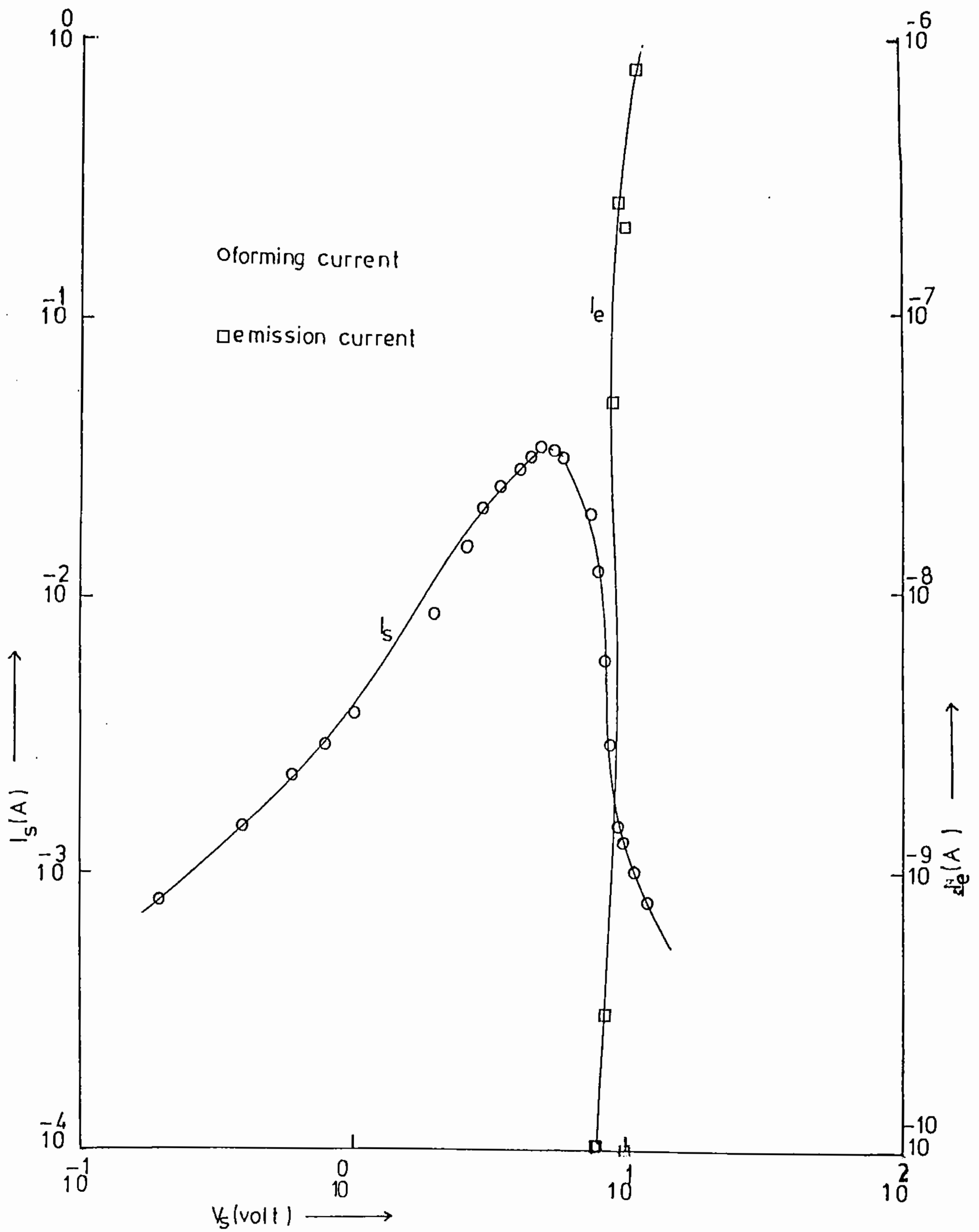

Fig.4.24. Electron emission of an Al-SiO-Cu sandwich device with insulator thickness 3700Å.

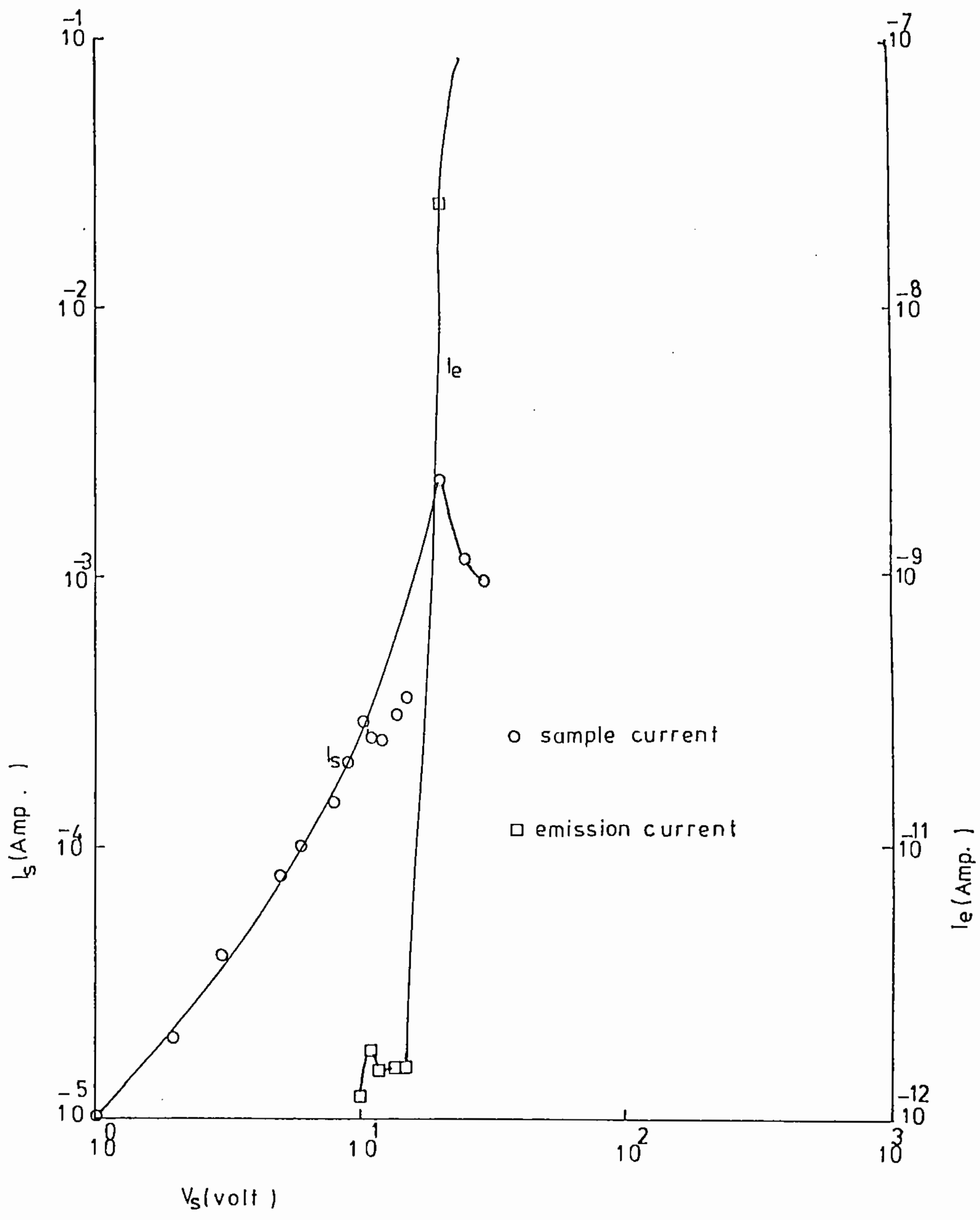

Fig.4.25. Electron emission of an Al-V_2O_5-Cu sandwich device with insulator thickness 2400Å.

objectives of this study were to obtain an estimate of the valence conduction band gap the extent of any band-tailing (from UV and Visible Measurements) the values of the refractive indices and to determine the presence and extent of absorption peaks (from IR measurements).

4.1.4.1 UV and Visible Measurements

The UV and visible absorption spectra for SiO and V_2O_5 films of different thickness are shown in Figs. 4.26(a) and (b). The values of the absorption coefficient α { = (2.303/d) log (1/T)} using transmission coefficient T in the straight portions of the graphs in the short wavelength region of the spectra (Figs.4.26(a) nd (b)] were calculated. The graphs of $[\alpha(w)\ w)^{1/2}$ versus w were plotted [Figs.4.26(a) and (b)]. The graphs of $[\alpha(w)\ w)^{1/2}$ versus w have well defined linear regions conforming the relation

$\alpha hw = B\ (w-E_{opt})^2$ . . . . (4)

where $\alpha(w)$ is absorption coefficient, w is the photon frequency. E_{apt} is the optical bandgap energy and B is a constant equal to $4\pi\delta^0/cnE_e$, here δ^0 is the electrical conductivity extrapolated to absolute zero, E_e is the width of the tails of localized states in the bandgap region n is the refractive index and c is the speed of light. The values of E_{opt} found from Figs. 4.27(a) and (b) are in the range 1.90-2.10 ev for SiO films and 1.30-1.80 ev for V_2O_5 films respectively.'

The band tailing E_e was obtained from the urbach rule; $\alpha(w)$

$\alpha_o exp\ (hw/e_e)$ . . . . (5)

Graphs of Figs. 4.28(a) and (b) represent In α versus w plots for

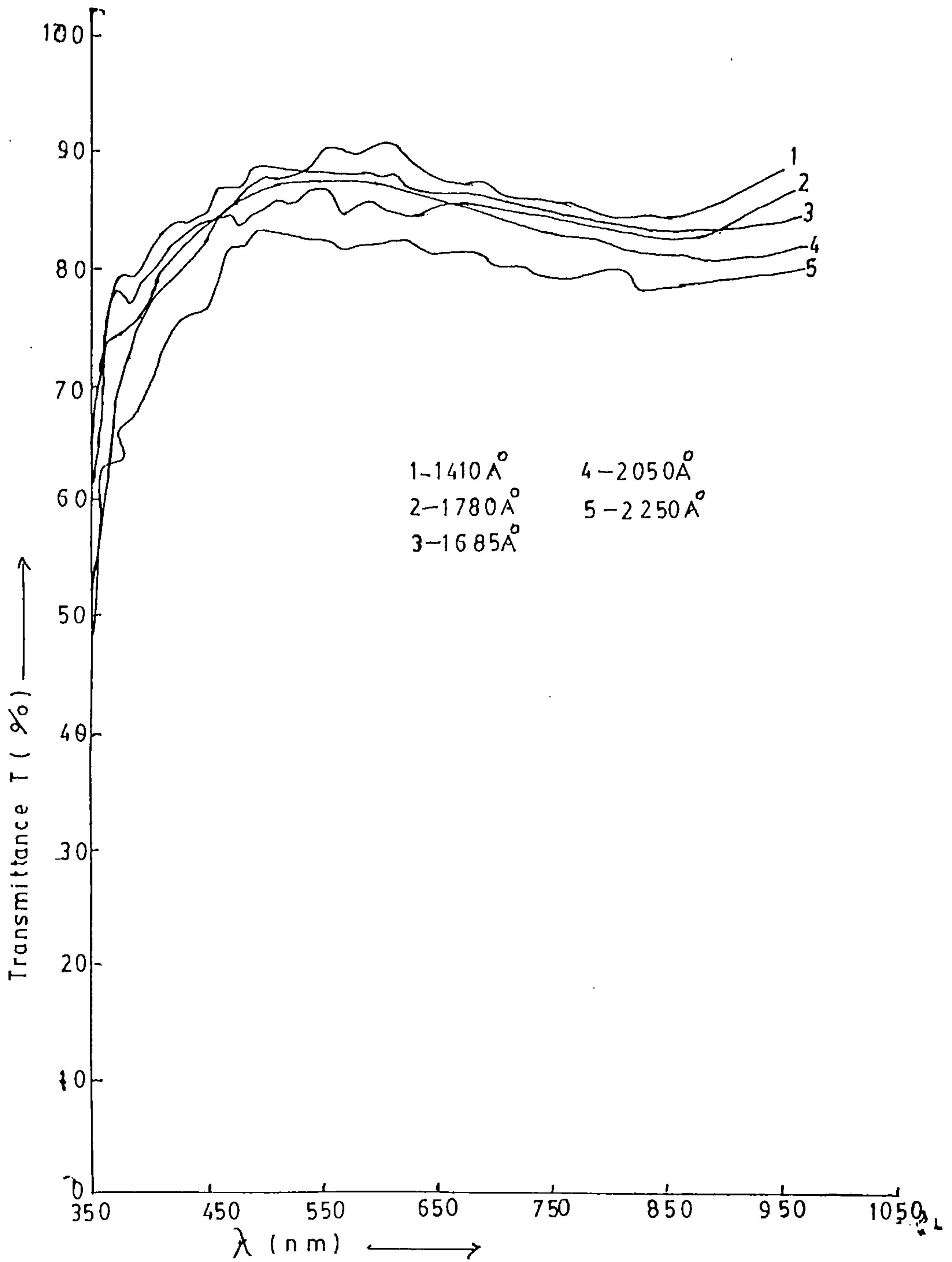

Fig.4.26(a). T-λ curves of five SiO films of different thicknesses.

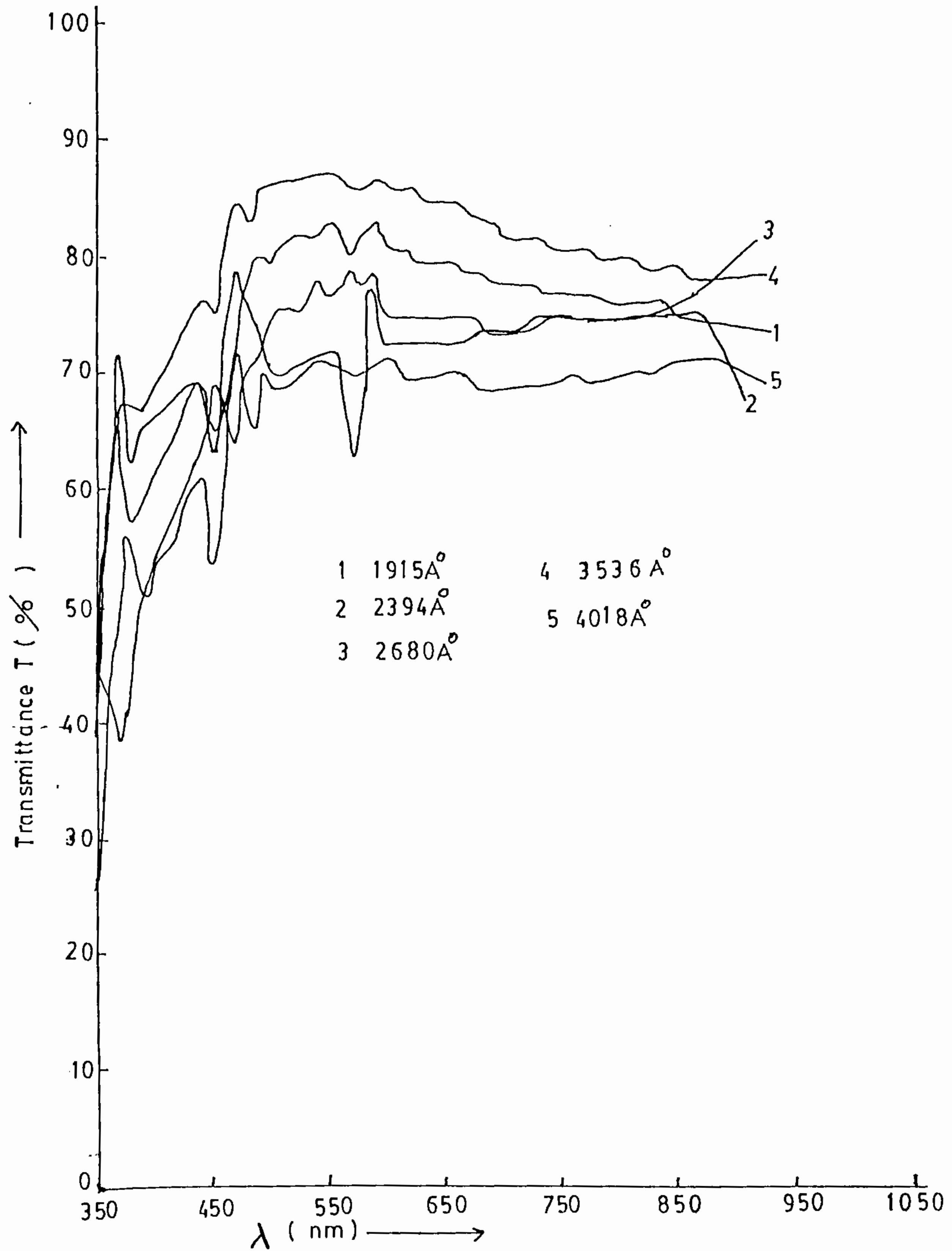

Fig.4.26(b). T-λ curves of five V_2O_5 films of different thicknesses.

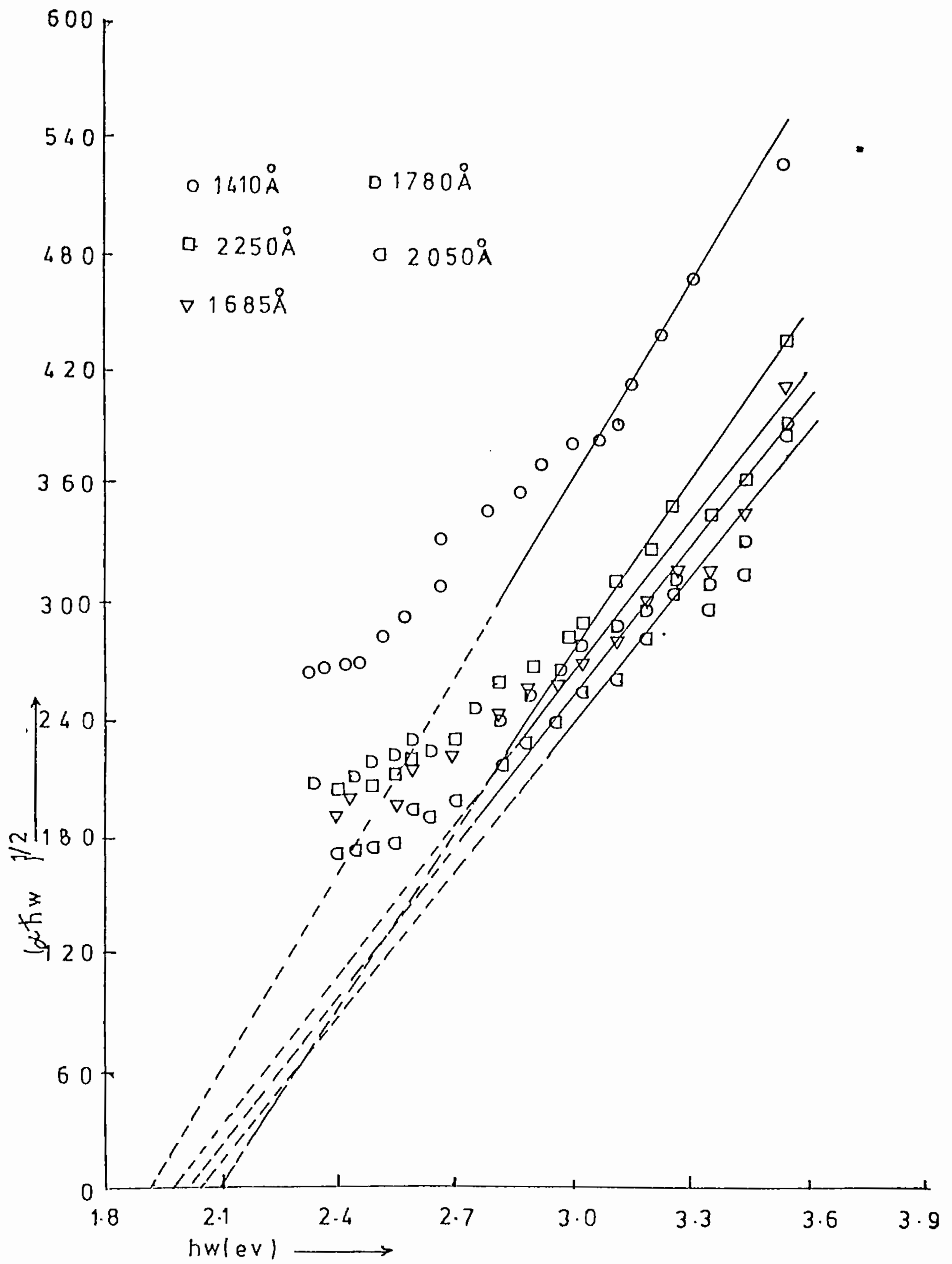

Fig.4.27(a). $(\alpha \hbar w)^{1/2} \sim \hbar w$ curves of SiO films.

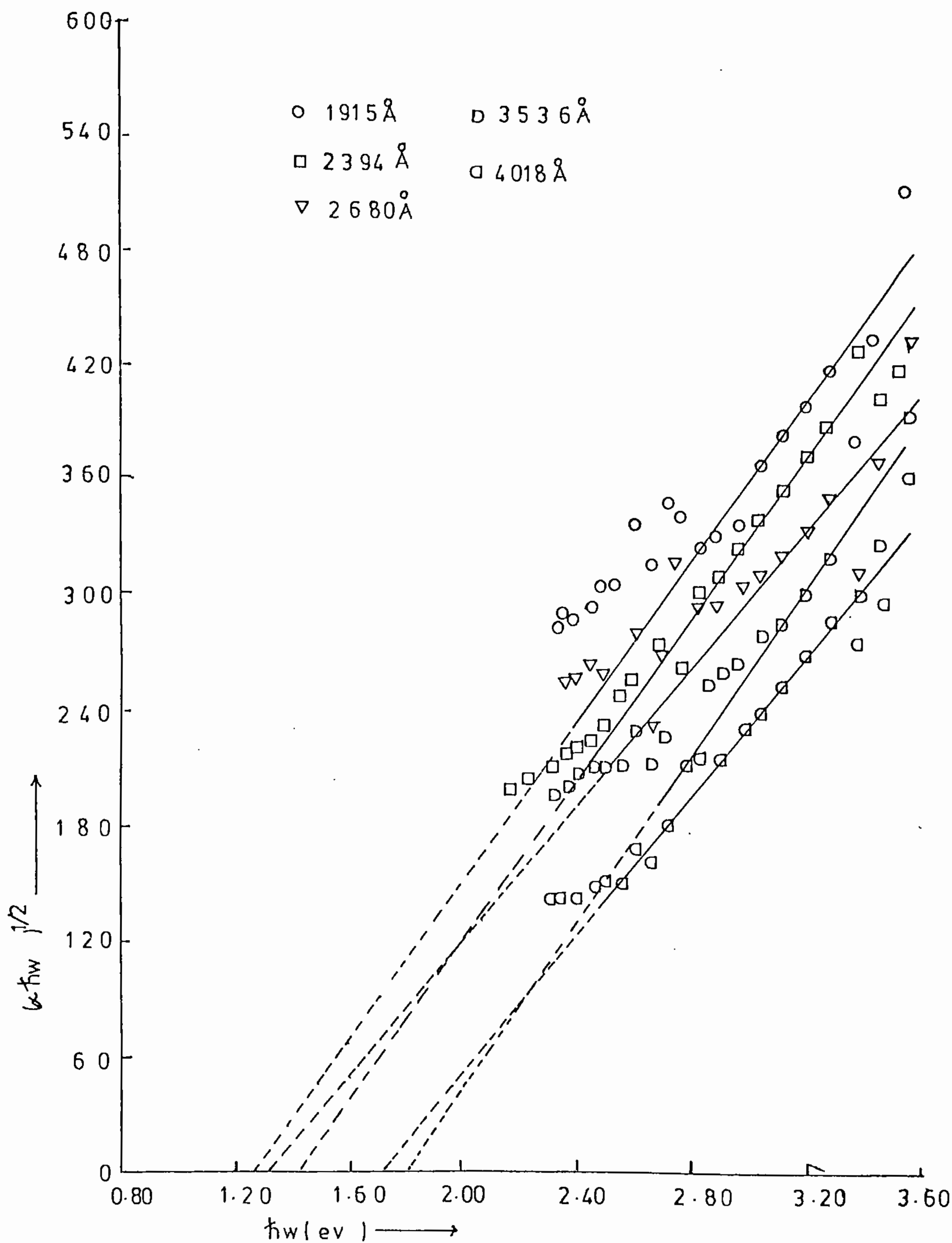

Fig.4.27(b). $(\alpha\hbar w)^{1/2} \sim \hbar w$ curves of V_2O_5 films.

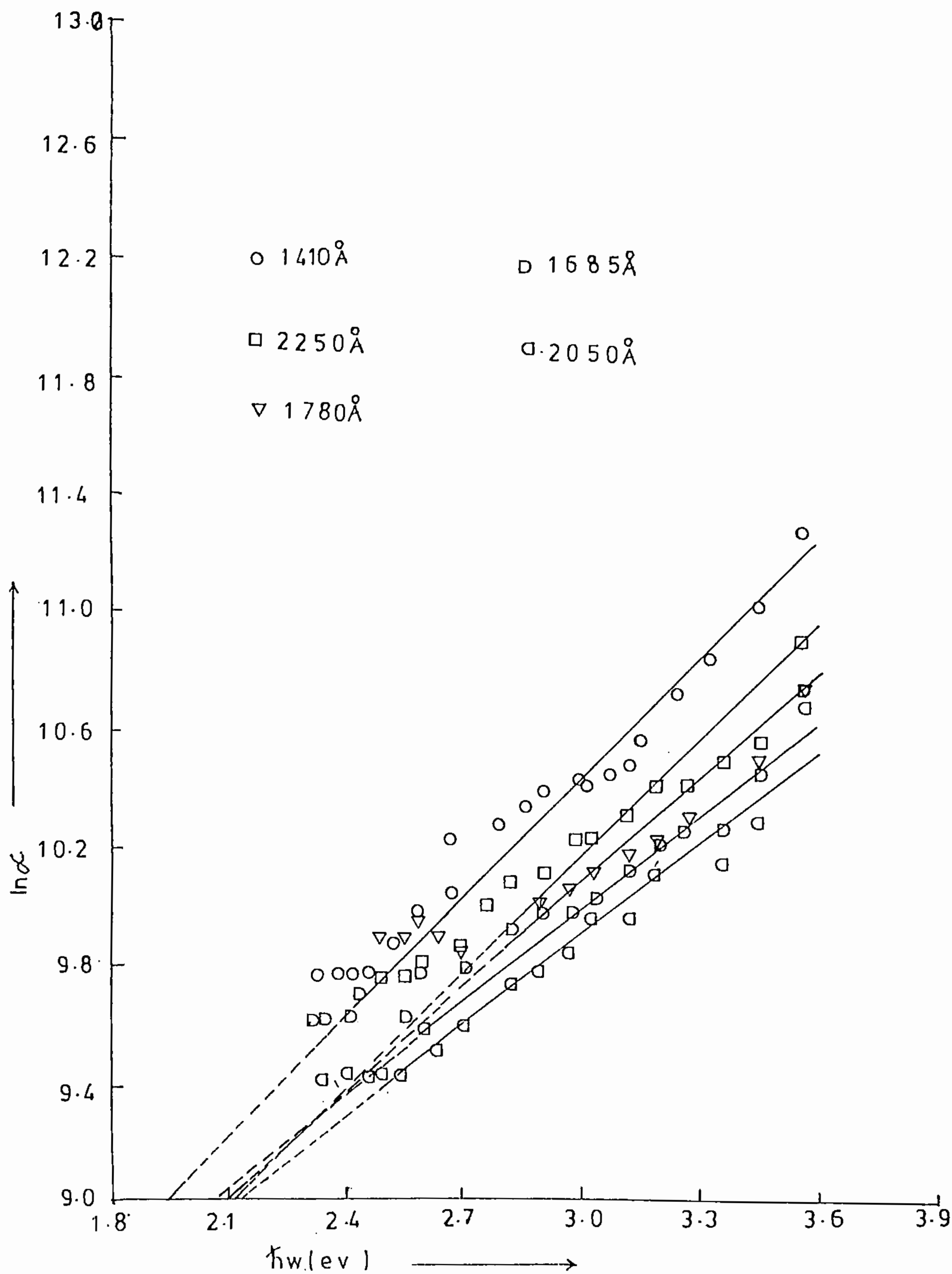

Fig.4.28(a). Inα~ħw curves of SiO films.

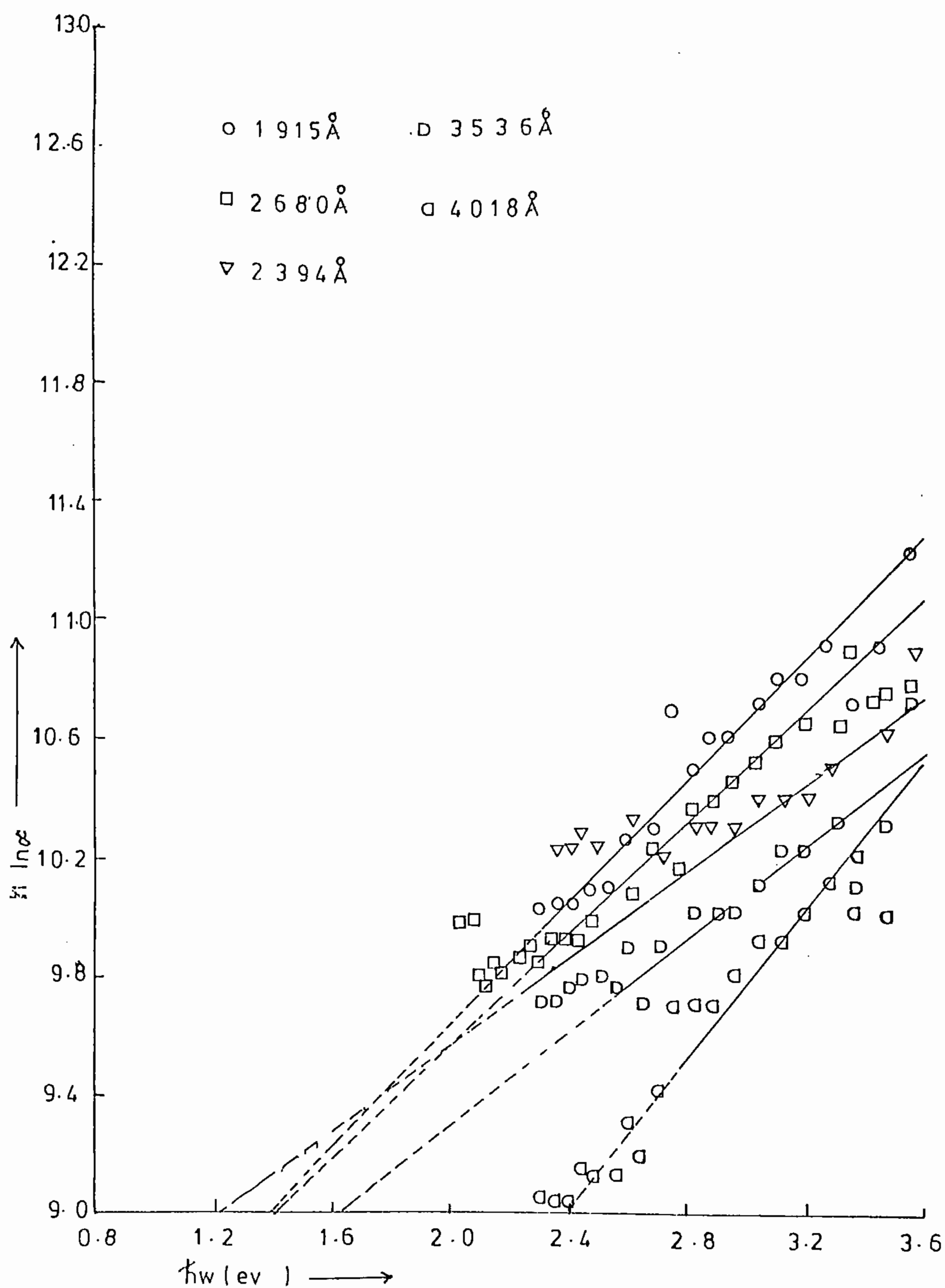

Fig.4.28(b). Inα ~ $\hbar w$ curves of V_2O_5 films.

SiO and V_2O_5 films respectively.

The values of band tailing E_e from graphs of Figs. 4.27(a) and (b) were found in the ranges 0.20-0.24eV and 0.13-0.27 eV for SiO and V_2O_5 films respectively.

Fig.4.29 represents the spectra of glass (graph 1) SiO (graph 2) and V_2O_5 (graph 3) respectively. In this figure, the dotted lines represent the average transmission spectra of SiO and V_2O_5 films. Taking average values of T from Fig.4.29 values of the refractive indices were calculated using following two relations.

$$T = \frac{16n^2 n_0 \eta}{(\eta+1)^3 (n+n_0)-(n-1)^3 (n_{02}^{t}-n) \eta^2+2 (-1)^m (n^2-1) (n^2{}_0-n^2)} \quad \text{.. (6)}$$

This relation was set by Michailovits *et al.* (74)..

$$T = \frac{16n^2 n_0 \eta (1+k^2)^3}{\{[n_0+n (1-k^2)]^2 + K^2[n_0+2n]^2\} \{[(1+n(1-k^2)]^2+K^2(1+2n)^2\}} \quad \text{.. (7)}$$

This relation was set by us.

Where n_o is the refractive index of glass and the values of n_0 were calculated from the relation

$$T = \frac{2n_0}{\eta^2{}_0+1} \quad \text{. . . . . (8)}$$

$$\eta = \exp (4\pi kd/\lambda) \quad \text{. . . . . (9)}$$

n is the refractive index of the material, T is the transmission coefficient of the material, T_0 is the transmission coefficient of

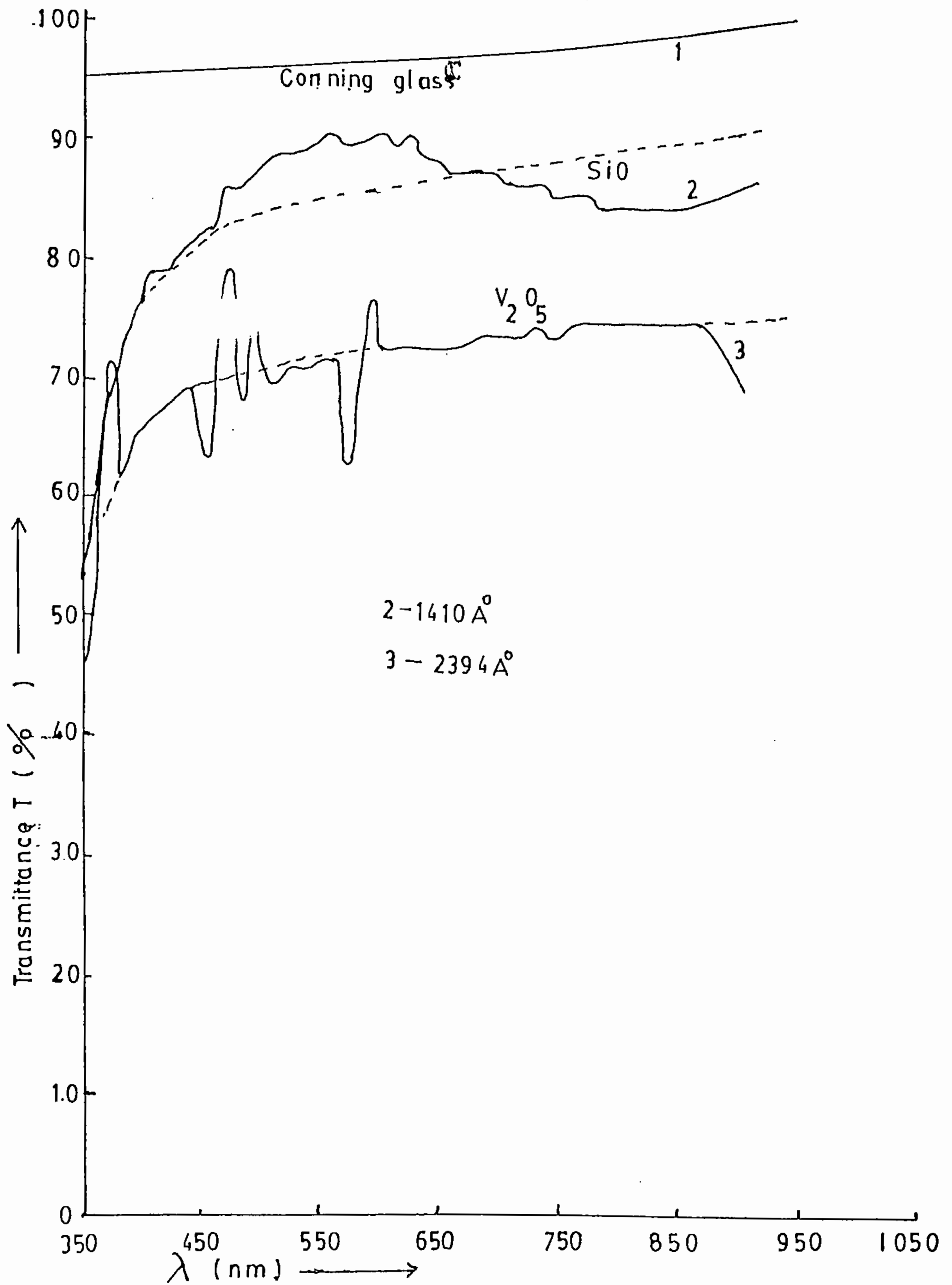

Fig.4.29. Average curves of SiO and V_2O_5 films.

glass, γ is the wavelength of light, d is the film thickness, K ($\approx$0) is the attenuation constant, η is the absorption coefficient and "m" is an index which may assume odd or even numerical values. Using expressions (6) and (7), values of η for given values of T, T_0, n_0, K, η were calculated by trial and error method. Error of calculation was limited within 2%.

Figs. 4.30(a) and 4.30(b) represent the variations of refractive indices with wavelength for SiO and V_2O_5 films respectively. In both the figures graphs (a) and (b) represent the variations of refractive indices calculated using (6) and (7) expressions respectively. The refractive indices as seen from the figures lie in the ranges 1.85-2.80 for SiO and 2.35-3.60 for V_2O films respectively in the 350-900nm light wavelength range.

4.1.4.2 Infrared (IR) Measurements.

Figs. 4.31(a) and (b) show the variations of transmission coefficients of SiO and V_2O_5 films respectively with wavelength in the IR regions of wavelength spectrum. Fig. 4.31(a) indicates that there is a strong absorption peak at 10μm (1000 cm^{-1}) wavelength and from Fig. 4.31(b) we see that there are two absorption peaks, one at 6.9 μm (1620 cm^{-1}) wavelength and the other at 10μm (1000 cm^{-1}) wavelength.

Since more than 30 years (80) IR spectroscopy has been an established technique both for measuring the interstitial oxygen concentration in crystalline silicon and for determining the position of the oxygen atoms in the silicon lattice. This method is equally applicable for determining oxygen concentration in vanodium

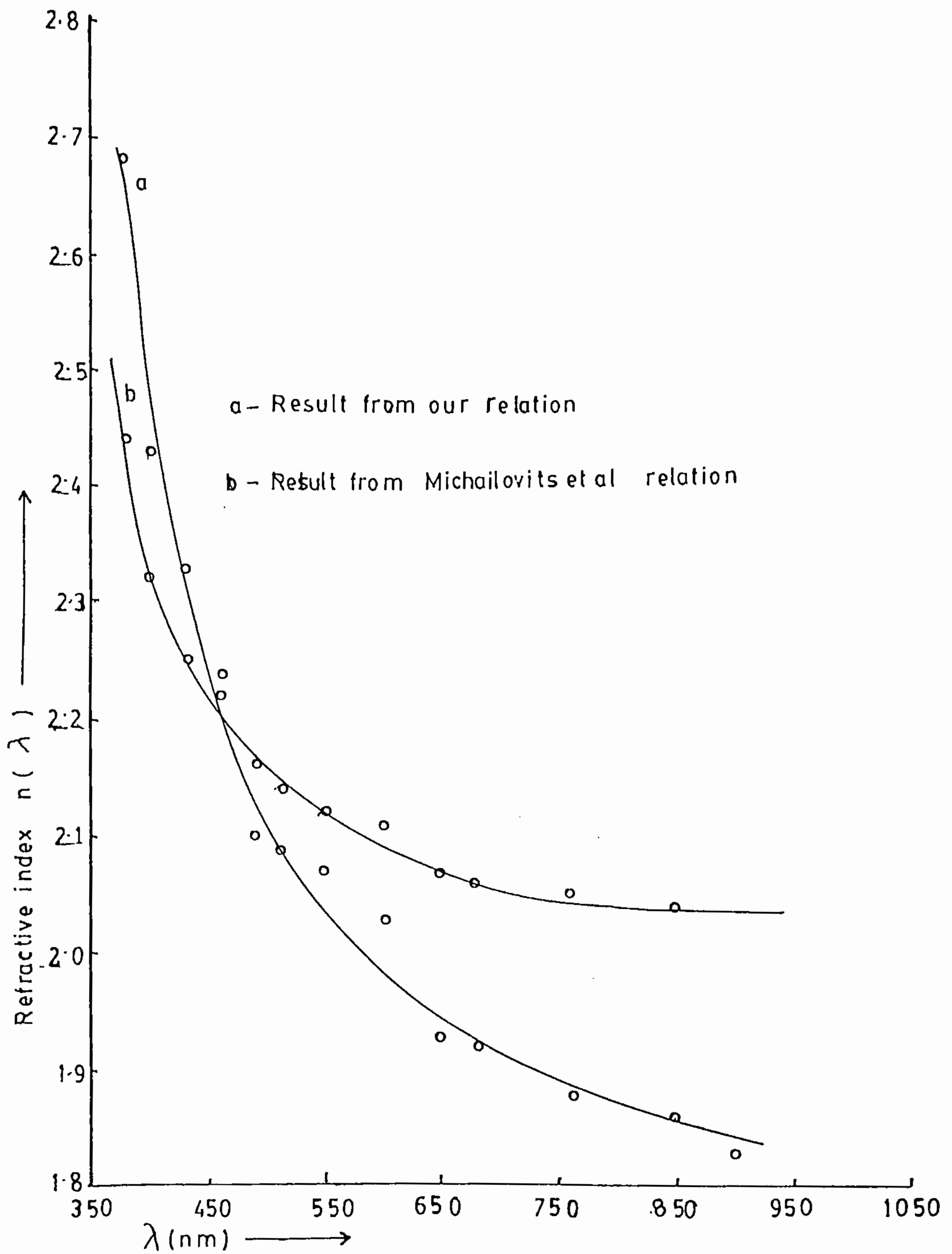

Fig.4.30(a). n–λ curves of a SiO filt.

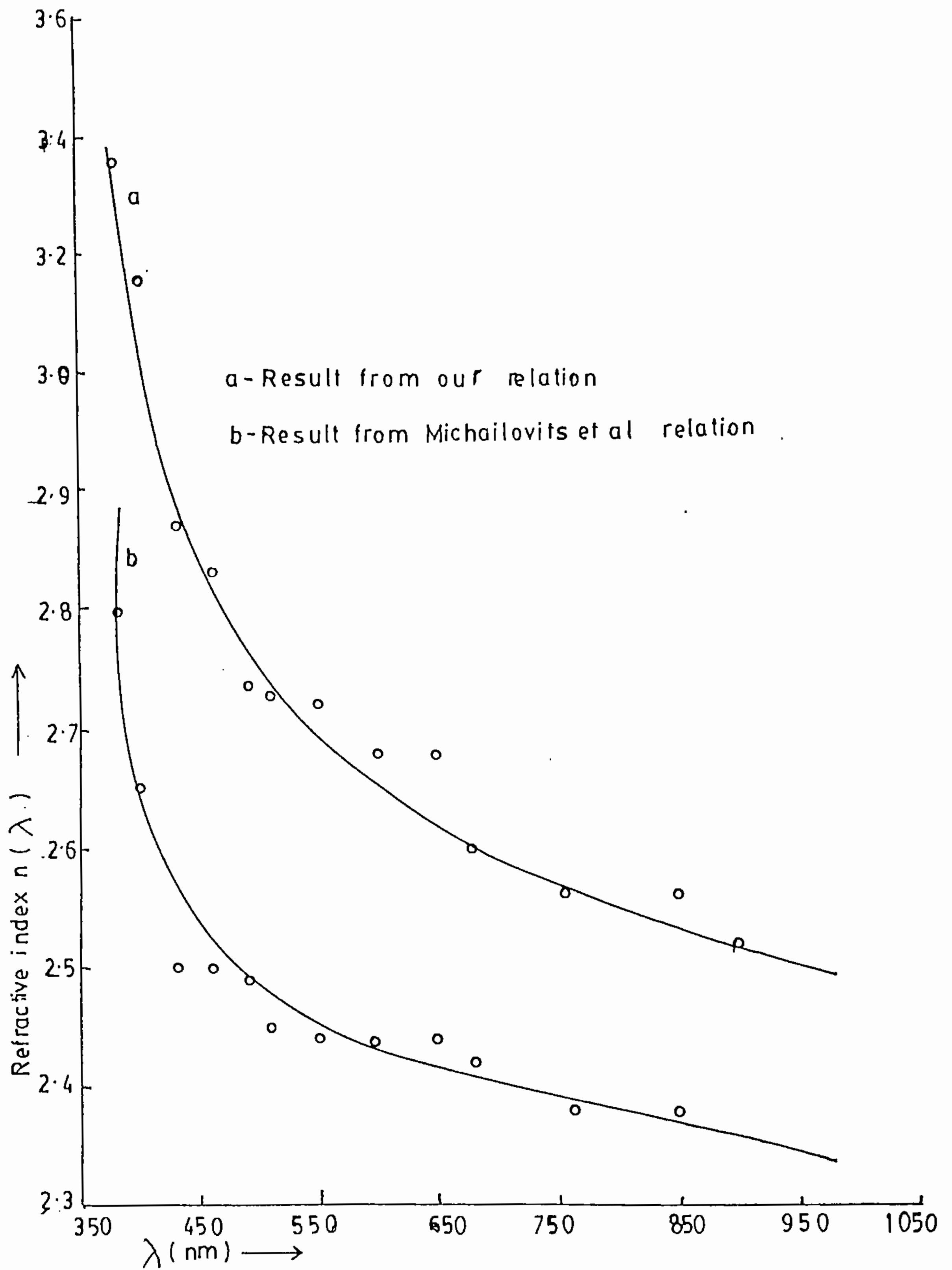

Fig.4.30(b). n-λ curves of a V_2O_5 film.

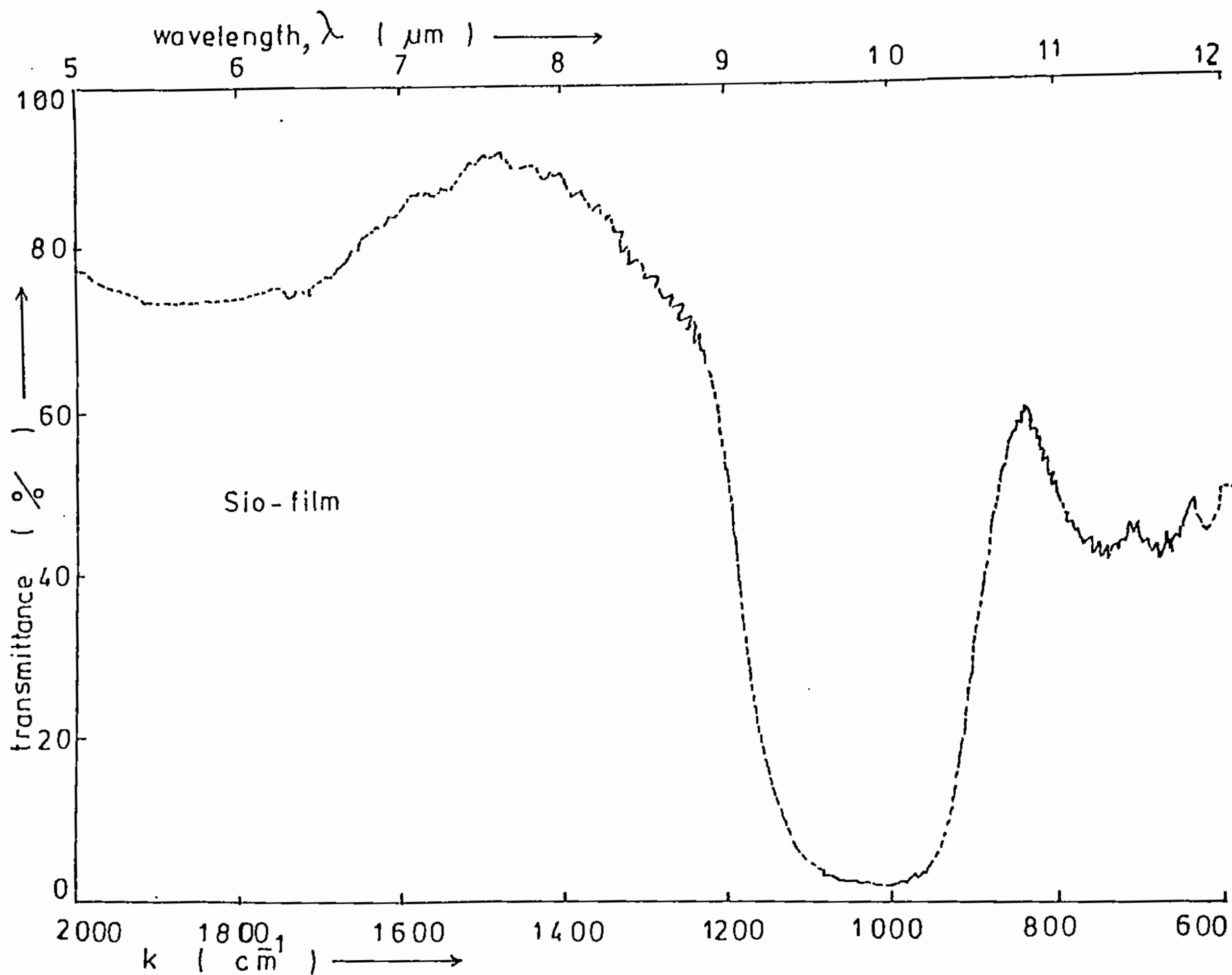

Fig.4.31(a). IR T-λ spectrum of a SiO film.

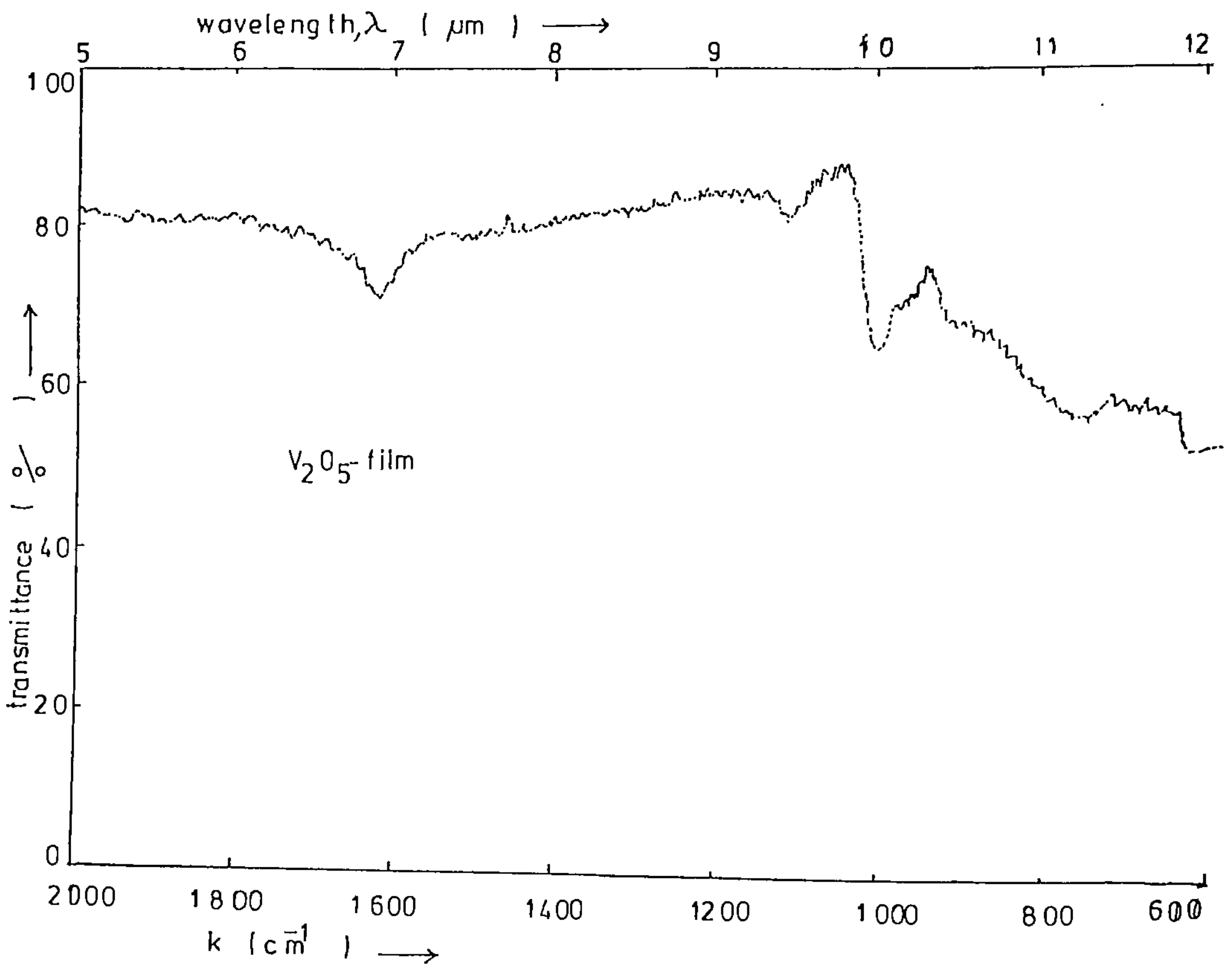

Fig.4.31(b). IR T-λ spectrum of a V_2O_5 film.

and for indicating oxygen position in the vanadium lattice.

Bond length [Si-O-Si) of pure SiO is 10μm (1000 cm^{-1}). Vandiumn pentoxide (V_2O_5) is a mixture of two compounds such aa Vanadium dioxide and vanadium trioxide. The bond lengths of VO_3 (V-O) and VO_2 (V-O) are 6.9 μm and 10 μm respectively.

Shabalov *et al.* (69) has been suggested that for the IR spectra the absorption peak could be shifted towards the higher frequency region by increasing oxygen concentration in the dielectric materials. Alternatively analysis of the IR spectra shows that the shift in the bond stretching modes into the region of low frequency spectra with a decrease in the oxygen concentration in the films due to the increase in the length of the dielectric material. So the oxygen concentration in VO_3 is greater than that in VO_2.

4.1.4.3 Proposed Electronic Band structure of SiO

Combining the information of DC meassurements. UV and visible measurements it is possible to draw an electronic band structure of SiO. It may be seen from Table 3 that the room temperature DC activation energy for electrical conduction varies from 01. to 0.2eV. From Tables 9 and 10 we see that the optical band gap energy is 2eV. Thus the activation energy is much smaller than the optical band gap energy. The mobility gap is 4eV. In SiO an unsatisfied silicon bond which is in total or partial coordination with oxigen (Si-O-Si) is more likely to form a donor centre responsible for Poole-Frenkel emission. The donor level is about 0.2eV below the conduction band of SiO as shown in Fig. 4.32.

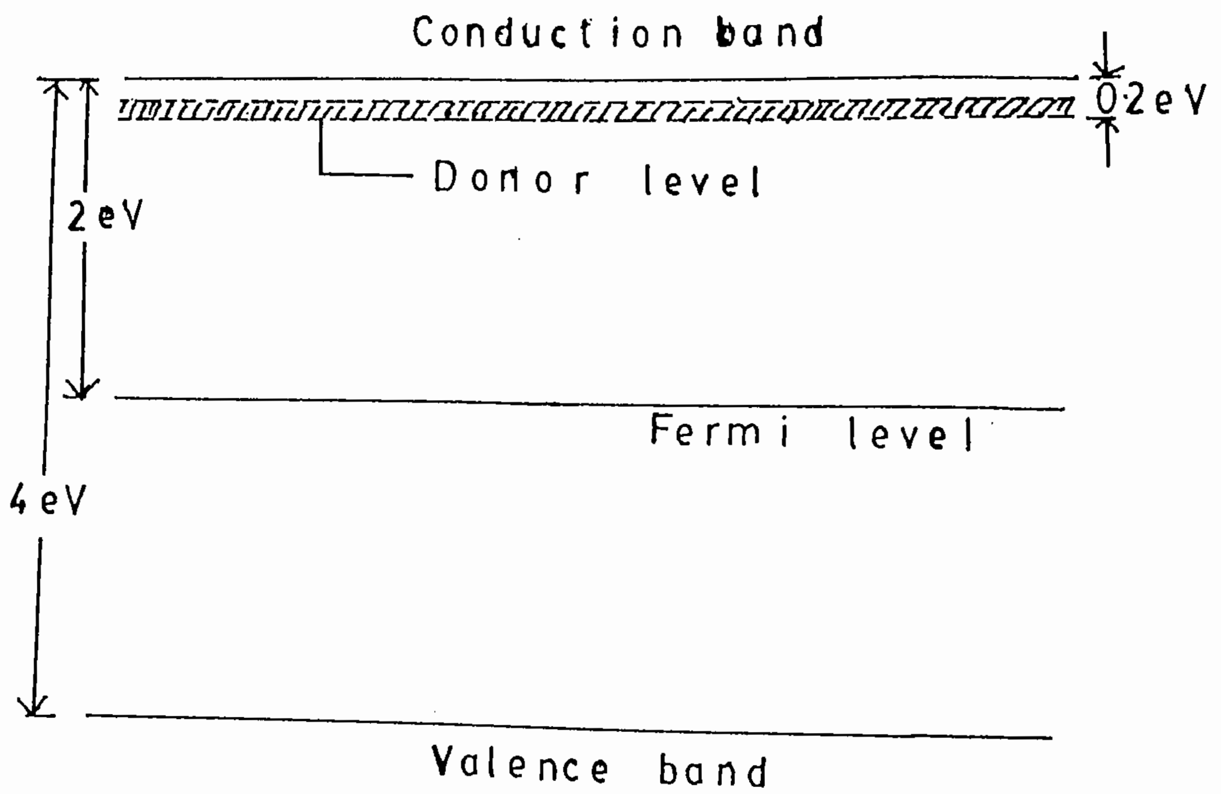

Fig.4.32. Possible energy band diagram for SiO-films.

Table-9 SiO film

Film thickness(Å)	Optical Band gap Energy E_g (eV)	Band tailing E_e (eV)
2200	2.09	1.06
2000	2.04	1.30
1800	2.01	1.17
1600	1.97	1.30
1400	1.90	0.93

Table 10. V_2O_5 - films

Film thickness(Å)	Optical Band gap Energy E_g (eV)	Band tailing E_e (eV)
4000	2.12	1.10
3500	2.16	0.90
2700	1.96	1.09
2400	2.16	0.70
1900	1.84	1.00

4.1.4.4 X-ray Diffraction Study

Figures 4.33 and 4.34 indicate x-ray diffraction pattern of SiO and V_2O_5 thin films respectively. It is seen from these spectra that SiO and V_2O_5 materials are amorphous in structure.

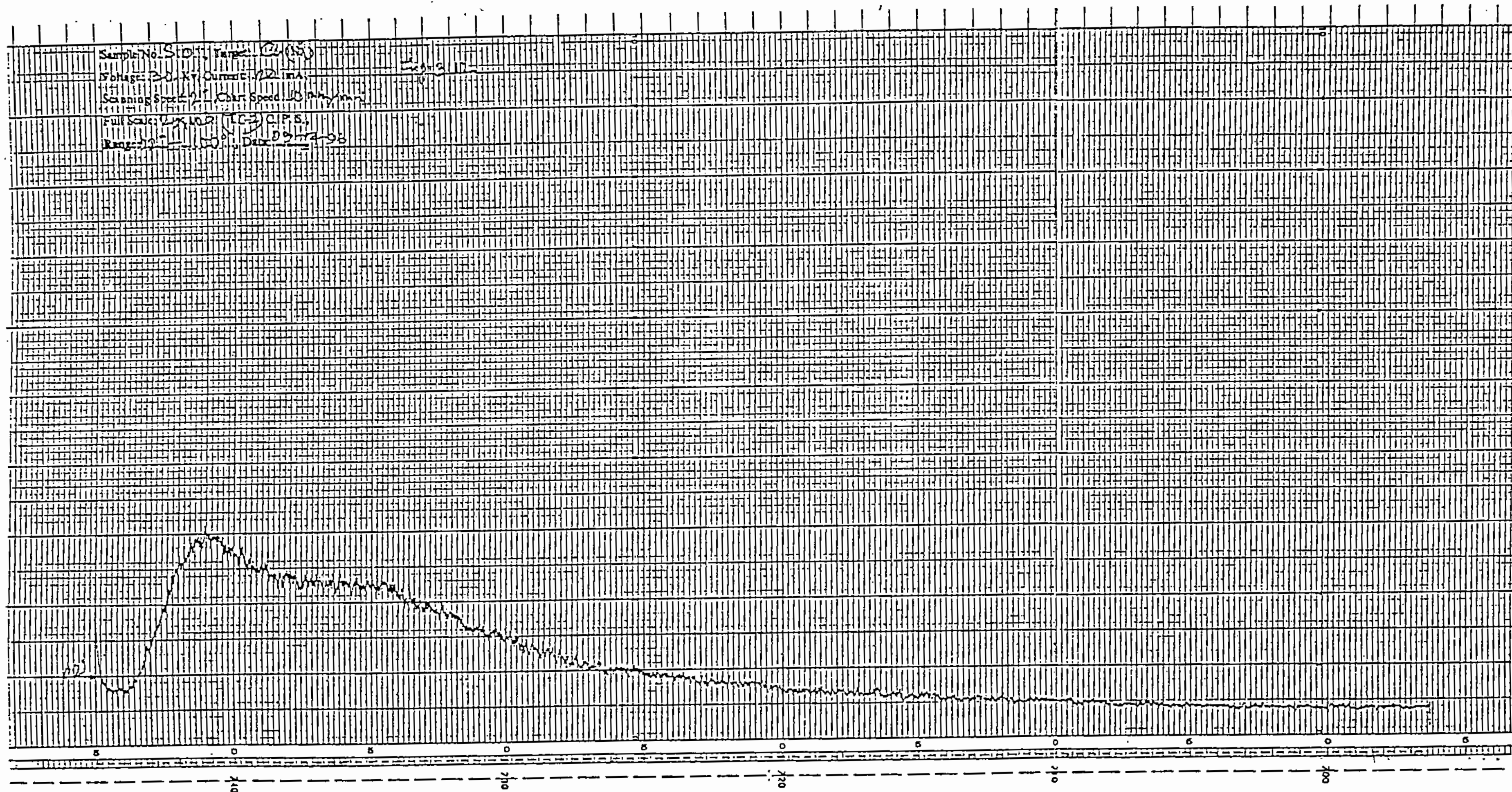

Fig.4.33. X-ray diffraction pattern of SiO thin film of thickness 3000Å.

CHAPTER V

CONCLUSION AND SUGGESTIONS FOR FURTHER RESEARCH.

In the light of the experimental investigations and their analyses (Chapter IV) the following conclusions may be drawn:

1. Optical measurements (UV and visible) provide the information of optical band gap. This band gap energy helps to construct the electronic band structure of the materials SiO and V_2O_5 .

Infrared measurements carried on SiO and V_2O_5 thin films have provided us with absorption peaks - One at 10 μm (1000 cm^{-1}) wavelength for a SiO film and the other at 6.9 μm (1620 cm^{-1}) and 10 μm (1100 cm^{-1}) wavelengths for a V_2O_5 film. This confirms purity of the materials (SiO and V_2O_5).

2. The non-ohmic behaviour of unformed and pre-formed devices of the insulators can be explained by the normal Poole-Frenkel models based on localized conduction. Thermal activation energies were determined. The origin of the DC activation energy at present is not known. This would be a future research work. Determination of the thermoelectric power of SiO and V_2O_5 films is the most direct way of finding out whether the mobility contains an activation energy either due to polarons or to disorder. If the activation energy deduced from the conductivity is greater than that deduced from the thermopower, polaron hopping would be occurring otherwise electronic hopping. This is another aspect for future research work.

3. A monotonic increase of conductance with frequency was observed in the AC measurements of unformed and pre-formed devices. It is suggested that multiphonon hopping conduction is occurring in these devices at all temperatures.

AC measurements may be extended to formed devices. The metallic nature of the filaments may be tested by measuring their conductance and capacitance.

4. Electroforming was observed in Al-SiO-Cu sandwich structures. VCNR, electronic switching and electron emission were explained by employing modified model of Ray and Hogarth. Electron emission may be studied further as a function of device temperature.

References

1. G.S. Kreynina, L.N. Selivanov and T.I. Shumskaya, Radio. Eng. Electron (USR), 5(1960) 219.
2. T.W. Hcikmott, *J. Appl.* Phys. 3 (1962) 2669.
3. J.G. Simmons and R.R. Verdeber, *Proc. Roy. Soc.* A-77 (1967) 102.
4. R.R. Verderber, J.G. Simmons and B. Eales. *Philosophical Magazine*, 16(1967) 1049-1061.
5. G. Dearnaley, D.V. Morgan and A.M. stoneham, Non-crystalline solids, 4 (1970) 593-613.
6. H. Biederman, Vacuum, 26 (1976) 513-522.
7. R.D. Could, Paper presented at the Fourth Internaitonal Congress on Thin Films, Loughborough Grt. Britain, September 11-15, 1978.
8. P.D. Greene, E.L. Bush and I.R. Rawlings. The symposium on deposited thin dielectrics, Montreal, p-167, 1969.
9. A.E. Rakshani. C.A. Hogarth and A.A. Abidi, *Journal of Non-crystalline solids, 20 (1976) 25-42.*
10. J.E. Ralph and J.M. Woodcock, Journal of Nona-Crystalline Solids, 7 (1972) 236-250.
11. H. Araki and T., Hanawa, Thin Solid Films, 152 (1987) 481-486.
12. J. Beynon, A.K. Ray, A.R. Sankar, Journal of Materials Science Letters. 5 (1986) 1156-1158.
13. R.F. Thurstans, Thin Solid Films, 57 (1979) 153-156.
14. H. Araki and T. Hanawa, Thin Solid Films, 121 (1984) 17-27.

15. S.M. Patel and N.G. Patel, Thin Solid Films, 113 (1984) 185-188.

16. F.A.S. Al-Ramadhan and C.A. Hogarth, *Journal of Materials Sciencem*, 19 (1984) 1718-1725.

17. A.G. Abdullayev, F.D. Kasimov, V.A. Vetkhov and V.M. Mamikonova, Thin Solid Films, 112 (1984) 121-125.

18. F.A.S. Al-Ramadhan. C.A. Hogarth and K.I. Arshak. International Journal of Electronics, 57 (1987) 227-238.

19. P.C. Lacaze, J.E. Dubois and G. Tourillon. Thin Solid Films, 66 (1980) 159-170.

20. K.I. Arshak, A. Glot, C.A. Hogarth, *Journal of Materials Science*, 20 (1985) 3590-3596.

21. H. Pagnia, N. Sotnik and W. Wirth, International Journal of Electronics, 69 (1990) 25-32.

22. Z. Hajek, I. Emmer and M. ohlidal, *International Journal of Electronics*, 69 (1990) 43-47.

23. Ludmilla Eckertova, *International Journal of Electronics*, 69 (1990) 65-78.

24. H. Pagnia, *International Journal of Electronics* 69 (1990) 33-42.

25. A.K. Ray and C.A. Hogarth, International Journal of Electronics, 69 (1990) 97-107.

26. J.R. Yeargan, & H.L. Taylor, *Journal of Applied Physics*, 39 (1968) 5600-5604.

27. J.G. Simmons, Physical Review, 155 (1967) 657-660.

28. Fateh Mohammad Nazar, *Japanese Journal of Applied Physkics*, 17 1978) 1953-1957.

29. S.P.S. Arya and H.P. Singh. Thin Solid Films, 62 (1979) 353-356.

30. R.H. Hill, Phidosophical Magazine, 20 (1970) 59-86.

31. K.S. Chari and B. Mathur, Thin Solid Films, 75 (1970) 157-167.

32. R. Signerski and J. Kalinowski, Thin Solid Films, 75 (1970) 157-167.

33. T. Mahalingam, M. Radhakrishnan and C. Balasubramanian, *Thin Solid Films*, 78 (1981) 245-249.

34. M. Stuart, RRIT *Journal of Applied Physics*, 18 (1967) 1637-1640.

35. R.M. Hill, T.J. Coutts, Thin Solid Filsm, 35 (1976) 117-120.

36. W. Herdt, H.Adachi and H.L. Hartnagel, Thin Solid Films, 82 (1981) 293-297.

37. E. Schabowska, Thin Solid Films, 75 (1981) 177-180.

38. T. Wiktorczyk, C. Wesolowska, Thin Solid Films, 91 (1982) 9-21.

39. Sh. M. Efendiev. A.A. Agasiev, V.E. Bagiev and Ya Yu Guseinov, *Physico Status Solidi* (a), 116 (1989) 305-311.

40. Z.T. Al-Dhhan and C.A. Hogarth, *International Journal of Electronics*, 64 (1988) 443-449.

41. M. Anwar and C.A. Hogarth, Internaitonal Journal of Electronics 67 (1989) 551-565.

42. Z.T. Al Dhhan, C.A. Hogarth and A. Davidson, *International Journal of Electronics*, 66 (1989) 409-418.

43. M. Anwar and C.A. Hogarth, Internaitonal Journal of Electronics, 66 91989) 419-436.

44. R.A. Moreno, C.X. Cardoso and M. Yoshida, *Physica Status Solidi* (a), 119 (1990) 583-588.

45. R.D. Gould and B.B. Ismail, *International Journal of Electronics*, 69 (1990) 19-24.

46. T.S. Shatai and R.,D. Gould, *International Journal of Electronics*,. 69 (1990) 3-9.

47. M. Pollak, Physical Review, 138 (1965) A1822-A1826.

48. M.L. Knotek, M.. Pollak and T.M. Donovan, Physical Review Letters, 30 (1973) 853-856.

49. R.M. Hill, Physica Status Solidi (a), 35 (1976) K-33

50. G.A. Niklasson, Pysics Department, Chalmers University of Technology, S-41296 Gothenburg, Sweden, (1987) RI-R14.

51. M.D. Hossain, Applied Physics, A29 (1982) 29-32.

52. M.J. Jayraj and C.P.G. Vallabhan, Physica Status Solidi(a) 115 91989) K63-K65.

53. V.S. Dharmadhikari and A. Goswami, Thin solid Films, 87 (1982) 119-126.

54. N.C. Halder and L.C. Nagarajan, *Physica Status Solidi(a)* 113 (1989) 511-519.

55. N.C., Halder, *Physica Stauts Solidi* (a), 112 (1981) 589-599.

56. S. Mishra, A.V. Krishna Rao and K.V. Rao, *Physica Status Solida* (a), 114 (1989) K115-K118.

57. S.K. Arora and T. Mathew, *Physica Status Solida (a)*, 116 (1989) 405-413.

58. V. Parkhutik, V. Sokol, V. Shershulskii, E. Utkina and A. Vorobeva, *Physica Stustus Solidiy* (a), 114 (1989) K33-K37.

59. A.L. Shavalov and M.S. Feldma, Thin Solid Films 151 (1987) L105-L108.

60. R. Sathyamoorthy, SA.K. Narayan Dass, C. Balasubramanian and D.d. Mangalaraj, *Physica Status Solidi* (a), 117 (1990) 495-500.

61. M.D. Kannan, SA.K. Narayan Dass, C. Balasubramanian and D. Mangalaraj, *Physica Status Solida* (a) 121 (1990) 515-523.

62. V. Lhotska, J. Fousek and N. Neumann, *Physica Status Solidi* (a), 120 (1990) 27-283.

63. R. Salam, *Physica Status Solidi* (a), 117 (1990) 55-540.

64. Sawaby, H.H. Afity and A.A. Shabaka, *Indian Journal of Physics* 64A (1990) 4422-431.

65. R. Heidinger, *International Journal of Physics*, 64 (1988) 37-48.

66. G.S. Nadkarni and V.S. Shirodkar, Thin Solid Films, 94 (1982) 101-109.

67. G. Hass and C.D. Salzberg, *Journal of the optical Society of America*, 44 (1954) 181-187.

68. Debajyoti Das and Ratnabati Banerjee, *Thin Solid Films* 147 (1987) 321-331.

69. A.L. Shabalov, M.S. Feldman, Thin Solid Films, 151 (1987) 317-323.

70. D.E. Aspnis, thin Solid Tilms, 89 91982) 249-262.

71. D.F. Bezuidnhout, R. Pretoriu, Thin Solid Films, 139 (1985) 121-132.

72. V.S. Dharmadhikari and A. Goswami, Thin Solid Films, 87 (1982) 119-126.

73. P. Grosse and H. Kostlin, thin Solid Films, **90** (1982) 309-315.

74. L. Michailovits, I. Hevesi *et al.*, thin Solid Films, **102** (1983) 71-76.

75. M. Fantini, I. Torriani, Thin Solid Films, **138** (1985) 255-265.

76. A.A. Zahab, M. Abe-Lefdil and M. Cadene, *Physica Status Solida* (a), **117** (1990) K103-K106.

77. C. Albers and A. Jacobi, Physica Status Solida (a), **113** (1989) K135-K137.

78. A. Shamim, K.M. Khan, A. Ahmad, M.Suleman, A. Mateen and A. Waseem, *International Journal of Electronics*, **67** (1989) 235-242.

79. Hong Wang, Jinke Wen, Bin Li and Huafu Wang, *Physica Status Solidi* (a), **118** (1990) K47-K50.

80. J.L. Lindstrom, B.G. Svensson, W.X, Ni and M. Wallander, *Physica Status Solidi* (a), **117** (1990) K171-k174.

81. R. Ashokan, V. Gopal and K.C. Chhabra, *Physica Status Solidi* (a), **121** 533-537.

82. E. Pigorsch and W.E. Steger, *Physica Status Solidi* (a), **117** (1990) K189-K191.

83. H. Araki and T. Hanawa, Thin Solid Films **158** (1988) 207-216.

84. D.G. Walmsley. E.I. Wolf. J.W. Osman. Thin Solid Films, **62** (1979) 61-66.

85. T. Figielski, *Physica Status Solidi* (a). **121** (1990) 187-193.

86. Salwar *et al. International Journal of Electronics*, **69** (1990) 87-95.

87. M.A.R. Sarkar. Ph.D. Thesis, 1984.

88. J. Frenkel, *Phys. Rev.* **54** (1938) 647.

89. Paramdeep Khurana and K.K. Srivastava, *Physica Status Solidi* (a), 115 (1989) K57-K61.

90. C.R. Dutta and K. Barua, Thin Solid Films, 92(1982) 281-285.

91. G.S. Nadkarni and N.S. Shirodkar, Thin solid Films. 105 (1985) 115-129.

92. Max Born and Emil Wolf, principle of Optics, 1959.

93. L.I. Maissel and R. Glang, Hand Book of Thin Film Technology, 1970.

94. I.Ohlidal and K. Nauratil, Thin solid Films, 15691988) 181-189.

95. A. Subbarayan, C. Balasubramanian, S.K. Narayandass, *Indian Jouranl of pure Applied Physics* (India), Vol.26, no. 6 (1988) 410-416.

96. Z.T. Al-Dhhan. C.a. Hogarth. *Internaitonal Journal of Electronics* (UK). 63 (1987) 707-722.

97. Z.T. Al-Dhhan, C.A. Hogarth, *International Journal of Electronics* (UK), 64 (1988) 443-449.

98. L. Zdanowicz, B. Jarzabck, *Journal of Non-Crystalline solids* (netherlands), 97-98 (1987) 1203-1206.

99. A.K. Ray, C.A. Hogarth, Thin solid Films (Switzerland), 144 (1986) 111-114.

100. B.P. Rai, *Physica Status Solidi* (a) (Germany) 110 91987) PK189-PK193.

101. Wha-Tek Kim, Chang-Dackim, *Journal of Applied Physics* (USA), 60 (1986) 2631-2633.

102. A.K.Roy, C.A. Hogarth, *Journal of Physics*, D(GB) 20 (1987) 552-554.

103. M. Hirano, N. Miyamoto, *Electronics and Communication*, Japan, 70 (1987) 95-106.

104. T. Gengenbach, H. Pagnia, N. Sotnik, Materials Letters (Netherlands) 5 (1987) 215-217.

105. J. Despujols, *Thin solid Films*, (Switzerland), **143** (1986) 7-18.

106. H. Ettaik, S. Lefrant, G. Leising, F. Stelzer, Synth. Met. (Switzerland), **38** (1990) 69-76.

107. N.J. Geddes, J.R. Sambles. W.G. parker. N.R. Couch, D.J. Jarvis, *Journal of Physics D. Applied Physics* (UK), **23** (1990) 95-102.

108. M.H. Islam, C.A. Hogarth, *Journal of Materials Science* (UK), **24** (1989) 187-194.

110. L. Eckertova, Materials Science (Poland), **13** 91987) 93-98.

111. H. Lehmberg, Materials Science (Poland) **13** (1987) 117.

112. N. Sotnik, Materials Science (Poland), **13** (1987) 125-129.

113. J.E. Olsen, F. Shimura, *Appl Phys. Lett.* (USA), **53** (1988) 1934-1936.

114. G.A. Dubinina, A.O. Ksenofontav, M.N. Libenson, Opt. Spectrosc. (USA), **63** (1987) 645-648.

115. M. Anwar, C.A. Hogarth, *Physica status solidi* (a), (E. Germany), **109** (1988) 469-478.

116. W.I. Khleif, C.A. Hogarth, *Physica Status solidi* B. (E. Germany), **149**(1988) PK187-PK190.

117. J. Beynon, M.M.A.G. El. Samanovdy, S.K.J. Al-Ani, *Journal of Materials Science Lett* (UK) 8(1989) 786-8.

118. S.P. Edirising. C.A. Hogarth, *Journal of materials Science Ltd.*, (UK) **8** (1989) 789-792.

119. W.I. Khleif. Z.t. Al-Dhhan. C.A. Hogarth. *International Journal of Electronics* (UK). **65** (1988) 789-796.

120. H. pagnia, N. Sotnik, *Physica status solidi* A (East Germany), **108** (1988) 11-65.

121. M. Lepek, Gryst. Res. Technolo. (East Germany), 23 (1988) PK66-PK69.

122. K.C. Sharma, J.C.Garg, *Indian Journal of Pure applied physics* (India), **26** (1988) 480.

123. H. Demiryont, K.E. Nietering, R. Surowice, F.I. Brown, D.R. Piatt, *Appl. opt.* (USA) **26** (1987) 3803-10.

124. H.I. Park, C.H. Chung, C.H.Kim, H.S. Kim, *Journal of Materials Science* (UK), **6** (1987) 1093-4.

125. R. Uitz. G. Temmel, G. Leising, H.Kahlest, Z. Phys. B Condensed Matter (West Germany), **67** (1987) 459-465.

126. K. Sakai, H. Matsuda, H. Kawada, K. Eguchi, T. Nakagiri, *Applied Physics Letter* (USA), **53** (1988) 1274-6.

127. M. Bischoff, *Materials Science* Poland) **13** (1987) 49-54.

128. R.J. Soukup, T.E. Tiwald, *J. Vac. Sci. Technol* A. Vac. Surf. Films (USA) **6**(1988) 1759-62.

129. T. Wiktorczyk, *Thin Solid Films*, **157** (1988) 13-20.

130. S. Saito, T. Yamamuto, T. Masuda, S. Thara, A. Yoshda, *Res. Rep. Koga Kuin Univ* (Japan). **67** (1989) 81-87.

131. C.A. Hogart, M.Zar, *Physica Status Solidi* (a) (Germany), **98** (1986) 611-616.

132. S.A. Bhosale, *Physica Status Solidi* (a) (Germany), **101** (1987) 639-50.

133. Sh.M. Alckperova, V.A. Vetkhov, G.S. Gadzhieva, F.D. Kasimov, V.M. Mamikonova, *Telecommunicaiton and Radio Eng.* **41** (1986) 89-91.

134. M.Y. Nadeem, C.A. Hogarth, *Journal of Materials Science Left.* (UK), 9 (1990) 857-9.

135. F.W. Schmidlin, *Phys. Rev.* **B16** (1977) 2362 Philoso. Mg. B41 (1980) 535.

136. V.S. Dharmadhikari, Thin Solid Films, **103** (1983) 311-317.

137. R. Fuchshuber, R. Gullishien and S. Roizen C.R. Acad. Sci. (Paris), 251 (1960) 51

138. C.R. Barnes and C.R. Geesover, *J. Electrochem. Soc.* **107** (1960) 98.

Rajshahi University Library
Documentation Section
Document No. D-1901
Date 10.10.98